

CFD simulacija nenominalnih radnih točaka centrifugalnog kompresora

Čorak, Matej

Master's thesis / Diplomski rad

2021

Degree Grantor / Ustanova koja je dodijelila akademski / stručni stupanj: **University of Zagreb, Faculty of Mechanical Engineering and Naval Architecture / Sveučilište u Zagrebu, Fakultet strojarstva i brodogradnje**

Permanent link / Trajna poveznica: <https://urn.nsk.hr/urn:nbn:hr:235:516890>

Rights / Prava: [Attribution-NoDerivatives 4.0 International/Imenovanje-Bez prerada 4.0 međunarodna](#)

Download date / Datum preuzimanja: **2024-07-06**

Repository / Repozitorij:

[Repository of Faculty of Mechanical Engineering and Naval Architecture University of Zagreb](#)



UNIVERSITY OF ZAGREB
FACULTY OF MECHANICAL ENGINEERING AND NAVAL
ARCHITECTURE

MASTER'S THESIS

Matej Čorak

ZAGREB, 2021

UNIVERSITY OF ZAGREB
FACULTY OF MECHANICAL ENGINEERING AND NAVAL
ARCHITECTURE

MASTER'S THESIS

CFD SIMULATION OF OFF-DESIGN OPERATING POINTS OF A
CENTRIFUGAL COMPRESSOR

Mentor:
prof. dr. sc. Hrvoje Jasak

Student:
Matej Čorak

ZAGREB, 2021

I would like to express my sincere appreciation to my mentor, professor Jasak for this opportunity and for helping me through this project.

Furthermore, I would like to thank dr. Tessa Uroić and Luka Balatinec for their constructive criticism, patience and guidance through the project.

Finally, I would like to thank my family and my girlfriend for all the support and understanding they have provided me.

Statement | Izjava

I hereby declare that I have made this thesis independently using the knowledge acquired during my studies and the cited references.

Izjavljujem da sam ovaj rad radio samostalno koristeći znanja stečena tijekom studija i navedenu literaturu.

Zagreb, March 2021

Matej Čorak



SVEUČILIŠTE U ZAGREBU
FAKULTET STROJARSTVA I BRODOGRADNJE



Središnje povjerenstvo za završne i diplomske ispite
Povjerenstvo za diplomske ispite studija strojarstva za smjerove:
procesno-energetski, konstrukcijski, brodstrojarski i inženjersko modeliranje i računalne simulacije

Sveučilište u Zagrebu	
Fakultet strojarstva i brodogradnje	
Datum:	Prilog:
Klasa: 602 - 04 / 21 - 6 / 1	
Ur. broj: 15 - 1703 - 21 -	

DIPLOMSKI ZADATAK

Student: **Matej Čorak**

Mat. br.: 0035198989

Naslov rada na hrvatskom jeziku: **CFD simulacija nenominalnih radnih točaka centrifugalnog kompresora**

Naslov rada na engleskom jeziku: **CFD simulation of off-design operating points of a centrifugal compressor**

Opis zadatka:

CFD simulations are frequently used as a tool in the design process of various turbomachinery components. However, CFD can also be used in the later stages to investigate the off-design operating points and fluid flow instabilities which may occur due to changing load, flow rate or rotational speed. The objective of this thesis is to investigate whether a CFD simulation of a single blade passage of a centrifugal compressor can be used to predict the flow field corresponding to conditions with off-design operating parameters.

The candidate shall perform the following tasks within this project:

- Perform a literature survey of off-design operating conditions of centrifugal compressors and describe the theoretical framework and principles;
- Perform a literature survey of CFD simulations of centrifugal compressors and describe the applied models and methods;
- Construct a 3D Finite Volume mesh of a single blade passage of a centrifugal compressor;
- Perform numerical simulations for three operating points of the centrifugal compressor, including off-design operating points, using the cyclic boundary conditions on the reduced geometry;
- Analyse the results of the simulations and compare the flow field for the three operating points;
- Additionally, describe the effects which the blade passage position relative to the stator might have on the flow field and whether this can be captured by the reduced geometry simulation.

The candidate must list the bibliography and any assistance received during this study.

Zadatak zadan:

21. siječnja 2021.

Datum predaje rada:

25. ožujka 2021.

Predviđeni datum obrane:

29. ožujka – 2. travnja 2021.

Predsjednica Povjerenstva:

Zadatak zadao:

Prof. dr. sc. Hrvoje Jasak

Prof. dr. sc. Tanja Jurčević Lulić

Contents

1	Introduction	1
1.1	Turbomachinery	1
1.2	Previous and Related Studies	7
1.3	Scope of the Thesis	7
1.4	Thesis Outline	8
2	Finite Volume Method	9
2.1	Introduction	10
2.2	Scalar Transport Equation	10
2.3	Governing Equations	12
2.3.1	Conservation of Mass	12
2.3.2	Conservation of Energy	12
2.3.3	Conservation of Momentum	13
2.4	Finite Volume Equations Discretisation	13
2.4.1	Linear System of Equations	16
2.4.2	Discretisation of the Temporal Derivative	17
2.4.3	Discretisation of the Convection Term	18
2.4.4	Discretisation of the Diffusion Operator	18
2.4.5	Discretisation of Source and Sink Terms	19
2.5	Compressible Navier-Stokes Equations	19
2.6	Boundary Conditions	21
2.7	Turbulence Modelling	22
2.7.1	Reynolds-Averaged Navier-Stokes Equations (RANS)	23
2.8	Closure	26

3	Applications of CFD Methods in Turbomachinery	27
3.1	Introduction	27
3.2	Domain Handling	27
3.2.1	Multiple Reference Frame	28
3.2.2	Moving Mesh	34
3.3	Interface Handling	35
3.3.1	General Grid Interface	35
3.3.2	Mixing Plane	38
3.4	Closure	39
4	Geometry and Computational Domain	40
4.1	Introduction	40
4.2	Centrifugal Compressor	40
4.2.1	Work and Energy Equations in a Rotating Frame	41
4.2.2	Moment of Momentum in the Absolute Frame	42
4.2.3	Flow Instabilities	44
4.3	Computational Domain	45
4.3.1	Boundary Definition	48
4.3.2	Boundary Conditions	55
4.4	Simulation Setup	59
4.5	Closure	59
5	Results	60
5.1	Introduction	60
5.2	Design operating conditions	60
5.3	Off-design operating condition	78
5.3.1	Choke condition	78
5.4	Closure	80
6	Conclusion	81
6.1	Conclusion	81
6.2	Future Work	82

A	Appendix	83
A.1	MRFZone	83
A.2	GGI	84
A.3	cyclicGgi	85
A.4	OpenFoam Boundary Conditions Description	86
A.4.1	von Neumann Boundary Condition	86
A.4.2	Dirichlet Boundary Condition	86
A.4.3	Mixed Boundary Conditions	87
A.4.4	GGI Boundary Conditions	87
A.4.5	Wall Boundary Conditions	88
	Bibliography	90

List of Figures

1.1.1	Compressors classification.	2
1.1.2	Simple centrifugal compressor [1].	3
1.1.3	Compressor control volume [1].	5
2.2.1	Closed system or Control Volume (CV) [2].	11
2.2.2	Surface and Volume sources of the CV [2].	11
2.4.1	Convex polyhedral control volume [3].	14
2.7.1	Vortex dynamics and energy cascade [3].	22
3.2.1	Single Frame of Reference [2].	28
3.2.2	Multiple Frame of Reference [2].	29
3.2.3	Single blade model with rotationally periodic boundaries [4].	30
3.3.1	OverlapGgi interface of axial turbo compressor [4].	37
3.3.2	CyclicGgi interface [2].	38
4.2.1	Relative and absolute velocities [5].	41
4.2.2	Meridional streamtube section for open rotor [5].	42
4.2.3	Mechanism of stall cell propagation [6].	44
4.2.4	Centrifugal compressor map with highlight choke and surge line [7].	45
4.3.1	<i>YZ</i> plane.	47
4.3.2	<i>XY</i> plane.	47
4.3.3	Regions of the domain.	48
4.3.4	Inlet region patches.	49
4.3.5	Inlet misalignment.	50
4.3.6	Rotor region.	51
4.3.7	Rotor region patches.	52

4.3.8	Diffuser region patches.	54
5.2.1	Simulated conditions.	61
5.2.2	Velocity vectors at the inlet.	62
5.2.3	Velocity vectors in diffuser.	63
5.2.4	Pressure field.	64
5.2.5	Temperature field.	64
5.2.6	Turbulent kinetic energy field.	65
5.2.7	Rothalpy field.	65
5.2.8	Velocity field view with a slice of the diffuser part.	66
5.2.9	Relative velocity field view with a slice of the diffuser part.	67
5.2.10	Pressure field view with a slice of the diffuser part.	67
5.2.11	Temperature field view with a slice of the diffuser part.	68
5.2.12	Rothalpy field view with a slice of the diffuser part.	68
5.2.13	Turbulent kinetic energy field view with a slice of the diffuser part.	69
5.2.14	Mach number field view with a slice of the diffuser part.	69
5.2.15	Rotor slice velocities.	71
5.2.16	Rotor velocities vectors.	71
5.2.17	Lambda shock.	72
5.2.18	Velocity field view at meridional plane.	73
5.2.19	Pressure field view at meridional plane.	73
5.2.20	Temperature field view at meridional plane.	74
5.2.21	Density distribution at meridional plane.	74
5.2.22	Rothalpy field at meridional plane.	75
5.2.23	Turbulent kinetic energy field at meridional plane.	75
5.2.24	Pressure field at whole geometry.	76
5.2.25	Velocity field at whole geometry.	77
5.2.26	Temperature field at whole geometry.	77
5.3.1	Shock wave location.	78
5.3.2	Pressure field for choke condition.	79
5.3.3	Density field for choke condition.	79

List of Tables

2.0.1	Flow Classification based on Mach number [3].	9
4.3.1	Compressor design parameters.	46
4.3.2	Inlet mesh region.	49
4.3.3	Inlet region patches.	50
4.3.4	Rotor mesh region.	51
4.3.5	Rotor region patches.	53
4.3.6	Diffuser mesh region.	53
4.3.7	Diffuser region patches	54
4.3.8	GGI pairs and corresponding zones.	55
4.3.9	Boundary conditions for inlet region.	56
4.3.10	Boundary conditions for rotor region.	57
4.3.11	Boundary conditions for diffuser region.	58
5.2.1	Operating points specifications.	61
5.2.2	Mass flow rate results.	61
5.2.3	Rotor forces, moments and power.	62

Nomenclature

Latin Characters

Symbol	Description	Unit of Measure
a	Acceleration	[m/s ²]
	General vector property	[–]
a_N	Matrix coefficient of neighbour [N]	
a_P	Central coefficient	[–]
C_f	Centrifugal force	[N]
C_l	Coefficient of lift	[–]
C_o	Coriolis force	[N]
\mathbf{d}_f	Delta vector	[m]
e	Total specific energy	[J/m ³]
F	Face flux	[–]
f	Value at cell face	[–]
\mathbf{g}	Gravitational acceleration	[m/s ²]
i	Enthalpy	[m ² /s ²]
k	Turbulent kinetic energy	[m ² /s ²]
M	Momentum	[Nm]
MaU	Mach number	[–]
\mathbf{n}	Surface normal vector	[–]
n	Polytropic exponent	[–]
P	Value at cell centroid or power	[W]
Q	Volume heat source	[N/m ³]
\mathbf{q}	Specific heat flux	[W/m ²]
q_p	Constant part of source term	[–]
q_u	Linear part of source term	[–]
R	Gas constant	[J/kgK]
\mathbf{r}_P	Centroid position vector	[m]
$ S $	Surface area of faceset	[m ²]
S_m	Surface area of V_m	[m ²]

S_f	Face surface area	$[\text{m}^2]$
\mathbf{s}_f	Surface normal vector	$[\text{m}]$
T	Temperature	$[\text{K}]$
t	Time	$[\text{s}]$
\mathbf{U}	Velocity	$[\text{m}/\text{s}]$
\mathbf{u}	Blade speed	m/s
V	Material volume	$[-]$
V_m	Material volume	$[\text{m}^3]$
V_p	Volume of cell	$[\text{m}^3]$
W	Weighting factor or work	$[\text{J}]$
\mathbf{w}	Relative velocity	$[\text{m}/\text{s}]$
\mathbf{x}	Position vector	$[\text{m}]$
\mathbf{Z}	General vector	$[-]$

Greek Characters

γ	Heat capacity ratio	[–]
η	Efficiency	[–]
λ	Thermal conductivity	[W/mK]
μ	Dynamic viscosity	[Pas]
ν_{teff}	Effective kinematic viscosity	[m/s]
ϕ	General property	[–]
Φ	Patch variable	[–]
ρ	Fluid density	[kg/m ³]
σ	Cauchy stress tensor	[N/m ²]
τ	Friction force	[N]
ψ	Compressibility	[J/mol]
ω	Angular velocity	[rad/s]

Superscripts

t	Instance of time
n	Value at new time step
o	Value at old time step
\rightarrow	Vector quantity

Subscripts

a	Axial
b	Blade
c	Casing
d	Disc
I	Inertial frame of reference
M	Master
R	Relative frame of reference
r	Radial

<i>rel</i>	Relative
<i>rot</i>	Rotational
<i>S</i>	Shadow
1	Upstream state
2	Downstream state

Abbreviations

BC - Boundary Conditions

CFD - Computation Fluid Dynamics

CV - Control Volume

DNS - Direct Numerical Simulations

FVM - Finite Volume Method

GGI - General Grid Interface

LES - Large Eddy Simulation

MRF - Multiple Frames of Reference

RANS - Reynolds-Averaged Navier-Stokes Equations

Re - Reynolds number

RTT - Reynolds Transport Theorem

SRF - Single Reference Frame

Abstract

CFD simulations of turbomachinery are now a part of the standard approach in the design process. However, CFD as an investigation tool in the later stages of the design process, namely to investigate off–design operating points and fluid flow instabilities are rarely used in practice. The main objective of this work is to investigate the applicability of CFD software, eg. open–source library foam–extend to predict the flow field corresponding to off–design operating conditions of a centrifugal compressor. Since a full rotor geometry is challenging to model due to the size of the computational mesh, we decided to investigate performing the simulations on a single blade passage using cyclic boundary conditions for non–conforming meshes (Generalised Grid Interface – GGI). The mesh is block–structured, created in Pointwise with 7.2 million cells. A Multiple Reference Frame approach is used to model the rotation, which means that the obtained flow field corresponds to a single rotor position. Start–up of the simulation is very sensitive due to the extreme operating conditions of the nominal operating–point, and it is necessary to introduce the boundary conditions gradually. Thus, the total pressure ratios and MRF angular velocity are increased progressively to prevent the simulation from crashing due to local extreme velocities and pressure values. To validate the simulation approach, a comparison is made to experimental and numerical data provided by Dewar and Tiainen [8]. The final objective is to create a compressor map with the established flow field features corresponding to different operating points, and some close surge and choke conditions.

Key words: *CFD, OpenFOAM, foam-extend, turbomachinery, centrifugal compressor.*

Sažetak

Korištenje CFD simulacija ustaljena je praksa u procesu konstruiranja turbostrojeva. Međutim, korištenje CFD-a u kasnijim fazama konstruiranja s ciljem istraživanja nenominalnih radnih točaka i nestabilnosti strujanja je vrlo rijetko i ima jedino akademski značaj. Cilj rada je istražiti mogućnosti CFD softwera *foam-extend* za izračunavanje polja strujanja u nenominalnim radnim točkama. Kako bi se skratilo vrijeme trajanja simulacija, odabrano je modelirati samo jedan kanal koji se nalazi između dvije rotorske lopatice. Kako bi se reprezentativno modelirao samo jedan prolaz potrebno je pripremiti mrežu sa specifičnim alatima koji se često koriste kod CFD simulacija turbostrojeva. U radu je opisana procedura pokretanja simulacije jer je početne uvjete trebalo mijenjati, kako bi se ostvarila konvergencija nelinearnog sustava jednadžbi turbulentnog strujanja s izmjenom topline. Postepeno je mijenjana razlika tlaka između ulaza i izlaza na kompresoru, sve do postizanja ciljanog masenog protoka. Rezultati su dopuna rezultata iz literature, a cilj rada je prikazati mapu rada kompresora, uključujući i stanje zagušenja toka.

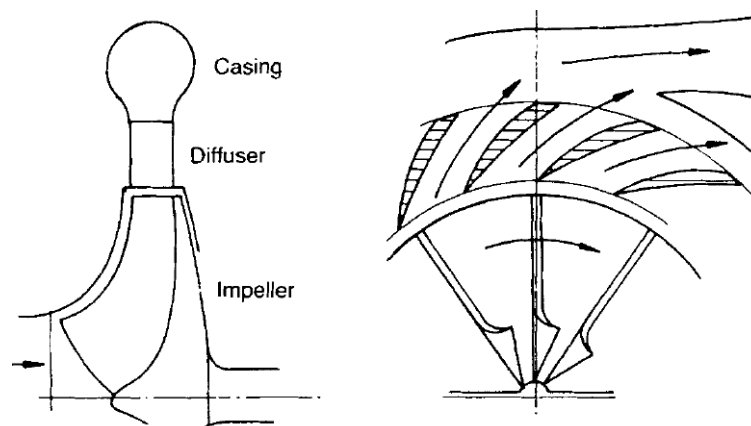
Ključne riječi: *CFD* , *OpenFOAM* , *foam-extend* , *turbostrojevi* , *centrifugalni kompresor*.

Prošireni sažetak

Uvod

Turbostrojevi vrše pretvorbu energije između radnog fluida i sklopa rotirajućih lopatica. Radni fluid može biti voda, para, zrak, kapljevina ili plin. U osnovi postoje dvije vrste turbostrojeva: pumpe i kompresori koji troše mehaničku energiju za rad koji prenose mediju, dok turbine koriste energiju fluida te obavljaju pretvorbu u druge oblike energije, npr. mehaničku. Turbostrojeve je također moguće podijeliti prema smjeru strujanja: radijalno, aksijalno i mješovito. Kod radijalnih strojeva, tok je okomit na os rotacije. Aksijalni strojevi imaju tok paralelan s osi rotacije, dok mješoviti strojevi imaju karakteristike radijalnih i aksijalnih strojeva.

Postoje dvije kategorije kompresora gledano sa stajališta principa po kojem se odvija kompresija, klipni i dinamički. Klipni kompresori usisavaju zrak kroz usisni ventil, stlaču ga mehaničkim smanjenjem volumena i izbacuju van kroz ispušni ventil. Dinamički kompresori rade na principu ubrzavanja toka fluida. Razlika između radijalnih i aksijalnih kompresora uočava se u principu rada, kao i ostvarenom masenom protoku i kompresijskom omjeru. Za jednake vanjske promjere, aksijalni kompresori propuštaju veći maseni protok ali imaju manji kompresijski omjer. Tipičan centrifugalni kompresor prikazan je na slici 1. Strujanje ulazi aksijalno u smjeru strelice, dolazi do rotora koji ga ubrzava, zakreće tok i izbacuje ga radijalno. Nakon izlaza iz rotora strujanje ulazi u stator gdje se nalaze statorske lopatice koje imaju funkciju usmjeravanja i usporavanja toka. Usporavanjem toka preuzima se energija koju sadrži obodna komponenta brzine.



Slika 1: Centrifugalni kompresor [1].

Matematički model

Osnovne jednačbe numeričkog modela temelje se na zakonima očuvanja:

- Zakon očuvanja mase:

$$\frac{\partial \rho}{\partial t} + \nabla \cdot (\rho \mathbf{U}) = 0. \quad (0.0.1)$$

- Zakon očuvanja energije:

$$\frac{\partial(\rho e)}{\partial t} + \nabla \cdot (\rho e \mathbf{U}) = \underbrace{\rho \mathbf{g} \cdot \mathbf{U}}_{\text{snaga gravitacijskih sila}} + \underbrace{\nabla \cdot (\boldsymbol{\sigma} \cdot \mathbf{U})}_{\text{snaga površinskih sila}} - \underbrace{\nabla \cdot \mathbf{q} + \rho Q}_{\text{toplinski tok}}. \quad (0.0.2)$$

- Zakon očuvanja momenta količine gibanja:

$$\frac{\partial \rho u}{\partial t} + \nabla \cdot (\rho u \mathbf{u}) = \underbrace{\rho g}_{\text{gravitacijska sila}} + \underbrace{\nabla \cdot \boldsymbol{\sigma}}_{\text{površinske sile}}. \quad (0.0.3)$$

Kako je strujanje u kompresoru stlačivo, potrebno je koristiti Navier-Stokesove jednačbe za stlačivo strujanje. Sljedeća jednačba je jednačba očuvanja momenta za stlačivo strujanje, izvedena iz jednačbe (0.0.1):

$$\frac{\partial(\rho \mathbf{u})}{\partial t} + \nabla \cdot (\rho \mathbf{u} \mathbf{u}) - \nabla \cdot [\mu(\nabla \mathbf{u} + (\nabla \mathbf{u})^T)] = -\nabla(P + \frac{2}{3}\mu \nabla \cdot \mathbf{u}). \quad (0.0.4)$$

Jednačba očuvanja energije izvedena je iz jednačbe (0.0.3) i glasi:

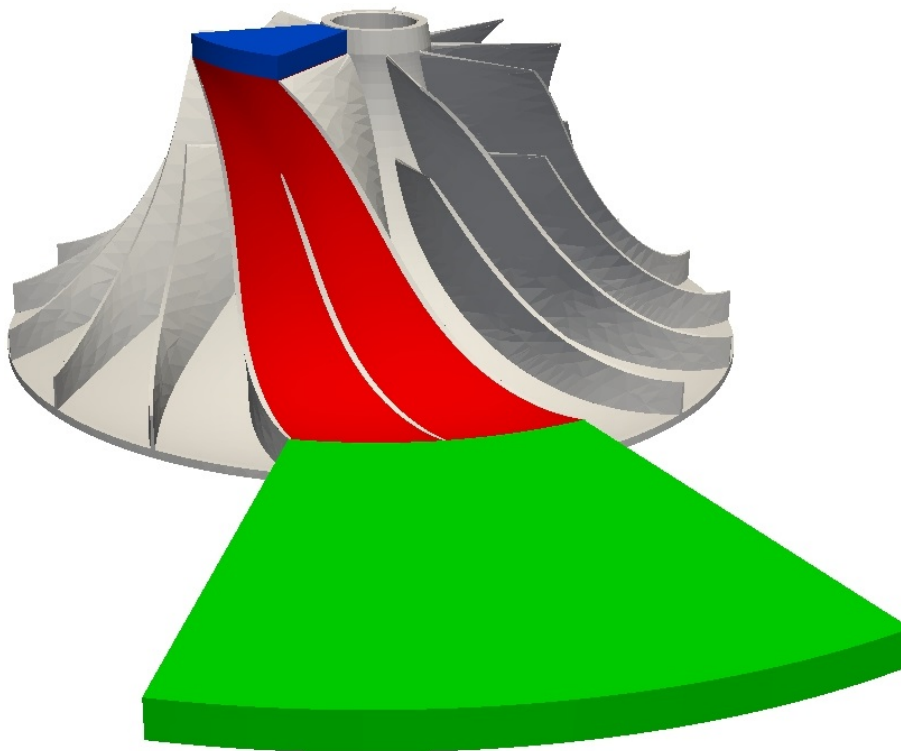
$$\frac{\partial(\rho e)}{\partial t} + \nabla \cdot (\rho e \mathbf{u}) - \nabla \cdot (\lambda \nabla T) = \rho \mathbf{g} \times \mathbf{u} - \nabla \cdot (P \mathbf{u}) - \nabla \cdot (\frac{2}{3}\mu(\nabla \cdot \mathbf{u}) \mathbf{u}) + \nabla \cdot [\mu(\nabla \mathbf{u} + (\nabla \mathbf{u})^T) \times \mathbf{u}]. \quad (0.0.5)$$

Gustoća ρ , tlak p i temperatura T povezani su preko jednačbe idealnog plina:

$$\rho = \frac{P}{RT}. \quad (0.0.6)$$

Numerička mreža i postavke simulacije

Numerička mreža izrađena je u programu Pointwise. Mreža se sastoji od 7196211 heksaedarskih ćelija podijeljenih u 3 bloka. Na slici 2. prikazan je smještaj numeričke mreže na model rotora. Mreža je izvedena iz 3 bloka kako bi se blokovima pridružili individualni inercijski koordinatni sustavi. Blok rotora označen je crvenom bojom na slici 2., blok statora zelenom i ulazni dio (dodan kako bi se profiliralo strujanje na ulazu) plavom bojom. Za os rotacije odabrana je os Z koja se poklapa s osi vratila.



Slika 2: Numerička mreža na modelu rotora.

Simulacije su provedene u softveru foam-extend. Za ulazne parametre korišteni su prije spomenuti podaci iz znanstvenog članka [8]. Zbog vrlo velikih brzina koje se javljaju u kompresoru, potrebno je simulaciji inicijalizirati polje brzina iz nestlačivog modela strujanja. Kao rubni uvjeti zadani su totalni tlak, totalna temperatura i maseni protok na ulazu. Zbog već spomenutih velikih brzina, tlak na izlazu postavljen je da se mijenja svakom iteracijom. U slučaju zadavanja konstantnih i konačnih vrijednosti rubnih uvjeta, rješenje bi brzo propagiralo kroz domenu i izazivalo numeričke nestabilnosti i raspad simulacije.

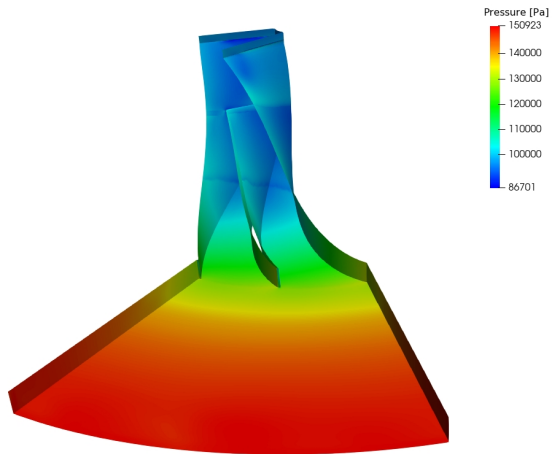
Rezultati simulacija

Simulacije su provedene za tri nominalne radne točke i jednu nenominalnu. Nominalne radne točke nalaze se najbliže krivulji najveće efikasnosti na mapi rada kompresora. U tablici 1 nalazi se usporedba rezultata simulacije i eksperimenta iz znanstvenog članka [8]. Također je potrebno uzeti u obzir nesigurnost mjerenja protoka u eksperimentu, koja prema podacima autora članka iznosi 1.3% do 2.5%, ovisno o tlaku na kojem je mjereno.

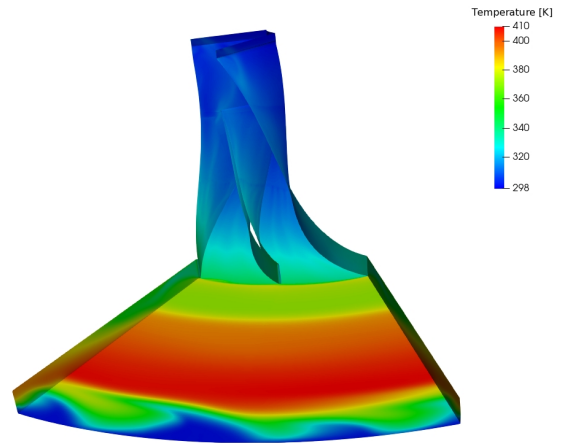
Tablica 1: Usporedba rezultata masenog protoka simulacije i eksperimenta.

Točka	Izmjereni maseni protok [kg/s]	Ostvareni maseni protok [kg/s]	Razlika
1	1.80	1.627	-10.09%
2	1.33	1.243	-6.79%
3	1.13	1.092	-3.40%

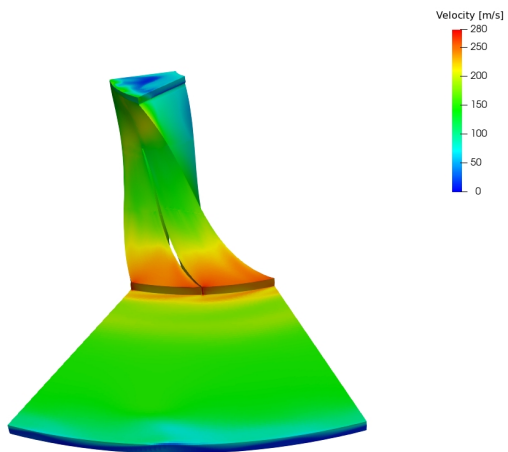
Sljedeće slike prikazuju različita polja varijabli strujanja. Slike odgovaraju točki pod brojem 3.



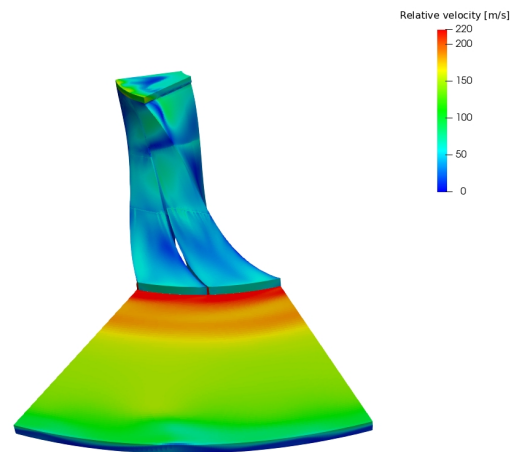
Slika 3: Raspodjela tlaka.



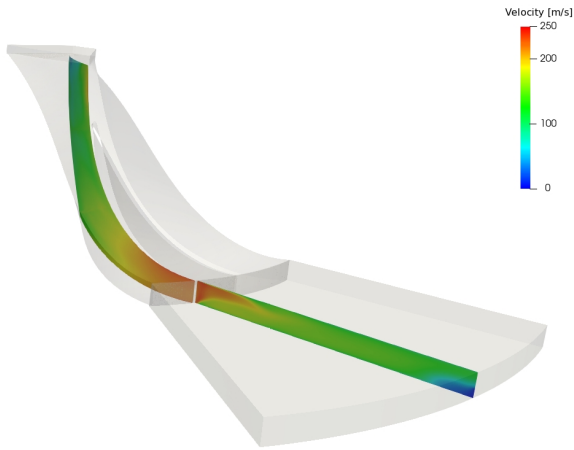
Slika 4: Raspodjela temperatura.



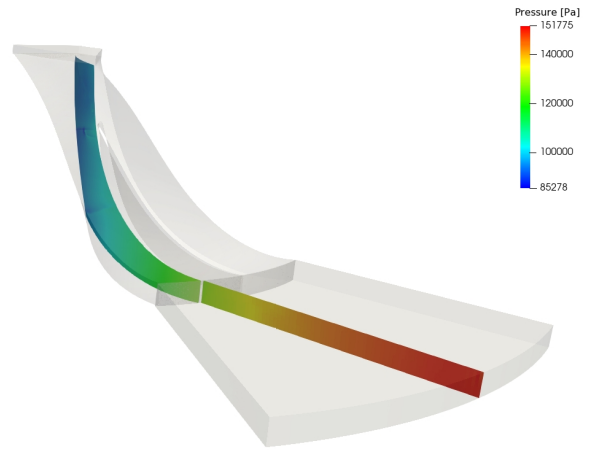
Slika 5: Raspodjela apsolutne brzine.



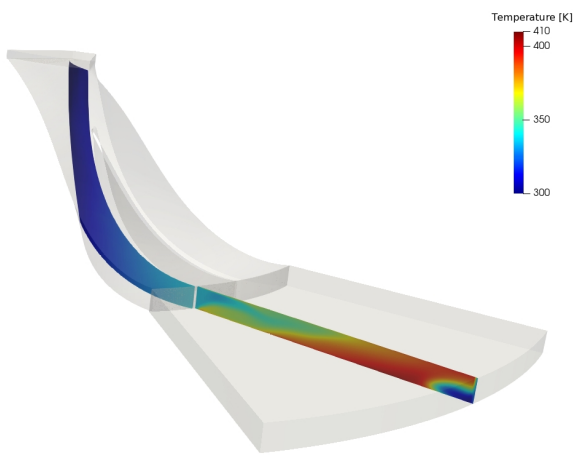
Slika 6: Raspodjela relativne brzine.



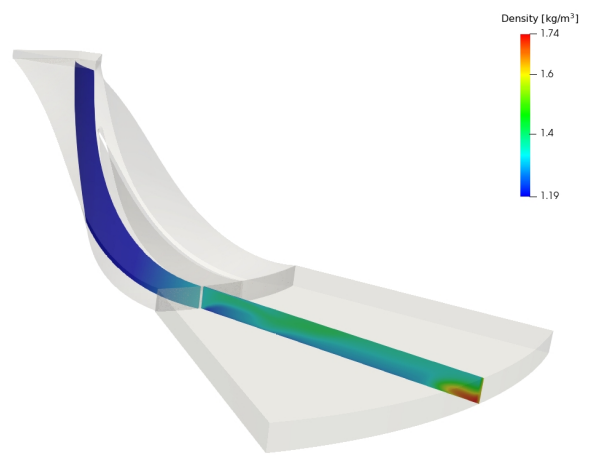
Slika 7: Raspodjela brzine na meridionalnom presjeku.



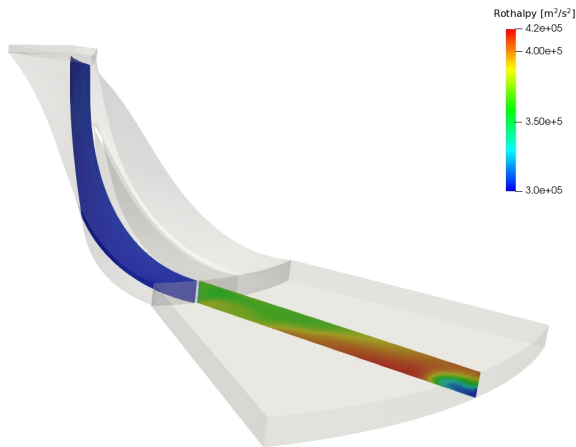
Slika 8: Raspodjela tlaka na meridionalnom presjeku.



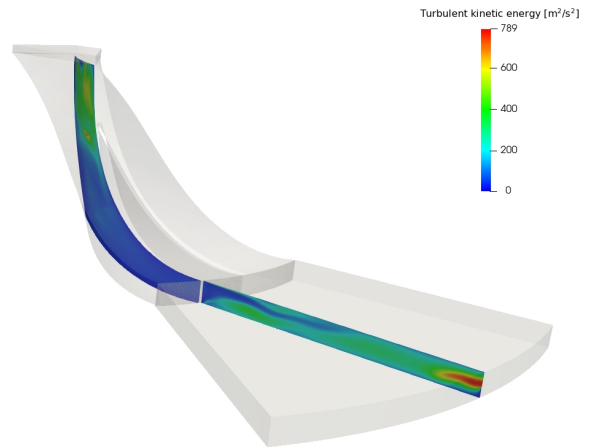
Slika 9: Raspodjela temperature na meridionalnom presjeku.



Slika 10: Raspodjela gustoće na meridionalnom presjeku

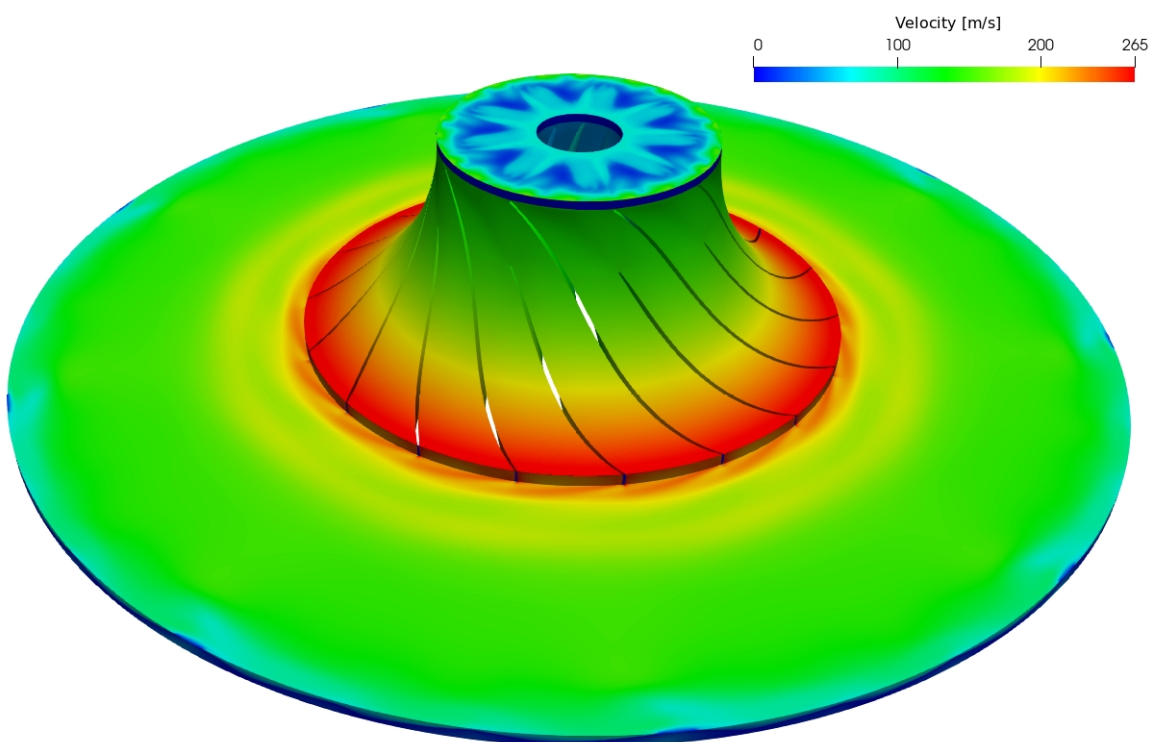


Slika 11: Raspodjela rotalpije na meridionalnom presjeku.

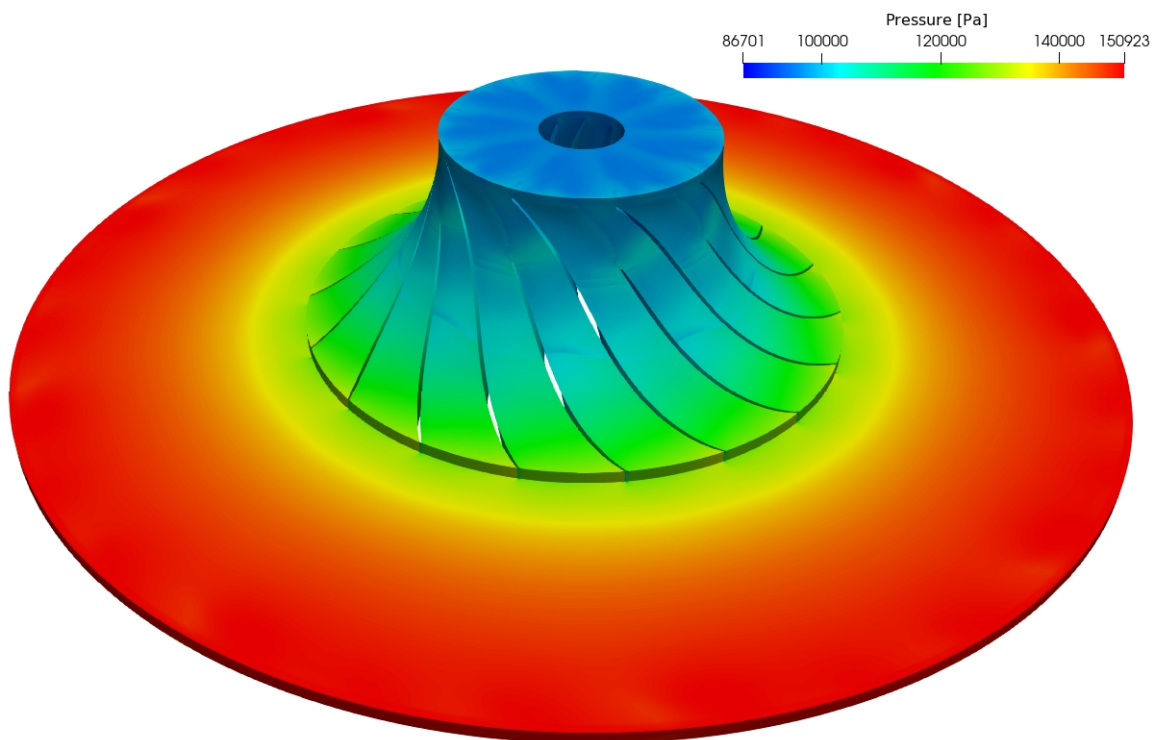


Slika 12: Raspodjela turbulente kinetičke energije na meridionalnom presjeku.

Iduće dvije slike predstavljaju rezultate simulacije na cijeloj geometriji, pokazuju raspodjelu brzina na slici 13. i raspodjelu tlaka na slici 14. Rezultati su dobiveni kopiranjem rezultata jednog prolaza devet puta.

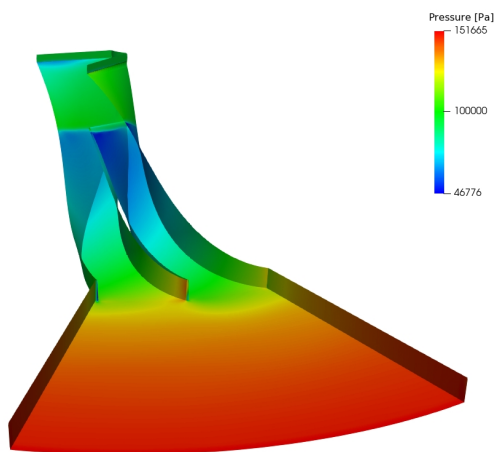


Slika 13: Raspodjela brzina na cijeloj geometriji.

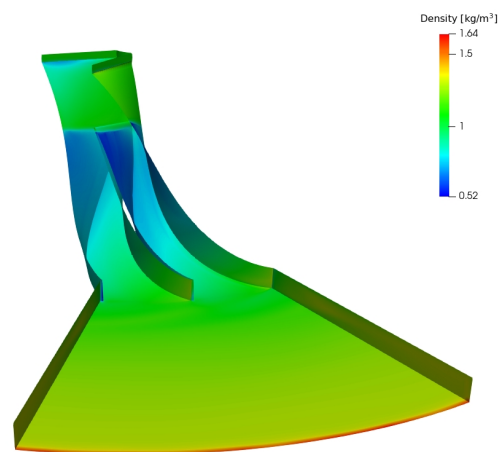


Slika 14: Raspodjela tlaka na cijeloj geometriji.

Iduće slike predstavljaju rezultate za nenominalnu točku. Slika 15. i slika 16. odnose se na uvjete u kojima dolazi do zagušenja strujanja.



Slika 15: Raspodjela tlaka kod zagušenja toka.



Slika 16: Raspodjela gustoće kod zagušenja toka.

Chapter 1

Introduction

1.1 Turbomachinery

The definition of a turbomachinery according to Dicks [5] "A machine that exchanges energy between the continuous flow of a working fluid and a continuously rotating blade system, where the energy exchange is based on flow-generated forces". In the most common scenario, the energy is harvested from the rotating component, eg. rotor. The possible working fluids are: water, steam or vapour, air, gas or refrigerant in cooling applications. Turbomachines may be further classified into two categories. First are those which utilise the energy to increase fluid pressure, eg. compressors and pumps. The second group of machines harvest energy by expanding the flow to a lower pressure and transforming it to other types of energy, eg. mechanical. The best example in this category is the turbine, which transforms the kinetic energy of the working fluid into rotating motion.

Turbomachines can also be categorised according to the direction of the flow: radial, axial and mixed flow. In radial machines, the flow of the fluid is perpendicular to axis of rotation. Axial machines have fluid flow parallel to the axis of rotation, while mixed flow machines have components of both radial and axial flows. Another criterion to classify turbomachinery can be by examining the flow streamlines around the rotor. Closed type or enclosed machines are machines where the rotor is enclosed in a casing or shrouded in such a way that the flow cannot escape from pressure to suction side of the blade across the tip of the blade, eg. compressors, centrifugal pumps and turbo-pumps. Open type or extended machines are the machines where

the flow can leak over the tip of the blade, eg. wind turbines and ship propellers [9].

Compressors are classified in a similar way, according to working principles. There are two main types, positive displacement compressors and dynamic compressors. Positive displacement compressors operate by sucking in a volume of gas through an inlet, reducing the working volume by mechanical work and finally forcing the gas out through an outlet. Furthermore, positive displacement compressors are divided into rotary and reciprocating types, eg. screw compressors, vane compressors and rotating vane compressors. Some authors tend to call reciprocating compressors piston compressors, since they use a piston driven by crankshaft to compress the gas and increase the pressure at the outlet. The main difference are the valves on the inlet and outlet manifold. They are used in a wide variety of fields, eg. HVAC, oil industry, chemical industry, etc. Finally, the last category which is closely related to this thesis is the group of dynamic compressors, further classified according to the flow direction: radial, axial and mixed flow. In axial compressors the fluid flow is essentially parallel to the axis of rotation and there are multiple stages which consist of rotor and stator blades. Radial compressors are more commonly referred as centrifugal compressors. The commonly accepted name for the disk is impeller, this term is exclusively used in turbomachinery only for centrifugal machines.

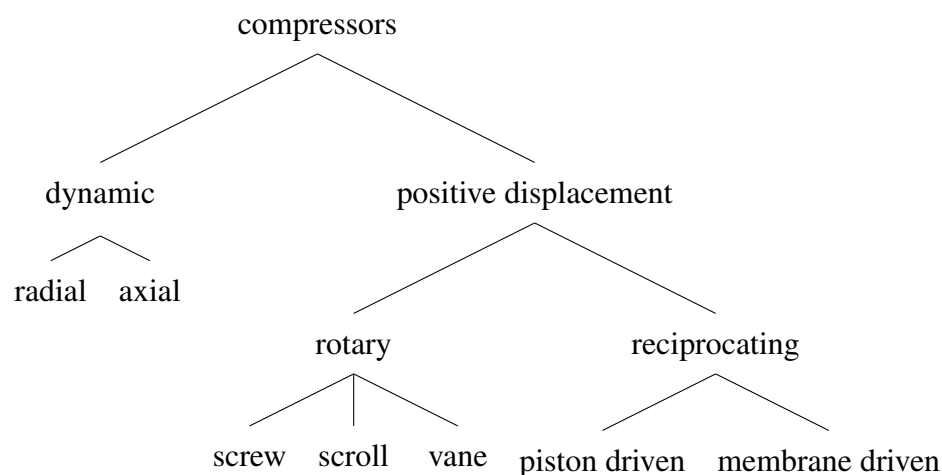


Figure 1.1.1: Compressors classification.

A fundamental difference between radial and axial compressors is that radial compressors, for equal external diameters, handle a lower flow rate, but achieve a larger stage work. In the case of axial compressors, 75% of the frontal area may be available for through-flow at a 50% radius

ratio, with an axial velocity up to about 50% of the blade speed on the average radius at about 40% of the tip speed. A flow coefficient defined with the frontal area and the peripheral speed thus may reach about 30%. The flow area with a radial compressor covers about 45% of the frontal area with a through-flow velocity maximally about 0.15. With an axial compressor, the working coefficient on the average radius is at a max of about 40%. Related to tip speed it is maximally about 0.3. With a radial compressor, the working coefficient may reach about 0.9 when applying radial end blades.

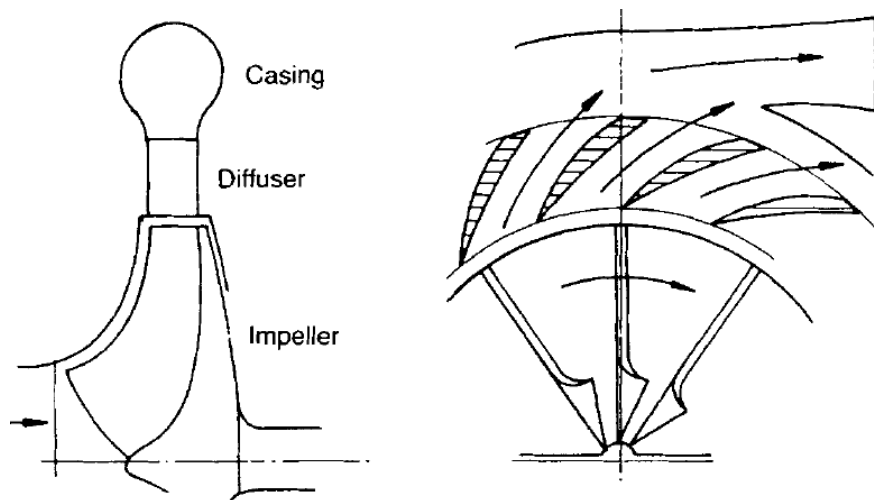


Figure 1.1.2: Simple centrifugal compressor [1].

The efficiency of an axial compressor is significantly better than that of a radial one. The isentropic total to total efficiency is about 0.92 at the maximum compared to about 0.84 for the centrifugal compressor with the open rotor and backswept blades. The efficiency improves with more backward sweep and closed rotors to a maximum of 0.87. The main reason is that flow is very inhomogeneous at the rotor outlet of the radial compressor, caused by turbulence segregation by the Coriolis force. The Coriolis force drives high energy cores within the turbulent motion from suction to the compression side. This leads to lowered velocity field near the suction side. The inhomogeneity of the rotor outlet flow causes a significant mixing loss downstream of the rotor. Secondly, rotors with radial end blades or with a slight backward sweep, eg. machines intended for high work, require significant velocity reduction in diffuser downstream of the rotor. A strong deceleration inevitably creates a large loss. A third reason is due to leakage loss within the open impeller [5].

The basic equations defining the flow are the Euler equations. In Fig. 1.1.2, the motion of

the fluid is indicated by the the arrow and it is picked up and operated upon by the rotor and discharged into the casing at a higher level of energy. The rotor has imparted both a velocity and a radial position change to the fluid, which together result in momentum changes and resultant forces on the rotor. Since momentum changes in the tangential direction give rise to torque and thus to work, a moment of momentum equations for elemental areas of flow at the points of entry and exit should be written. The normal fluid velocities are \mathbf{V}_{n1} and \mathbf{V}_{n2} . If elemental areas of flow da_1 and da_2 are examined, the moments of momentum entering the rotor at 1 and 2 are given:

$$dM_1 = (\rho \mathbf{V}_{n1} da_1) \mathbf{V}_{u1} R_1, \quad (1.1.1)$$

$$dM_2 = (\rho \mathbf{V}_{n2} da_2) \mathbf{V}_{u1} R_2. \quad (1.1.2)$$

Thus the total moments of momentum are:

$$M_1 = \int \rho \mathbf{V}_{n1} \mathbf{V}_{u1} R_1 da_1, \quad (1.1.3)$$

$$M_2 = - \int \rho \mathbf{V}_{n2} \mathbf{V}_{u2} R_2 da_2. \quad (1.1.4)$$

Subscripts 1 and 2 correspond to the entering and exit plane of the control volume. The fluid torque is the net effect given by:

$$T = M_1 + M_2, \quad (1.1.5)$$

$$T = \int \rho \mathbf{V}_{n1} \mathbf{V}_{u1} R_1 da_1 - \int \rho \mathbf{V}_{n2} \mathbf{V}_{u2} R_2 da_2, \quad (1.1.6)$$

It is assumed that $\mathbf{V}_u R = \text{const.}$ across each surface. Substitution $\dot{m} = \int \rho \mathbf{V}_n da$ into Eqn. (1.1.6), gives:

$$T = \dot{m}(\mathbf{V}_{u1} R_1 - \mathbf{V}_{u2} R_2). \quad (1.1.7)$$

In compressible, the flow density does change considerably and it is necessary to relate enthalpy changes into equations.

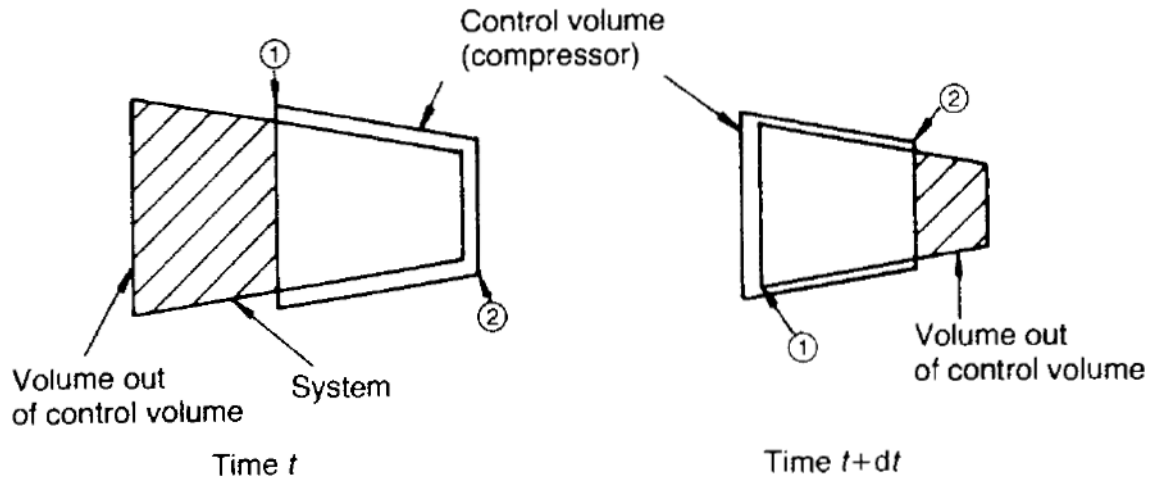


Figure 1.1.3: Compressor control volume [1].

Suppose that a compressor corresponds to the control volume in Fig. 1.1.3 and that the fluid system moves through the control volume in time dt as sketched. If the heat added in the time interval is dQ and the work extracted is dW , then the first law of thermodynamics applied to the system at time t and time $t + dt$ from Fig. 1.1.3 yields:

$$dQ - dW = \underbrace{(E_B - E_A)}_{\text{internal energy change}} + \underbrace{(me_2 - me_1)}_{\text{internal energy difference}} + \underbrace{(p_2mv_2 - p_1mv_1)}_{\text{net work done}}. \quad (1.1.8)$$

In the case of steady flow, the first bracket is zero, and the second and third can be rewritten in terms of enthalpy, velocity, and potential energy as follows:

$$dQ - dW = m \left[(h_2 - h_1) + \frac{\mathbf{V}_2^2 - \mathbf{V}_1^2}{2} + g*(Z_2 - Z_1) \right]. \quad (1.1.9)$$

This can be expressed in terms of work rate and mass flow rate. The elimination of heat exchange results, if stagnation enthalpy is used, in the equation:

$$W = \dot{m}(h_{02} - h_{01}), \quad (1.1.10)$$

or

$$W = \dot{m}C_p(T_{02} - T_{01}). \quad (1.1.11)$$

In a turbomachine.

$$W = \dot{m}(gH) = (\mathbf{u}_2\mathbf{V}_{u2} - \mathbf{u}_1\mathbf{V}_{u1})\dot{m}, \quad (1.1.12)$$

thus

$$C_p(T_{02} - T_{01}) = (\mathbf{u}_2\mathbf{V}_{u2} - \mathbf{u}_1\mathbf{V}_{u1}), \quad (1.1.13)$$

or

$$(h_{02} - h_{01}) = (\mathbf{u}_2 \mathbf{V}_{u2} - \mathbf{u}_1 \mathbf{V}_{u1}). \quad (1.1.14)$$

Thus stagnation enthalpy change relates to the velocity triangles. Isentropic efficiency statements may be written as total to total:

$$\eta_{TT} = \frac{h_{02s} - h_{01}}{h_{02} - h_{01}}, \quad (1.1.15)$$

or as static to static enthalpy:

$$\eta_{SS} = \frac{h_{2s} - h_1}{h_2 - h_1}. \quad (1.1.16)$$

The choice of efficiency depends on the system in which the compressor operates. Efficiency in Eqn. (1.1.15) is appropriate for situations where stagnation conditions at the inlet and outlet are real indices of performance. Eqn. (1.1.15) and Eqn. (1.1.16) are valid for the whole process of compression, however because of the divergence of the constant pressure lines, the sum of stage isentropic rises exceeds the overall rise. Thus, if η_p is the small stage efficiency, and η_c the overall efficiency:

$$\eta_p > \eta_c. \quad (1.1.17)$$

The preheat factor is given by:

$$\frac{\eta_p}{\eta_c} = \frac{\sum \text{stage rise}}{\text{overall rise}}. \quad (1.1.18)$$

The small stage or polytropic efficiency is given by:

$$\eta_p = \frac{dh_{is}}{dh} = \frac{v dp}{C_p dT} = \frac{RT dp}{C_p dT}. \quad (1.1.19)$$

Taking into consideration the relation:

$$C_p = \left(\frac{\gamma}{\gamma - 1}\right)R, \quad (1.1.20)$$

integrating Eqn. (1.1.19) for the compressor yields:

$$\frac{T_2}{T_1} = \left(\frac{p_2}{p_1}\right)^{\frac{\gamma-1}{\eta_p \gamma}}, \quad (1.1.21)$$

or in case of the ideal compression process, $\eta_p = 1$,

$$\frac{T_{2s}}{T_1} = \left(\frac{p_2}{p_1}\right)^{\frac{\gamma-1}{\gamma}}. \quad (1.1.22)$$

1.2 Previous and Related Studies

CFD simulations of turbomachinery are now a part of the standard approach in the design process. However, CFD as an investigation tool in the later stages of the design process, namely to investigate off-design operating points and fluid flow instabilities are rarely used. The main objective of this work is to investigate the applicability of CFD software, eg. open-source library foam-extend to predict the flow field corresponding to off-design operating conditions of a centrifugal compressor. Since a full rotor geometry is challenging to model due to the size of the computational mesh, we decided to investigate performing the simulations on a single blade passage using cyclic boundary conditions for non-conforming meshes (Generalised Grid Interface – GGI). The mesh is block-structured, created in Pointwise with 7.2 million cells. A Multiple Reference Frame approach is used to which means that the obtained flow field corresponds to a single rotor position. Start-up of the simulation is very sensitive due to the extreme operating conditions of the nominal operating-point, and it is necessary to change the boundary conditions gradually. Thus, the total pressure ratios and MRF angular velocity are increased progressively to prevent the simulation from crashing due to local extreme velocities and pressure values. To validate the simulation approach, a comparison is made to experimental and numerical data provided in the paper [8]. The final objective is to create a compressor map with the established flow field features corresponding to different operating points, some close surge and choke conditions. The interest in researching these topics began in the 1970s [10], and continues until today with numerous scientific publications [7, 11, 12, 13].

1.3 Scope of the Thesis

The main objective of the Thesis is to investigate the possibilities of using compressible solvers for predicting the off-design operating points of centrifugal compressors. To achieve the objective specific CFD tools for turbomachinery applications have been applied. All simulations were run in the open source CFD software foam-extend.

1.4 Thesis Outline

The Thesis is divided in to six chapters. In Chapter 1 an introduction is given as well as the classification of the compressors. In Chapter 2 the governing equations are presented and the discretisation trough the Finite Volume Method, as well as the mathematical model of turbulence models. In Chapter 3 specific extensions of the CFD method used in turbomachinery are described, with description of the domain and interface handling. In Chapter 4 an overview of the geometry and computational domain. Finally, in Chapter 5 results and discussion are presented. Conclusion with the possible future work are given in Chapter 6.

Chapter 2

Finite Volume Method

Almost every flow described with CFD can be divided into one of the two categories: compressible and incompressible. In incompressible flows, density change is mostly neglected. Density changes are minimal and do not affect significantly the solution of numerical simulation. The challenge is where is needed to take into account density change. The most distinguished criteria to evaluate the type of flow is based on the Mach number. In general, all subsonic flows are considered incompressible, but after the Mach number of 0.3 density change can't be neglected any more. Detailed classification of flows based on Mach number is given in Table 2.0.1. The flow inside radial compressors must be considered as a compressible flow.

The mathematical model of the steady compressible turbulent simulation in a centrifugal compressor is based on the laws of conservation of physical properties which is significant for a specific given problem. Parallel with conservation laws, we need to provide additional relations to solve a mathematical problem.

Table 2.0.1: Flow Classification based on Mach number [3].

Flow Type	Mach Number
Low Subsonic	0 - 0.3
High Subsonic	0.3 - 0.6
Transonic	0.6 - 1.1
Supersonic	1 - 5
Hypersonic	>5

2.1 Introduction

In the previous chapter, a short overview of turbomachinery and classification of compressors was given. In this chapter the Finite Volume Method and the mathematical model will be presented. It is divided into three parts, discretisation of a scalar transport equation using Finite Volume Method, turbulence modelling and governing equations of the compressible single-phase, turbulent fluid flow.

2.2 Scalar Transport Equation

The Reynolds Transport Theorem (RTT), also known as the Leibniz–Reynolds Transport Theorem, when applied to a region of interest, can be used to analyse the rate of change of some general property ϕ in that specific region, which we call the control volume (CV). The CV is a closed volume of space where the rate of change of property ϕ is equal to sum of the change of property inside the CV and the rate of outflow through surfaces which enclose the CV. RTT applied to a CV, eg. the one in Fig. 2.4.1 may be written as [3]:

$$\frac{d}{dt} \int_{V_m} \phi dV = \int_{V_m} \frac{\partial \phi}{\partial t} dV + \oint_{S_m} \phi (\mathbf{n} \cdot \mathbf{U}) dS. \quad (2.2.1)$$

Gauss Theorem can be applied to transform the surface integral from Eqn. (2.2.1) :

$$\int_{V_P} \nabla \cdot \mathbf{a} dV = \oint_{\partial V_P} d\mathbf{s} \cdot \mathbf{a} = \oint_{\partial V_P} d\mathbf{n} \cdot \mathbf{a} dS. \quad (2.2.2)$$

When Eqn. (2.2.2) is applied to Eqn. (2.2.1), the RTT volume integral form:

$$\frac{d}{dt} \int_V \phi dV = \int_V \left[\frac{\partial \phi}{\partial t} + \nabla \cdot (\phi \mathbf{U}) \right] dV. \quad (2.2.3)$$

Eqn. (2.2.3) is used to model the convective transport of a general property ϕ facilitated by convective velocity \mathbf{u} . The inflow and the outflow of general property ϕ is distinguished as $(\mathbf{u} \cdot \mathbf{n}) < 0$ for the inflow, and for the outflow $(\mathbf{u} \cdot \mathbf{n}) > 0$, where \mathbf{n} is the surface normal vector.

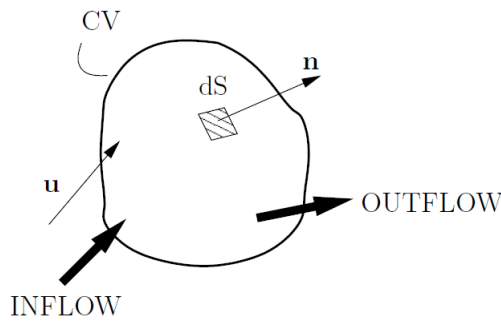


Figure 2.2.1: Closed system or Control Volume (CV) [2].

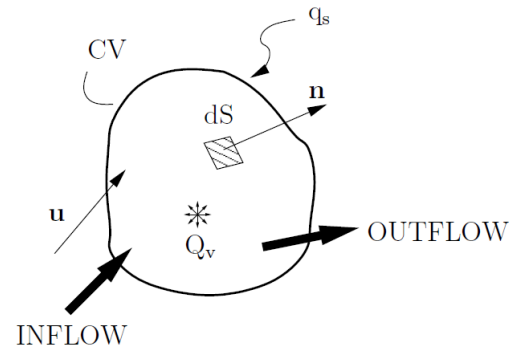


Figure 2.2.2: Surface and Volume sources of the CV [2].

Alongside the convective transport, surface and volume sources also contribute to the change of a general property inside a CV. The contribution of surface and volume sources is shown in Eqn. (2.2.2), and is represented by the equation:

$$\frac{d}{dt} \int_V \phi dV = \int_V q_v dV - \oint_S (\mathbf{n} \cdot \mathbf{q}_s) dS. \quad (2.2.4)$$

Applying the Gauss Theorem to the source term in Eqn. (2.2.4), and inserting Eqn. (2.2.4) instead of the Eqn. (2.2.3) and integrating it over CV with the constant volume assumption ($V = const.$) yields:

$$\frac{\partial \phi}{\partial t} + \nabla \cdot (\phi \mathbf{U}) = q_v - \nabla \cdot \mathbf{q}_s. \quad (2.2.5)$$

These terms represent surface sources, which act on a surface S of the selected CV. A general property ϕ in a closed domain (CV) would be transported from regions of higher concentration to regions with lower concentration until it becomes equal in the whole CV. The diffusion model is built on a fact that $\nabla \phi$ points in the direction of higher concentration of property ϕ and that the diffusive transport occurs in the opposite direction, where the intensity is governed by the diffusivity γ [3]:

$$\mathbf{q}_s = -\gamma \nabla \phi. \quad (2.2.6)$$

Inserting Eqn. (2.2.6) into Eqn. (2.2.5) and rearranging the equation members, yields the general form of the Scalar Transport Equation:

$$\underbrace{\frac{\partial \phi}{\partial t}}_{\text{temporal derivative}} + \underbrace{\nabla \cdot (\phi \mathbf{U})}_{\text{convection term}} - \underbrace{\nabla \cdot (\gamma \nabla \phi)}_{\text{diffusion term}} = \underbrace{q_v}_{\text{source term}}. \quad (2.2.7)$$

The temporal derivative in Eqn. (2.2.7) represents the inertia of the system. Inertia can be described as the potential of the system (CV) to accumulate the general property ϕ . Convection term can be presented as a coordinate transformation, on the amount of the property ϕ which is transported into and out of the system with the convective velocity \mathbf{U} . The diffusion term represents the gradient transport of the property ϕ . Source or sink terms define the local production or destruction of the general property ϕ .

2.3 Governing Equations

Eqn. (2.2.7) is one of the fundamental equations in continuum mechanics. It describes how a scalar quantity is transported through space. When the general property ϕ is replaced with some other properties, other transport equations may be written.

2.3.1 Conservation of Mass

If the general property ϕ is substituted with the density of fluid, ρ (specific mass) in Eqn. (2.2.7) and the source term is neglected, the equation describes the conservation of mass:

$$\frac{\partial \rho}{\partial t} + \nabla \cdot (\rho \mathbf{U}) = 0. \quad (2.3.1)$$

If the flow is incompressible, density is constant, $\rho = \text{constant}$, and Eqn. (2.3.1) can be further simplified, as follows:

$$\nabla \cdot \mathbf{U} = 0. \quad (2.3.2)$$

Conservation of mass in Eqn. (2.3.2) is the continuity equation.

2.3.2 Conservation of Energy

If the general property ϕ from Eqn. (2.2.7) is substituted with the specific internal energy ρe and the source (or sink) term is equal to all forces which act onto the CV, taking into account the specific heat flux \mathbf{q} and the volumetric heat source Q , the equation for conservation of energy can be written as:

$$\frac{\partial(\rho e)}{\partial t} + \nabla \cdot (\rho e \mathbf{U}) = \underbrace{\rho \mathbf{g} \cdot \mathbf{U}}_{\text{power of gravity force}} + \underbrace{\nabla \cdot (\boldsymbol{\sigma} \cdot \mathbf{U})}_{\text{power of surface forces}} - \underbrace{\nabla \cdot \mathbf{q} + \rho Q}_{\text{net heat flux}}. \quad (2.3.3)$$

2.3.3 Conservation of Momentum

If the general property ϕ from Eqn. (2.2.7) is substituted with the linear momentum vector ϕu , the equation describing conservation of linear momentum is written as:

$$\frac{\partial \rho u}{\partial t} + \nabla \cdot (\rho u \mathbf{u}) = \underbrace{\rho g}_{\text{gravitation force}} + \underbrace{\nabla \cdot \boldsymbol{\sigma}}_{\text{surface forces}}. \quad (2.3.4)$$

In the case of incompressible flow, the change in density is neglected, $\rho = \text{constant}$. Besides constant density, gravitation forces are also usually neglected. If all previous statements are considered, Eqn. (2.3.4) can be transformed in to:

$$\underbrace{\frac{\partial u}{\partial t}}_{\text{local production}} + \underbrace{\nabla \cdot (uu)}_{\text{convection term}} - \underbrace{\nabla \cdot (\mathbf{v}_{\text{eff}} \nabla \mathbf{U})}_{\text{diffusion}} = - \underbrace{\nabla \frac{p}{\rho}}_{\text{pressure gradient}}. \quad (2.3.5)$$

In Eqn. (2.3.5) Cauchy stress tensor is written as a sum of the pressure gradient ∇p and the viscous stress tensor which exist in the diffusion term. Velocity U in Eqn. (2.3.5) can be a transporting and a transported variable, thus making the convection term non-linear [3]. The continuity equation and the momentum equation represents the Navier-Stokes equations for incompressible flow.

2.4 Finite Volume Equations Discretisation

Since in many engineering applications the integral values (forces, force coefficients, power, torque) are the most relevant pieces of information, it is sufficient to approximate the solution of the governing equations. Thus, the solution is calculated as a discrete field of values obtained by solving a linear system. The linear system is assembled via the Finite Volume discretisation of the integral form of the governing equations. The discretisation in this Thesis will be carried out using the terminology and procedures introduced by Jasak in [14]. In foam-extend, the discretisation is based on the Polyhedral Finite Volume Method which consist of the following next steps [3]:

1. Discretisation of space is conducted by constructing a computational mesh of the spatial domain.
2. Discretisation through a time is made of series of time-steps which cover the observed time interval.
3. An assumption of spatial and temporal variation of ϕ are required for a discrete representation of the field data.
4. Integration of the discrete operator over a cell (CV) is conducted.
5. Per operator discretisation is made by visiting each operator, explicitly following the predetermined methodology and discretising it.
6. Spatial and temporal variations are used for the interpretation of the operator in discrete terms.

The main objective of the discretisation process is to define space and time domains which will be used. Spatial domain is represented with finite number of control volumes or in CFD vocabulary called just cells. On Fig. 2.4.1 is represented typical convex polyhedral control volume.

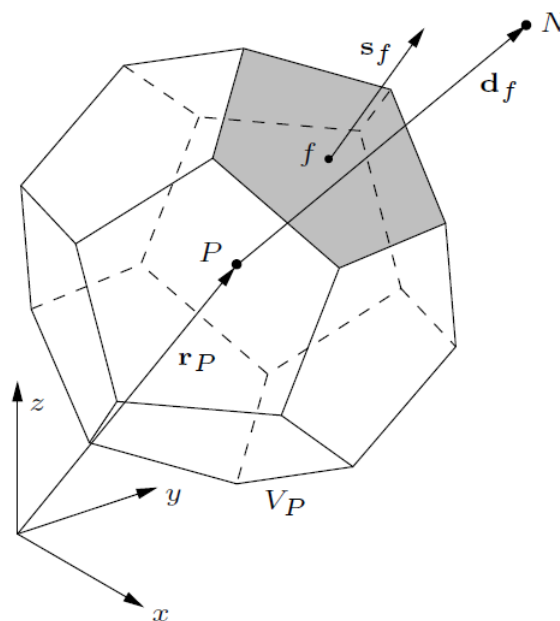


Figure 2.4.1: Convex polyhedral control volume [3].

The polyhedral cell with the corresponding volume V_p is defined with a cell centroid P and the centroid position vector \mathbf{r}_p , whose origin in the origin is of the global coordinate system. On a cell face f , the surface normal vector is \mathbf{s}_f and its magnitude is equal to the area of selected face f . For the cell, there exists exactly one neighbouring cell across each face. The neighbouring cell and its cell centre are marked with N and they are connected to the centroid of the main cell P via the "delta" vector $\mathbf{d}_f = \overline{PN}$ [3]. The definition of the the cell centroid P reads:

$$\int_{V_p} (\mathbf{x} - \mathbf{x}_p) dV = \mathbf{0}. \quad (2.4.1)$$

The face centre f is defined in the same manner,

$$\int_{S_f} (\mathbf{x} - \mathbf{x}_f) dS = \mathbf{0}. \quad (2.4.2)$$

Faces on polyhedral cells are usually not flat surfaces, thus the surface normal vector \mathbf{S}_f needs to be calculated from the integral:

$$\mathbf{S}_f = \int_{S_f} \mathbf{n} dS. \quad (2.4.3)$$

Solutions of equations are stored in the cell centroid. Boundary data are stored at the face centres of the boundary faces. In some situations, it is necessary to access the data which are located in the face centres of the cell. To achieve that interpolation schemes from cell centers to cell faces are used. The spatial variation of a general property ϕ in space is assumed to be linear:

$$\phi(\mathbf{x}) = \phi_P + (\mathbf{x} - \mathbf{x}_P) \cdot (\nabla \phi)_P. \quad (2.4.4)$$

Second order temporal discretisation in time is also assumed:

$$\phi(t + \Delta t) = \phi^t + \Delta t \left(\frac{\partial \phi}{\partial t} \right)^t. \quad (2.4.5)$$

Value of ϕ at the centroid is $\phi_P = \phi(\mathbf{x}_P)$ and the value of ϕ at time-instance t is $\phi^t = \phi(t)$. The volume integral can be evaluated using Eqn. (2.4.4):

$$\begin{aligned}
\int_V \phi dV &= \int_V [\phi_P + (\mathbf{x} - \mathbf{x}_P) \cdot (\nabla \phi)_P] dV \\
&= \phi_P \int_V dV + (\nabla \phi)_P \cdot \int_V (\mathbf{x} - \mathbf{x}_P) dV \\
&= \phi_P V_P.
\end{aligned} \tag{2.4.6}$$

Surface integrals can be evaluated in the same way as before:

$$\begin{aligned}
\oint_S \mathbf{n} \phi dS &= \sum_f \int_{S_f} \mathbf{n} \phi_f dS_f \\
&= \sum_f \int_{S_f} \mathbf{n} [\phi_f + (\mathbf{x} - \mathbf{x}_f) \cdot (\nabla \phi)_f] dS_f \\
&= \sum_f \mathbf{s}_f \phi_f.
\end{aligned} \tag{2.4.7}$$

Scalar Transport Eqn. (2.2.7) is discretised term by term, starting from the integral form of the equation:

$$\int_V \frac{\partial \phi}{\partial t} dV + \oint_S \phi (\mathbf{n} \cdot \mathbf{u}) dS - \oint_S \gamma (\mathbf{n} \cdot \nabla \phi) dS = \int_V Q_v dV. \tag{2.4.8}$$

The result is the transformation of the equation from differential form into a set of linear equations which are solved in the matrix form.

2.4.1 Linear System of Equations

The basis for discretisation of linear equations is the scalar transport Eqn. (2.2.7). For every computational point, a linear equation needs to be solved for each unknown variable. The solution depends on the values in the neighbouring cell centroids N . General form of an equation in the linear system for a cell P is:

$$a_P x_P + \sum_N a_N x_N = \mathbf{b}. \tag{2.4.9}$$

At every time step in which x_P depends on itself, a contribution is added into a_P , and when x_N depends on itself, contribution is added into a_N . Other contributions are added into b . Eqn. (2.4.9) written for all cells in the domain can be assembled into a system of linear equations, which in matrix form can be written as:

$$[A] [\mathbf{x}] = [\mathbf{b}]. \tag{2.4.10}$$

In Eqn. (2.4.10), $[A]$ is coefficient matrix, $[\mathbf{x}]$ is the unknown vector which contains values of x_P and vector $[\mathbf{b}]$ represents the right-hand side. The dimension of matrix $[A]$ can be very large because it consists of $N \times N$ coefficients and it is a square matrix. Usually, only a small number of coefficients are non-zero, which is employed for reducing memory overhead by choosing the appropriate storage format.

2.4.2 Discretisation of the Temporal Derivative

Time derivative in Eqn. (2.4.8) represents the rate of change of general property ϕ , discretised as:

$$\frac{\partial \phi}{\partial t} = \frac{\phi^n - \phi^o}{\Delta t}. \quad (2.4.11)$$

Eqn. (2.4.11) is the first order approximation of the temporal derivative. The time step size Δt can be calculated from equation:

$$\Delta t = t_{new} - t_{old}. \quad (2.4.12)$$

The value of variable ϕ calculated in the previous time step t_{old} is defined with:

$$\phi^o = \phi(t = t_{old}), \quad (2.4.13)$$

while the value of variable ϕ calculated in a new time step t_{new} is defined with:

$$\phi^n = \phi(t = t_{new}). \quad (2.4.14)$$

Second order approximation of the temporal derivative can be written as follows:

$$\frac{\partial \phi}{\partial t} = \frac{\frac{3}{2}\phi^n - 2\phi^o + \frac{1}{2}\phi^{oo}}{\Delta t}, \quad (2.4.15)$$

where ϕ^{oo} is the value of ϕ from the time step preceding ϕ^o .

Eqn. (2.4.11) and Eqn. (2.4.15) are integrated over the volume, are to obtain:

$$\int_V \frac{\partial \phi}{\partial t} dV = \frac{\phi^n - \phi^o}{\Delta t} V_P, \quad (2.4.16)$$

$$\int_V \frac{\partial \phi}{\partial t} dV = \frac{\frac{3}{2}\phi^n - 2\phi^o + \frac{1}{2}\phi^{oo}}{\Delta t} V_P. \quad (2.4.17)$$

2.4.3 Discretisation of the Convection Term

To discretise the convection term from Eqn. (2.4.8), Gauss Theorem needs to be used, Eqn. (2.2.2), to transform the volume integral into the surface integral:

$$\int_V \nabla \cdot (\phi \mathbf{u}) dV = \oint_S \phi (\mathbf{n} \cdot \mathbf{u}) dS. \quad (2.4.18)$$

Using same principle of integration as before, surface integral is written as the sum over the faces of CV:

$$\oint_S \phi (\mathbf{n} \cdot \mathbf{u}) dS = \sum_f \phi_f (\mathbf{s}_f \cdot \mathbf{u}_f) = \sum_f \phi_f F, \quad (2.4.19)$$

where ϕ_f is the value of ϕ at the cell face, F represents the face flux:

$$F = \mathbf{s}_f \cdot \mathbf{u}_f. \quad (2.4.20)$$

Since flux F can be calculated as a product of the surface normal vector \mathbf{s}_f and the convective velocity \mathbf{u}_f , thus the value of property ϕ_f needs to be evaluated on the face using ϕ_P and ϕ_N .

The two standard interpolation schemes are [3]:

1. **Central differencing** - which is second order accurate, but causes oscillations,

$$\phi_f = f_x \phi_P + (1 - f_x) \phi_N, \quad (2.4.21)$$

$f_x = \overline{fN}/\overline{PN}$, P and N are cell centroids shown in Fig. 2.4.1 .

2. **Upwind differencing** - this type takes into account information which comes from upstream, it does not produce oscillations, but it smears the solution:

$$\phi_f = \max(F, 0) \phi_P + \min(F, 0) \phi_N. \quad (2.4.22)$$

2.4.4 Discretisation of the Diffusion Operator

Discretisation of the diffusion term can be achieved with the same method as in the previous section:

$$\begin{aligned} \oint_S \gamma (\mathbf{n} \cdot \nabla \phi) dS &= \sum_f \int_{S_f} \gamma (\mathbf{n} \cdot \nabla \phi) dS \\ &= \sum_f \gamma_f \mathbf{s}_f \cdot (\nabla \phi)_f. \end{aligned} \quad (2.4.23)$$

Diffusivity γ_f is evaluated at the face centres using the central differencing scheme, $\mathbf{s}_f \cdot (\gamma\phi)_f$ describes the face-normal gradient and it can be calculated as:

$$\mathbf{s}_f \cdot (\gamma\phi)_f = |\mathbf{s}_f| \frac{\phi_N - \phi_P}{|\mathbf{d}_f|}. \quad (2.4.24)$$

The gradient is assumed to align with the direction of the vector \mathbf{d}_f . Eqn. (2.4.24) is valid only for orthogonal meshes, eg. if the mesh is non-orthogonal, a correction term needs to be applied to the discrete diffusion term.

2.4.5 Discretisation of Source and Sink Terms

Source and sink terms cause local effects, they are modelled with the function of time and space or any other complex variable q_v . Discretised equation then should be:

$$\int_V q_v dV = q_v V_P, \quad (2.4.25)$$

where:

$$q_v(\phi) = q_v + q_d \phi. \quad (2.4.26)$$

Term q_d is described as follows:

$$q_d = \frac{\partial q_v(\phi)}{\partial \phi}. \quad (2.4.27)$$

2.5 Compressible Navier-Stokes Equations

In this section overview of the compressible flow equations will be given. The starting point is the compressible continuity equation, Eqn. (2.3.1). The compressible form of the momentum equation can be written as:

$$\frac{\partial(\rho\mathbf{u})}{\partial t} + \nabla \cdot (\rho\mathbf{u}\mathbf{u}) - \nabla \cdot [\mu(\nabla\mathbf{u} + (\nabla\mathbf{u})^T)] = -\nabla(P + \frac{2}{3}\mu\nabla \cdot \mathbf{u}). \quad (2.5.1)$$

The internal energy equation which is derived from Eqn. (2.3.3) states:

$$\frac{\partial(\rho e)}{\partial t} + \nabla \cdot (\rho e\mathbf{u}) - \nabla \cdot (\lambda\nabla T) = \rho\mathbf{g} \times \mathbf{u} - \nabla \cdot (P\mathbf{u}) - \nabla \cdot (\frac{2}{3}\mu(\nabla \cdot \mathbf{u})\mathbf{u}) + \nabla \cdot [\mu(\nabla\mathbf{u} + (\nabla\mathbf{u})^T) \times \mathbf{u}]. \quad (2.5.2)$$

Density ρ , pressure p and the temperature T are connected via the equation of state of an ideal gas:

$$\rho = \frac{P}{RT} = \psi P, \quad (2.5.3)$$

Where ψ stands for compressibility:

$$\psi = \frac{1}{RT}. \quad (2.5.4)$$

The system of equations is closed with the relations for the transport coefficients λ and μ which are general functions of thermodynamic state variables:

$$\lambda = \lambda(P, T), \quad (2.5.5)$$

$$\mu = \mu(P, T). \quad (2.5.6)$$

Derivation of Compressible Pressure Equation

The rate of change $\frac{\partial \rho}{\partial t}$ can be expanded, using the chain rule as follows:

$$\frac{\partial \rho}{\partial t} = \frac{\partial \rho}{\partial P} \frac{\partial P}{\partial t} + \frac{\partial \rho}{\partial T} \frac{\partial T}{\partial t}. \quad (2.5.7)$$

It should be noted that the second term, $\frac{\partial \rho}{\partial T} \frac{\partial T}{\partial t}$ introduces a source term which is dependent on the rate of change of temperature. Introduction of this source term enables the general polytropic change of state. The formal derivation relies on the substitution of the Eqn. (2.5.3) into Eqn. (2.5.7). For the ideal gas, the equation has the following form:

$$\frac{\partial \rho}{\partial P} = \psi. \quad (2.5.8)$$

Discretisation of the momentum equation is identical to the discretisation of the incompressible momentum equation as described at [14]:

$$a_p^U \mathbf{u}_p = \mathbf{H}(\mathbf{u}) - \nabla p. \quad (2.5.9)$$

In the divergence term, \mathbf{u} is substituted and ρ should be presented in the term of P :

$$\nabla \cdot (\rho \mathbf{u}) = \nabla \cdot \left[\rho (a_p^U)^{-1} \nabla P \right]. \quad (2.5.10)$$

The first term, which is under divergence is converted into a convection term, using $\rho = \psi P$ as follows:

$$\nabla \cdot \left[\rho (a_p^U)^{-1} \mathbf{H}(\mathbf{u}) \right] = \nabla \cdot \left[\psi P (a_p^U)^{-1} \mathbf{H}(\mathbf{u}) \right] = \nabla \cdot (\mathbf{F}_p P). \quad (2.5.11)$$

Term \mathbf{F}_p represents the velocity which has a feature in convective flux effects in pressure:

$$\mathbf{F}_p = \psi ((a_p^U)^{-1} \mathbf{H}(\mathbf{u})). \quad (2.5.12)$$

It should be noted that unlike the divergence of the mass flux, divergence of \mathbf{F}_p is not zero, because no conservation law applies to it:

$$\nabla \cdot \mathbf{F}_p \neq 0. \quad (2.5.13)$$

Eqn. (2.5.11) can be altered to obtain the final form of the compressible pressure equation:

$$\frac{\partial(\psi P)}{\partial t} + \underbrace{\nabla \cdot [\psi(a_p^U)^{-1} \mathbf{H}(\mathbf{u})P]}_{\text{convective effects}} - \underbrace{\nabla \cdot [\rho(a_p^U)^{-1} \nabla P]}_{\text{pressure Laplacian equivalent}}. \quad (2.5.14)$$

2.6 Boundary Conditions

Boundary conditions are used to isolate the system from the rest of environment and limit what is modelled [3]. Choosing the right type and location of the boundary condition depends on the physics of the case and the experience of user. Boundary conditions will contribute to the discretisation through prescribed behaviour. Some of the most frequently used numerical boundary conditions are:

1. Dirichlet Boundary Condition - prescribes fixed boundary value of ϕ ,

$$\phi = \text{constant}. \quad (2.6.1)$$

2. Von Neumann Boundary Condition - value of gradient of ϕ is prescribed and projected on the boundary face area vector [15]:

$$\mathbf{n} \cdot \mathbf{q}_s = 0. \quad (2.6.2)$$

3. Mixed (Robin) Boundary Condition - combination of Neumann and Dirichlet boundary conditions, in which Dirichlet contributes with α and Neumann with $(1 - \alpha)$.

4. Geometric and coupled boundary conditions:

- Symmetry plane - enforces using mirror a image of the internal solution;
- Cyclic and periodic - couples near-boundary-cells to cells on the other boundary.

2.7 Turbulence Modelling

Every flow encountered in engineering practice becomes unstable above a certain Reynolds number. At low Reynolds numbers the flows are laminar, while the higher Reynolds numbers flows are observed to become turbulent. A chaotic and random state of motion develops in which the velocity and pressure change continuously. However, the physics of turbulence is completely understood and described in detail. Turbulence can be characterised with higher diffusion rates and increased drag, sometimes this phenomenon is appreciated, but usually it is detrimental for the process performance. Turbulence can be visualised through vortex dynamics. Large scale vortices are created by the flow and through the process, the vortices stretch and break up into smaller vortices. In this way the energy is transported from larger to smaller scales. Dissipation of energy in the system is proportional to the velocity gradient, which is the highest in the smallest vortices.

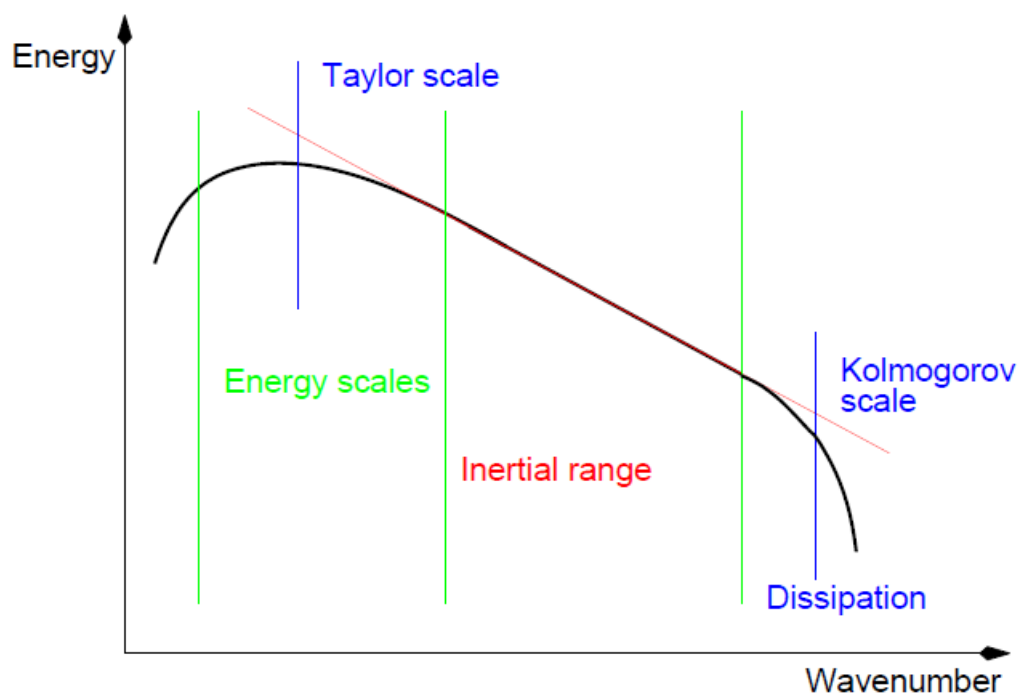


Figure 2.7.1: Vortex dynamics and energy cascade [3].

In Fig. 2.7.1 *wavenumber* on the abscissa axis describes the number of vortices that can fit into space. Wavenumber is divided into four regions: large scale vortices which are affected by the flow type and global flow field are difficult to distinguish since they can be coherent

structure or actual turbulence. Taylor scale comprises vortices which carry the highest amount of the turbulent kinetic energy. Inertial scale is where stretching of the vortices can be described with the inertial effects of vortex breakup and viscous effects can be neglected. Small vortices contain a small proportion of overall energy, but they still contribute to dissipation. This is also the smallest relevant scale in turbulent flows, characterised by the Kolmogorov micro-scale.

Turbulent flows are governed by the Navier-Stokes equations. The stochastic nature of turbulent flow makes modelling very challenging. The challenge of turbulence modelling is to create models and manipulate equations to be able to simulate interactions for specific conditions [3]. Despite the complexity, there is a number of analytical results for turbulence flow types. Since Reynolds-Averaged two-equations models are used in the scope of this thesis, they will be outlined in the following section.

2.7.1 Reynolds-Averaged Navier-Stokes Equations (RANS)

The RANS model is frequently used in engineering applications and the main advantage over Direct Numerical Simulations (DNS), and Large Eddy Simulations (LES) is that the computer resources needed are a couple of orders of magnitude smaller. RANS equations may be assembled by decomposing values of pressure and velocity into mean and fluctuating components:

$$\mathbf{u} = \bar{\mathbf{u}} + \mathbf{u}', \quad (2.7.1)$$

$$p = \bar{p} + p', \quad (2.7.2)$$

where $\bar{\mathbf{u}}$ is the mean component of velocity. Substituting Eqn. (2.7.1) and Eqn. (2.7.2) into Eqn. (2.3.5) and eliminating all terms containing products of mean and fluctuating values, the following equations are obtained:

$$\frac{\partial \bar{\mathbf{u}}}{\partial t} + \nabla \cdot (\bar{\mathbf{u}} \bar{\mathbf{u}}) - \nabla \cdot (\nu \nabla \bar{\mathbf{u}}) = -\nabla \bar{p} + \nabla \cdot (\overline{\mathbf{u} \mathbf{u}'}), \quad (2.7.3)$$

$$\nabla \cdot \bar{\mathbf{u}} = 0. \quad (2.7.4)$$

Term $\overline{\mathbf{u} \mathbf{u}'}$ is called the Reynolds stress tensor and it is second rank symmetric tensor.

$$\mathbf{R} = \overline{\mathbf{u} \mathbf{u}'}. \quad (2.7.5)$$

In order to close the system of equations, \mathbf{R} needs to be described as a function of the solution. There are two methods of doing it:

1. Write an algebraic function which yields eddy viscosity models:

$$\mathbf{R} = f(\bar{\mathbf{u}}, \bar{p}). \quad (2.7.6)$$

2. Add more differential equations, eg. introducing a transport equation for \mathbf{R} and producing Reynolds Transport Models, however as new equations are introduced, the problem from the previous example will arise and an algebraic function will have to be devised at some point.

Both options are used today, first one more often. Using turbulent viscosity ν_t and symmetric velocity gradient $\bar{\mathbf{S}}$, \mathbf{R} can be written as:

$$\mathbf{R} = \nu_t \frac{1}{2} [\nabla \bar{\mathbf{u}} + (\nabla \bar{\mathbf{u}})^T]. \quad (2.7.7)$$

The term on the right in squared brackets is the tensor \mathbf{S} . Turbulent viscosity ν_t is calculated using dimensionless constant A which allows the model to be tuned with the actual physical behaviour, velocity scale \mathbf{U} and length scale Δ :

$$\nu_t = A U \Delta. \quad (2.7.8)$$

The velocity scale can be approximated relatively easy using turbulent kinetic energy $U \approx |\mathbf{u}'|$, where turbulent kinetic energy k is:

$$k = \frac{3}{2} \mathbf{u}'^2. \quad (2.7.9)$$

Since RANS approach is used in the Thesis two two-equation models will be described: the k - ω model and the k - ω SST model. Two equation models are popular because they account for transport of both the velocity and length scale, and they can also be tuned to produce canonical results.

k- ω model

There are two differential equations which describe turbulence, first equation is describing the turbulence kinetic energy k :

$$\frac{\partial k}{\partial t} + \nabla \cdot (\bar{\mathbf{u}} k) - \nabla \cdot [(\nu_{eff}) \nabla k] = G - \varepsilon, \quad (2.7.10)$$

in which term G is represented with:

$$G = \nu_t \left[\frac{1}{2} (\nabla \bar{\mathbf{u}} + \nabla \bar{\mathbf{u}}^T) \right]^2. \quad (2.7.11)$$

The second equation describes the dissipation of turbulent kinetic energy:

$$\frac{\partial \varepsilon}{\partial t} + \nabla \cdot (\bar{\mathbf{u}} \varepsilon) - \nabla \cdot [(\nu_{eff} \nabla \varepsilon)] = C_1 G \frac{\varepsilon}{k} - C_2 \frac{\varepsilon^2}{k}, \quad (2.7.12)$$

Where ν_t is defined as:

$$\nu_t = C_\mu \frac{k^2}{\varepsilon}. \quad (2.7.13)$$

Term G used in Eqn. (2.7.11) is also valid for Eqn. (2.7.12).

k- ω SST model

The k- ω sst model a combination of the k- ω model and the k- ε model. Original formulation was developed by Wilcox [16] and the two-equation eddy viscosity model was developed by Menter as described in [17] and in [18]. The standard k- ε model is used in free stream conditions while k- ω is used next to the wall conditions. The two equations which describes model are:

$$\frac{\partial k}{\partial t} + \nabla \cdot (\bar{\mathbf{u}} k) - \nabla \cdot [(\nu_{eff} \nabla k)] = \min(G, C_1, \beta^* k \omega) - \beta^* k \omega, \quad (2.7.14)$$

$$\frac{\partial \omega}{\partial t} + \nabla \cdot (\bar{\mathbf{u}} \omega) - \omega \nabla \cdot \bar{\mathbf{u}} - \nabla \cdot [(\nu_{rff} \nabla \omega)] = \gamma \min[S_2, \frac{c_1}{a_1} \beta^* \omega \max(a_1 \omega, b_1 F_{23} \sqrt{S_2})] - \beta \omega^2 + (1 - F_1) CD_{k\omega}. \quad (2.7.15)$$

Eqn. (2.7.14) describe the transport of turbulent kinetic energy k and Eqn. (2.7.15) describes the transport of specific dissipation rate ω . Terms G and ν_t used in previous equations are defined as:

$$G = \nu_t S_2, \quad (2.7.16)$$

$$S_2 = 2 \left[\frac{1}{2} (\nabla \bar{\mathbf{u}} + \nabla \bar{\mathbf{u}}^T) \right]^2, \quad (2.7.17)$$

$$\nu_t = \frac{a_1 k}{\max[a_1 \omega, b_1 F_{23} \sqrt{2} \left| \frac{1}{2} (\nabla \bar{\mathbf{u}} + \nabla \bar{\mathbf{u}}^T) \right|]}. \quad (2.7.18)$$

Eqn. (2.7.14) and Eqn. (2.7.15) are form the work of Menter and Esch [19] while the coefficients are from [20]. Term F_3 was added as Hellsten describes in [21].

2.8 Closure

An overview of the discretisation using the Finite Volume Method was given in this Chapter. Turbulence models and pressure velocity coupling algorithm for compressible flow were also briefly explained. In the following Chapter the CFD methods for the turbomachinery will be presented as well as the addition to the compressible pressure-velocity system.

Chapter 3

Applications of CFD Methods in Turbomachinery

3.1 Introduction

In the previous chapter an overview of the Finite Volume Method was given, with a more detailed description of the segments used in the making of this Thesis. In this chapter an overview of the specific methods used in turbomachinery CFD simulations will be given, as well as the information about domain manipulation methods and interface handling methods.

3.2 Domain Handling

The decision on the way in which the domain is approached is based on a few simple criteria. The first is the type of flow, whether it is a steady-state or a transient problem. The steady-state approach in turbomachinery is also called the *Frozen Rotor* approach, due to fact that none of the geometry is moving. Here, the rotation of the domain is modelled by including additional terms into equations of motion for the rotating region [4]. The advantages of this approach are the robustness and fewer computer resources are required than with the other models. The drawback of the model is the inadequate prediction of local and transient flow phenomena and the results are sensitive to the relative position of the rotor and stator for tightly coupled components.

For transient simulations, the Frozen Rotor approach cannot be used anymore. For transient

flow, the Moving Mesh Model or Dynamic Mesh Model is applied. The main disadvantage is that the model requires more computational resources, but however not due to an additional set of equations for compensating topological changes of the computational domain. The difference of dynamic mesh in transient simulations to static mesh in transient simulations is just around 5% of computational resources used per time step [3].

3.2.1 Multiple Reference Frame

The Multiple Reference Frame approach is a way of representing the flow around moving parts in turbomachinery simulations as a steady-state problem. That kind of representation can be achieved by selecting cells in the computational domain and adding inertia caused by rotational movement. The set of equations used to describe the motion of mesh reference frame are modified by adding terms of acceleration which occurs due to transformation from stationary to the moving reference frame [4].

In cases when the entire zone can be modelled as a single moving zone, a Single Reference Frame (SRF) is used. An example is shown in figure 3.2.1. It represents a cut-out of a rotor geometry.

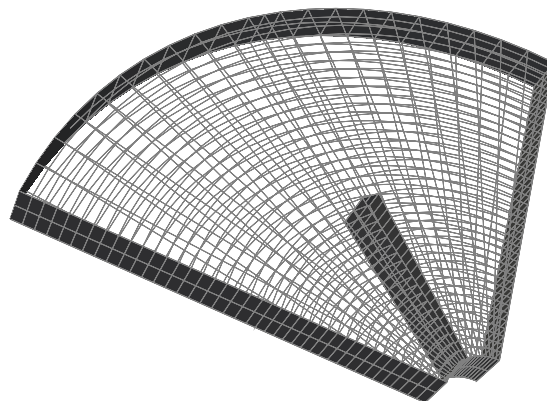


Figure 3.2.1: Single Frame of Reference [2].

For most turbomachinery, a single moving zone is not adequate, since the geometry of turbomachines has both moving and stationary zones, eg. rotors and stators in compressors and turbines. In these cases, the Multiple Reference Frame (MRF) approach is used. With the MRF approach, the computational domain can be divided into different zones which can be assigned either a stationary or the rotational frame of reference. A common practice is to include a small part of the mesh near the rotating part of the machine as a rotating frame of reference, which was used in this thesis as well. The detailed description of the computational domain is given in the next chapter.

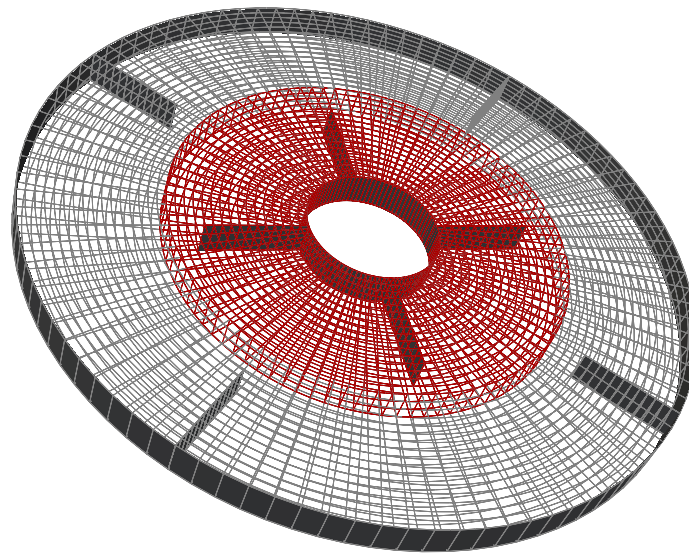


Figure 3.2.2: Multiple Frame of Reference [2].

Application of MRF approach is shown in Fig. 3.2.2 where the cells in the rotating zone are shown in red.

Single Reference Frame (SRF)

As previously described, SRF is used only when the entire computational domain is moving. An example from the field of turbomachinery would be a single blade row, with the assumption that the flow is rotationally periodic and by prescribing periodic boundary conditions on rotational periodic boundaries, Fig. 3.2.3.

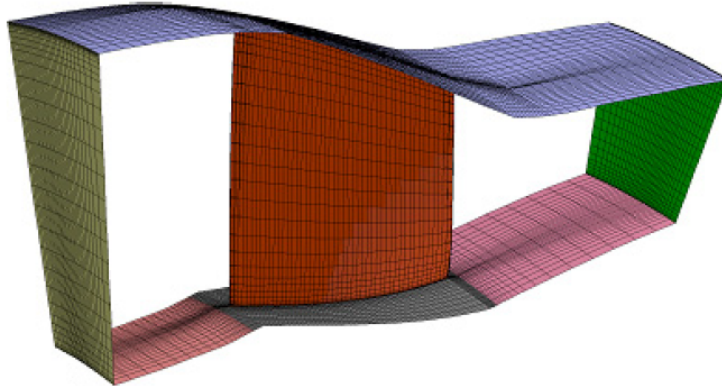


Figure 3.2.3: Single blade model with rotationally periodic boundaries [4].

As described in [22] when a general vector \mathbf{Z} is inserted into an inertial frame of reference, vector $\boldsymbol{\omega}$ is added to account for angular velocity:

$$\left[\frac{d\mathbf{Z}}{dt} \right]_I = \left[\frac{d\mathbf{Z}}{dt} \right]_R + \boldsymbol{\omega} \times \mathbf{Z}. \quad (3.2.1)$$

By exchanging the general vector \mathbf{Z} with the position vector \mathbf{r} , the following equation can be written:

$$\left[\frac{d\mathbf{r}}{dt} \right]_I = \left[\frac{d\mathbf{r}}{dt} \right]_R + \boldsymbol{\omega} \times \mathbf{r}. \quad (3.2.2)$$

The temporal derivation of the position vector \mathbf{r} corresponds to the velocity vector in inertial or relative frame:

$$\mathbf{u}_I = \mathbf{u}_R + \boldsymbol{\omega} \times \mathbf{r}, \quad (3.2.3)$$

where \mathbf{u}_I and \mathbf{u}_R represent absolute and relative velocity, respectively. Substituting the position vector \mathbf{r} into Eqn. (3.2.1), yields:

$$\left[\frac{d\mathbf{u}_I}{dt} \right]_I = \left[\frac{d\mathbf{u}_I}{dt} \right]_R + \boldsymbol{\omega} \times \mathbf{u}_I, \quad (3.2.4)$$

\mathbf{u}_I on the right hand side in Eqn. (3.2.4) can be replaced with Eqn. (3.2.3):

$$\left[\frac{d\mathbf{u}_I}{dt} \right]_I = \left[\frac{d[\mathbf{u}_R \times \boldsymbol{\omega} + \mathbf{r}]}{dt} \right]_R + \boldsymbol{\omega} \times [\mathbf{u}_R + \boldsymbol{\omega} \times \mathbf{r}]. \quad (3.2.5)$$

After sorting the terms, acceleration for the inertial frame of reference can be written as:

$$\left[\frac{d\mathbf{u}_I}{dt} \right]_I = \left[\frac{d\mathbf{u}_R}{dt} \right]_R + \frac{d\boldsymbol{\omega}}{dt} \times \mathbf{r} + 2\boldsymbol{\omega} \times \mathbf{u}_R + \boldsymbol{\omega} \times \boldsymbol{\omega} \times \mathbf{r}. \quad (3.2.6)$$

$\frac{d\boldsymbol{\omega}}{dt} \times \mathbf{r}$ is the tangential acceleration, $2\boldsymbol{\omega} \times \mathbf{u}_R$ represents the Coriolis acceleration and $\boldsymbol{\omega} \times \boldsymbol{\omega} \times \mathbf{r}$ represents the centrifugal acceleration. Equations (2.3.2) and (2.3.4) in the form inertial frame form are the incompressible Navier-Stokes equation for the inertial reference frame:

$$\begin{cases} \frac{D\mathbf{u}_I}{Dt} = \nabla \cdot (\mathbf{v}_{eff} \nabla \mathbf{u}_I) - \nabla \frac{p}{\rho} \\ \nabla \cdot \mathbf{u}_I = 0. \end{cases} \quad (3.2.7)$$

By expressing the material derivative as a sum of local and convective rates of change and using the continuity equation $\nabla \cdot \mathbf{u}_I = 0$, incompressible Navier Stokes equation for the inertial frame can be written as:

$$\begin{cases} \frac{\partial \mathbf{u}_I}{\partial t} + \nabla \cdot (\mathbf{u}_I \mathbf{u}_I) - \nabla \cdot (\mathbf{v}_{eff} \nabla \mathbf{u}_I) = -\nabla \frac{p}{\rho} \\ \nabla \cdot \mathbf{u}_I = 0. \end{cases} \quad (3.2.8)$$

The left side of the momentum equation (3.2.7) combined with Eqn. (3.2.6) yields:

$$\frac{D\mathbf{u}_I}{Dt} = \frac{D\mathbf{u}_R}{Dt} + \frac{d\boldsymbol{\omega}}{dt} \times \mathbf{r} + 2\boldsymbol{\omega} \times \mathbf{u}_R + \boldsymbol{\omega} \times \boldsymbol{\omega} \times \mathbf{r}. \quad (3.2.9)$$

The continuity equation must be satisfied at every moment. According to the previous statement, $\nabla \cdot \mathbf{u}_I = 0$ and $\nabla \cdot \mathbf{u}_R = 0$ stems from $\nabla \cdot (\boldsymbol{\omega} \times \mathbf{r}) = 0$. This simplification should be used to transform the diffusion term in Eqn. (3.2.8) into the form which is more adequate for the rotating reference frame. However, before the transformation, Eqn. (3.2.3) should be taken into account:

$$\begin{aligned} \nabla \cdot \nabla (\mathbf{u}_I) &= \nabla \cdot \nabla [\mathbf{u}_R + \boldsymbol{\omega} \times \mathbf{r}] = 0 \\ &= \nabla \cdot \nabla (\mathbf{u}_R) + \underbrace{\nabla \cdot \nabla (\boldsymbol{\omega} \times \mathbf{r})}_{=0}. \end{aligned} \quad (3.2.10)$$

After replacing $\frac{D\mathbf{u}_I}{Dt}$ from Eqn. (3.2.7) with Eqn. (3.2.8) and taking into account Eqn. (3.2.10), yields:

$$\begin{cases} \frac{\partial \mathbf{u}_R}{\partial t} + \frac{d\boldsymbol{\omega}}{dt} \times \mathbf{r} + 2\boldsymbol{\omega} \times \mathbf{u}_R + \boldsymbol{\omega} \times \boldsymbol{\omega} \times \mathbf{r} + \nabla \cdot (\mathbf{u}_R \mathbf{u}_R) = \nabla \cdot (\mathbf{v}_{eff} \nabla \mathbf{u}_R) - \nabla \frac{p}{\rho} \\ \nabla \cdot \mathbf{u}_R = 0. \end{cases} \quad (3.2.11)$$

Since in the steady-state simulations, which are used with Moving Reference Frame methods, temporal derivatives are neglected the following is obtained:

$$\begin{cases} \nabla \cdot (\mathbf{u}_R \mathbf{u}_R) + 2\boldsymbol{\omega} \times \mathbf{u}_R + \boldsymbol{\omega} \times \boldsymbol{\omega} \times \mathbf{r} = \nabla \cdot (\mathbf{v}_{eff} \nabla \mathbf{u}_R) - \nabla \frac{p}{\rho} \\ \nabla \cdot \mathbf{u}_R = 0. \end{cases} \quad (3.2.12)$$

Eqn. (3.2.12) is the incompressible Navier-Stokes equation for the rotating frame of reference. To achieve the results to be as close as possible to the real values, boundary conditions must be correctly applied, and the following conditions should be fulfilled as well [4]. Walls which lie on the boundary can assume any shape as long as they are moving with the rotating reference frame, while walls which do not move can be defined in the stationary coordinate system, however these walls must be surfaces of revolution about the axis of rotation. When dealing with large rotational speeds, a high degree of coupling between the momentum equations may occur. A high degree of rotation causes a large radial pressure gradient which is driving the flow in axial and radial directions and this behaviour influences the formation of the swirl or rotation in the field. This kind of coupling may lead to instabilities in the solution, and in order to eliminate these instabilities, several solution techniques can be applied [4]:

1. For pressure-based solver only : changing the frame in which the velocities are solved by changing the velocity formulation settings.
2. Mesh must be sufficiently refined to be able to resolve large gradients of pressure and swirl velocity.
3. For pressure-based, segregated solvers only : Under-relaxation factors shall be reduced for the velocity (a good estimate would be 0.3 to 0.5 and even lower).
4. Start the simulation with lower rotational speed and increase it gradually to the final condition.

Looking at the most common turbomachinery geometries, SRF is rarely used without significant simplifications. A more applicable approach would be Multiple Frame of Reference because the geometry domain does not need to correspond with surfaces of rotation anymore. It may have rotational and stationary zones.

Multiple Reference Frame (MRF)

The Multiple Reference Frame method is a steady-state approximation in which individual cell zones can be assigned with different motion. The flow in each zone can be solved using the modified equations for moving reference frames with the terms corresponding which define different rotation or translation. If the zone is stationary, equations are reduced to their stationary

forms. At the interfaces between zones, a local reference frame transformation is performed to enable the flow from one zone to be used to calculate the fluxes at the boundary of the neighbor zone. The drawback of the MRF model is that it does not take into account the relative motion of the moving zone concerning neighbour zones, as the mesh remains fixed for the computation. This approach is analogue with freezing the moving part in a specific position and observing the flow field with the rotor in that position, thus MRF is also often referred to as the frozen rotor approach. Although MRF is an approximation, it can still give a useful model of the flow in turbomachinery applications. Usage of MRF can be extended to the transient simulations. It can be used for computing flow fields which can be applied as an initial condition for the transient sliding mesh simulations.

The governing equations for the MRF approach can be derived using the same principle as for the SRF method. Eqn. (3.2.12) shall be further developed according to [22] as:

$$\begin{aligned}
\nabla \cdot (\mathbf{u}_R \mathbf{u}_R) &= \nabla \cdot (\mathbf{u}_R [\mathbf{u}_I - \boldsymbol{\omega} \times \mathbf{r}]) \\
&= \nabla \cdot (\mathbf{u}_R \mathbf{u}_I) - \underbrace{\nabla \cdot \mathbf{u}_R}_{0} (\boldsymbol{\omega} \times \mathbf{r}) - \underbrace{\mathbf{u}_R \nabla \cdot (\boldsymbol{\omega} \times \mathbf{r})}_{\boldsymbol{\omega} \times \mathbf{u}_R} \\
&= \nabla \cdot (\mathbf{u}_R \mathbf{u}_I) - \boldsymbol{\omega} \times \mathbf{u}_R.
\end{aligned} \tag{3.2.13}$$

Equation (3.2.13) inserted into the left hand side of the momentum equation (3.2.12) transforms into:

$$\begin{aligned}
\nabla \cdot (\mathbf{u}_R \mathbf{u}_R) + 2\boldsymbol{\omega} \times \mathbf{u}_R + \boldsymbol{\omega} \times \boldsymbol{\omega} \times \mathbf{r} &= \nabla \cdot (\mathbf{u}_R \mathbf{u}_I) - \boldsymbol{\omega} \times \mathbf{u}_R + 2\boldsymbol{\omega} \times \mathbf{u}_R + \boldsymbol{\omega} \times \boldsymbol{\omega} \times \mathbf{r} \\
&= \nabla \cdot (\mathbf{u}_R \mathbf{u}_I) + \boldsymbol{\omega} \times \mathbf{u}_R + \boldsymbol{\omega} \times \boldsymbol{\omega} \times \mathbf{r} \\
&= \nabla \cdot (\mathbf{u}_R \mathbf{u}_I) + \boldsymbol{\omega} \times (\mathbf{u}_R + \boldsymbol{\omega} \times \mathbf{r}) \\
&= \nabla \cdot (\mathbf{u}_R \mathbf{u}_I) + \boldsymbol{\omega} \times \mathbf{u}_I.
\end{aligned} \tag{3.2.14}$$

Taking into account Eqn. (3.2.10) and newly formed Eqn. (3.2.14), the governing equations used in MRF approach are:

$$\begin{cases} \nabla \cdot (\mathbf{u}_R \mathbf{u}_I) + \boldsymbol{\omega} \times \mathbf{u}_R = \nabla \cdot (\mathbf{v}_{eff} \nabla \mathbf{u}_I) - \nabla \frac{p}{\rho} \\ \nabla \cdot \mathbf{u}_R = 0. \end{cases} \tag{3.2.15}$$

This equation is an incompressible Navier-Stokes equation for the rotating frame of reference with absolute velocity. Eqn. (3.2.15) is used for solving fluid flow in the rotating MRF zone.

To solve the inertial (stationary) zone, the derivation stems from Eqn. (3.2.8):

$$\begin{cases} \nabla \cdot (\mathbf{u}_I \mathbf{u}_R) - \nabla \cdot (v_{eff} \nabla \mathbf{u}_I) = -\nabla \frac{p}{\rho} \\ \nabla \cdot \mathbf{u}_I = 0. \end{cases} \quad (3.2.16)$$

Although this approach is very applicable and robust, some limitations still exist [4].

- The interfaces which connect stationary to a moving region must be oriented such that the component of the frame velocity normal to the boundary is zero. This means that the in translation moving frame, translational velocity vector, and moving zones boundaries must be parallel. In the case of rotational motion, the interfaces must be surfaces of revolution about the axis of rotation defined by the fluid zone.
- Multiple Reference Frames should only be used in steady-state simulations.
- Translational and rotational velocities are assumed constant in time.
- Axisymmetric swirl can not be accurately modelled.
- The relative velocity formulation can not be used in combination with MRF or mixing models.

To summarize, the MRF method is a go-to choice for fast and robust modelling turbomachinery with different rotating or translating parts. It can produce results in cases without the strong influence of transients. It can not be used for the transient simulations, where in the case of the Moving Mesh approach should be used.

3.2.2 Moving Mesh

Dynamic mesh handling includes deforming mesh cases in which the number and connectivity of the mesh remain intact, while during the topological changes, mesh size and connectivity varies during the simulation. As in most turbomachinery, the control volume is determined by the fixed geometry boundaries. Solution-dependent mesh motion is not commonly practice to use in turbomachinery. A detailed description of mesh movement using FVM and the governing equations is described by Jasak in [23] and will not be discussed in this Thesis since it was not used.

3.3 Interface Handling

To join multiple regions into a single continuous computational domain, interfaces which connect the regions via interpolation are introduced. A discontinuous domain may be the product of geometry which consists of several regions which do not match perfectly, eg. the interface between a single blade passage of rotor and stator in axial turbo compressor. To overcome the challenge of generating complex meshes, interfaces can be applied even though it would be possible to create a single domain. Special interfaces are used when only a part of a circumferentially periodic geometry is simulated. In this case, only the part of the domain which encompasses the repetitive part of the geometry is chosen for simulations, eg. a single blade passage of the rotor in a centrifugal compressor. Using a single passage produces the results only for the part of the geometry, but the results can be assumed cyclic for the specific degree as a segment of a full 360° geometry. Interfaces available in openFOAM will be described in the following section as they were used in this Thesis.

3.3.1 General Grid Interface

General Grid Interface (GGI) connection is used where the mesh (faces, edges points) on either side of the connection is not aligned exactly. GGI connection allows non-matching node locations, element types, and even the flow physics across the connection [24]. GGI can be used to establish a connection between the mesh zone with the assigned relative rotation and the rest of the domain.

The main idea behind GGI is to enable coupling between non-conformal mesh regions at the level of discretization, without the need to use topological changes and re-meshing of cells next to the interface [24].

Governing Equations

The governing equations are calculated via weighted interpolation as the way of evaluating and transmitting flow values or any other variables across a pair of patches. Patches can be either conformal or non-conformal. The special form of interface discretisation is used, relying on GGI interpolation. Master and shadow patches are assigned to a pair of coupled patches with the flow values between them. These two patches are governed by equations derived from the

FVM discretisation [24]. For flow values or variables interpolated from master patch to the shadow patch:

$$\Phi_{S_i} = \sum_n W_{M_n \rightarrow S_i} \cdot \Phi_{M_n}. \quad (3.3.1)$$

Flow or variable values from the shadow patch to the master patch:

$$\Phi_{M_j} = \sum_m W_{S_m \rightarrow M_j} \cdot \Phi_{S_m}. \quad (3.3.2)$$

$W_{M_n \rightarrow S_i}$ and $W_{S_m \rightarrow M_j}$ are weighting factors, used for control of master and shadow patches.

In order to keep the interface discretisation conservative, the following conditions must be satisfied:

$$\sum_n W_{M_n \rightarrow S_i} = 1, \quad (3.3.3)$$

$$\sum_m W_{S_m \rightarrow M_j} = 1. \quad (3.3.4)$$

Along with Eqn. (3.3.3) and Eqn. (3.3.4), a product of patch surface area and weighting factor must be equal to the surface area of intersection between master and shadow patch:

$$W_{M_n \rightarrow S_i} \cdot |S_{M_n}| = W_{S_m \rightarrow M_j} \cdot |S_{S_m}| = |S_{\cap M \rightarrow S}|. \quad (3.3.5)$$

Additional terms in form of the symmetry constraint are:

$$\text{if } W_{M_n \rightarrow S_i} > 0 \quad \rightarrow \quad W_{S_m \rightarrow M_j} > 0, \quad (3.3.6)$$

and

$$W_{M_n \rightarrow S_i} \neq W_{S_m \rightarrow M_j}. \quad (3.3.7)$$

Simplified interpolation which does not strictly meet previously stated requirements would lead to unacceptable discretisation error [24]. Value of GGI weighting factors can be calculated from Eqn. (3.3.5).

For the master to shadow patch faceset:

$$W_{M_n \rightarrow S_i} = \frac{|S_{\cap M \rightarrow S_i}|}{|S_{M_n}|}, \quad \text{with } \in [0, 1]. \quad (3.3.8)$$

For the shadow to master patch faceset:

$$W_{S_m \rightarrow M_j} = \frac{|S_{\cap S \rightarrow M_j}|}{|S_{S_m}|}, \quad \text{with } \in [0, 1]. \quad (3.3.9)$$

The weighting factor described in Eqn. (3.3.8) and Eqn. (3.3.9) represents the percentage of surface intersection between two overlapping faces. It needs to be larger than zero, and in the extreme case of zero overlap, it would mean that there is no intersection between two given faces. Non-overlapping faces are treated as an error in the geometry and are reassigned to a symmetry plane boundary condition. Another borderline case would be when the weighting factor is one. This case could be treated by merging different regions of meshes.

overlapGgi

OverlapGgi is a modified form of the basic GGI. It is intended to be used in situations where an interface is not fully covered. For example a rotor-stator interface in an axial turbo compressor, where the stages of compressor have a different pitch which would result in uncovered faces, which fit together perfectly in reality, e.g. Fig. 3.3.1.

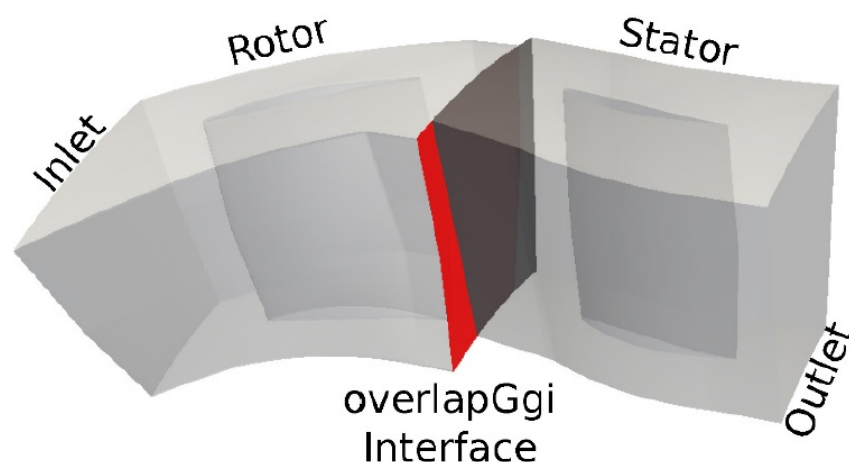


Figure 3.3.1: OverlapGgi interface of axial turbo compressor [4].

cyclicGgi

The main criteria to use cyclicGgi is that the geometry is periodically repetitive, eg. geometries of rotational bodies, which is widely applicable in turbomachinery. Both the basic cyclic and cyclicGgi boundary conditions could be used in repetitive geometry, but the main difference is that cyclic conditions must have identical mesh on the repetitive part. CyclicGgi allows the us-

age of not identical boundary domains. Cvijetić presented in [4] the advantages of the cyclicGgi over the cyclic boundary condition. Cyclic boundary conditions require both boundaries of periodic geometry to be defined as a single patch with one-half of the patches representing one side and the other half representing the second half, while CyclicGgi will store each boundary surface as a separate patch. The use of cyclicGgi does not require an interface to be flat as cyclic requires. Cyclic allows only meshes which match completely while as the cyclicGgi allows non-conformal boundary meshes, eg. Fig. 3.3.2:

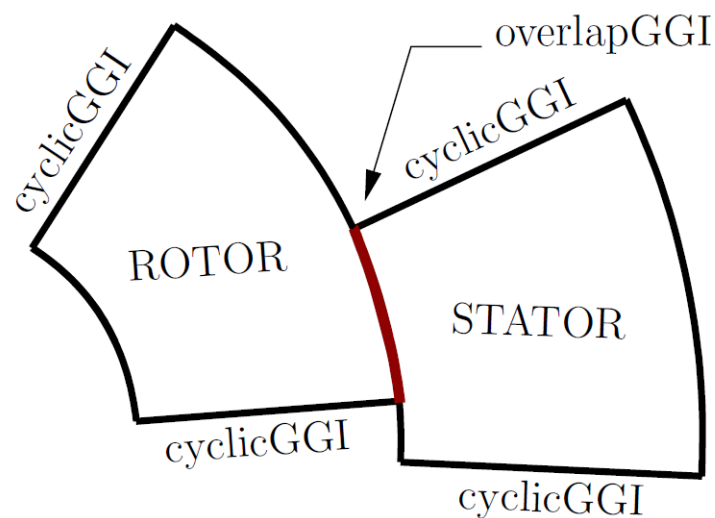


Figure 3.3.2: CyclicGgi interface [2].

CyclicGgi is assigned to the parts of geometry which are periodically repetitive and overlapGgi is assigned to the part which is partially covered by the both patches.

3.3.2 Mixing Plane

The mixing plane approach provides an alternative to the MRF model and sliding mesh models for simulating flow through domains with one or more regions that are in relative motion. As discussed before, the MRF model is only applicable when the flow between neighbour moving and stationary zones is almost uniform. In case the flow is not uniform, MRF would give a non-physical solution. On the other hand, the sliding mesh would be appropriate in this case but it is, as we mentioned, used for transient simulations. In the mixing plane approach, each zone is treated as a steady-state problem. Field data from neighbour zones are passed as boundary

conditions which are spatially averaged at the mixing plane interface. The operation of spatial averaging is also called mixing. The process of mixing removes any possible unsteadiness which could arise due to circumferential variations. Even though the mixing plane has specific simplifications, it can still provide the solution with satisfying results. There is a choice of different averaging methods: area-weighted averaging, mass averaging, and mixed-out averaging [4].

3.4 Closure

In this chapter an overview of specific tools implemented code *OpenFOAM* for turbomachinery simulations was given. The tools are divided into domain handling and interface handling. In the domain handling category the Frozen Rotor approach was described for steady-state simulations, while the moving mesh model is used for transient simulations. In interface handling, different approaches for connecting mesh regions are introduced. The focus was on methods used in this Thesis, such as different types of GGI-s.

In the following chapter an overview of a centrifugal turbo compressor which was simulated in this Thesis will be given.

Chapter 4

Geometry and Computational Domain

4.1 Introduction

Previous chapter gave an overview of specific tools implemented code *OpenFOAM* for turbomachinery simulations. The tools are divided into domain handling and interface handling. In the domain handling category the Frozen Rotor approach was described for steady-state simulations, while the moving mesh model is used for transient simulations. In interface handling, different approaches for connecting mesh regions are introduced. The focus was on methods used in this Thesis, such as different types of GGI-s.

In this chapter the characteristics of the centrifugal compressor investigated in the Thesis will be described. The process of assembling computational domain from provided geometry will also be described along with the boundary conditions. In the last section of the chapter simulation setup parameters will be outlined.

4.2 Centrifugal Compressor

Referring onto Section 1.1, where the basic working principles for rotating turbomachinery were given. Along with the previous equations, there are some additional equations to fully define the laws for rotating ducts.

4.2.1 Work and Energy Equations in a Rotating Frame

In this section the equations for work and energy in a rotating frame with constant angular velocity will be presented [5]. Additional two forces are introduced: centrifugal and Coriolis force. From Fig. 4.2.1, it follows:

$$\vec{v} = \vec{\Omega} \times \vec{r} + \vec{w}, \quad (4.2.1)$$

where $\vec{\Omega}$ is the angular velocity vector, \vec{r} is the coordinate vector of considered point **P** which originates from the origin of the rotation axis, and \vec{w} is the relative velocity. The differentiation of the velocity relation Eqn. (4.2.1) yields:

$$\vec{a} = \frac{d\vec{v}}{dt} = \vec{\Omega} \times (\vec{\Omega} \times \vec{r}) + 2\vec{\Omega} \times \vec{w} + \vec{a}_{rel}, \quad (4.2.2)$$

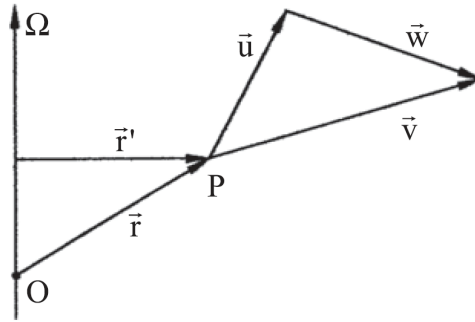


Figure 4.2.1: Relative and absolute velocities [5].

where \vec{a} and \vec{a}_{rel} represent the absolute and relative accelerations. The basic laws may thus be applied in the relative frame of reference, with the condition that the forces per mass unit are introduced:

$$\text{Centrifugal force: } \vec{C}_f = \Omega^2 \vec{r}', \quad (4.2.3)$$

$$\text{Coriolis force: } \vec{C}_o = -2\vec{\Omega} \times \vec{w}, \quad (4.2.4)$$

where \vec{r}' is the radial distance vector of point **P** measured from the axis of rotation. An additional term comes from the momentum equation:

$$\rho A dx \Omega^2 \vec{r}' \vec{I}_x = \rho A \Omega^2 r dr = \rho A \Omega d \frac{r^2}{2} = \rho A d \frac{u^2}{2}, \quad (4.2.5)$$

where \vec{r}' is exchange with \vec{r} and where $\mathbf{u} = \Omega r$ represents the blade speed. The Coriolis force does not contribute to the work along the streamline. Eqn. (4.2.5) multiplied with the velocity and divided by the mass flow rate follows:

$$d\frac{1}{2}\mathbf{w}^2 + \frac{1}{\rho}dp + dq_{irr} = dW + d\frac{1}{2}\mathbf{u}^2. \quad (4.2.6)$$

The centrifugal force contribution to the work along the streamline. The same contribution must be added to the energy equation. The work dW is zero on a rotor since forces affecting the rotor perform no work with the frame that is turning with the rotor. Gravitational potential energy is negligible, thus:

$$\text{Work: } d\frac{1}{2}\mathbf{w}^2 + \frac{1}{\rho}dp + dq_{irr} = d\frac{1}{2}\mathbf{u}^2, \quad (4.2.7)$$

$$\text{Energy: } dh + d\frac{1}{2}\mathbf{w}^2 = d\frac{1}{2}\mathbf{u}^2 + dq. \quad (4.2.8)$$

4.2.2 Moment of Momentum in the Absolute Frame

The meridional section of a rotating object is a section containing the axis of rotation. According to the mean line flow representation, there is no velocity component perpendicular to the average circumferential stream surface. The meridional velocity may be decomposed into an axial component \mathbf{v}_a and a radial component \mathbf{v}_r .

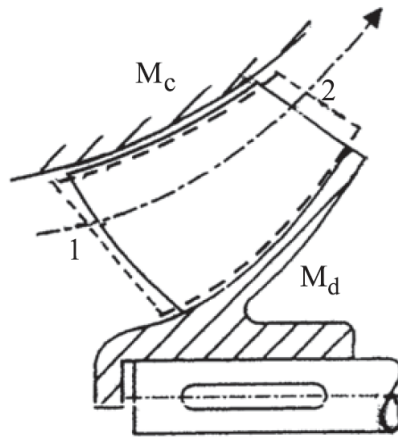


Figure 4.2.2: Meridional streamtube section for open rotor [5].

The flow moment can be divided into two parts:

$$M = M_b + M_c. \quad (4.2.9)$$

M_b part originates from the blade surfaces and the hub, the material rotor surfaces while M_c is the contribution by the casing. Both moments are considered as being exerted on the flow. M_b is positive and M_c is negative. The moment balance on the rotor is.

$$M_{shaft} - M_b + M_d = 0, \quad (4.2.10)$$

in which M_d represents the disc friction moment of the hub. Eqn. (4.2.10) with addition of Eqn. (4.2.9) can be rearranged into:

$$M_{shaft} = M - M_c - M_d. \quad (4.2.11)$$

It means that the shaft moment M_{shaft} is divided into two parts: the M_b part reaches the blades (the rotating machine parts) and the part $-M_d$ is absorbed by disc friction. Furthermore, the blade moment M_b is divided into two parts: the M part affects the flow and the $-M_c$ part is absorbed by the friction of the casing. After multiplication of Eqn. (4.2.11) with the angular velocity Ω , the following is obtained:

$$P_{shaft} = M\Omega - M_c\Omega - M_d\Omega. \quad (4.2.12)$$

The moment M_c is equal to the integral of the scalar product of the friction force $\vec{\tau} dS$ exerted on the flow and a unit vector parallel to the blade speed \vec{u} , multiplied with the radius. The shaft power is split into three parts: the part $M\Omega$ affects the flow, the part $-M_c\Omega$ is dissipated at the casing and the third part $-M_d\Omega$ is dissipated at the rotor disc. The term $-M_c\Omega$ is always positive and has the same nature as the term $-M_d\Omega$. With the relation between the absolute and the relative velocities $\vec{v} = \vec{u} + \vec{w}$, it follows:

$$M_c\Omega = \int \vec{\tau} \cdot \vec{u} dS = \int \vec{\tau} \cdot \vec{v} dS - \int \vec{\tau} \cdot \vec{w} dS. \quad (4.2.13)$$

The term with integrand $\vec{\tau} \cdot \vec{v}$ represents dissipation caused by the friction force on the casing. The term with integrand $\vec{\tau} \cdot \vec{w}$ is physically fictive but may be considered as the dissipation that would be generated if a friction force was acting in the relative frame. The difference between both terms may be considered as the disk friction dissipation due to the friction force acting on a fictitious shroud of the rotor. Division of Eqn. (4.2.12) with the mass flow rate, yields:

$$\Delta W_{shaft} = \Delta W + q_{irr}, \quad (4.2.14)$$

where $M\Omega = \dot{m}\Delta W$ and $-M_c\Omega - M_d\Omega = \dot{m}q_{irr}$.

4.2.3 Flow Instabilities

As mentioned before, there are two marginal conditions, choke and surge. The surge line is the limit of the stable operation of the compressor. It can be reached by reducing the flow rate in comparison with the design flow rate, at same rotational speed may generate stall and reversal flow may occur within the vanless diffuser. These phenomena generate losses, causing a decrease in the pressure ratio of the compressor. In the moment when the compressor goes into the surge, the effects are dramatic. They can be recognized due to increase in noise levels caused by the airflow and mechanical vibration [6]. Looking at the compressor map, surge line can be found as the line closest to the ordinate in Fig. 4.2.4.

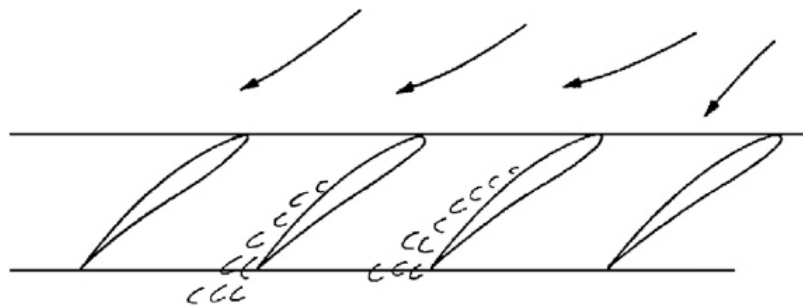


Figure 4.2.3: Mechanism of stall cell propagation [6].

Choking

Choke occurs when the process of compression does not create enough resistance to fluid flow and the compressor operates at a maximum flow rate for a given level of performance. Effects of the choke are generally ignored because there is typically no damage to the machine. Besides not taking damage, it is difficult to detect using a vibration monitoring system. The only indicator can sometimes be a change in noise frequency. The choke line is located far away from the ordinate line at the compressor map in Fig 4.2.4.

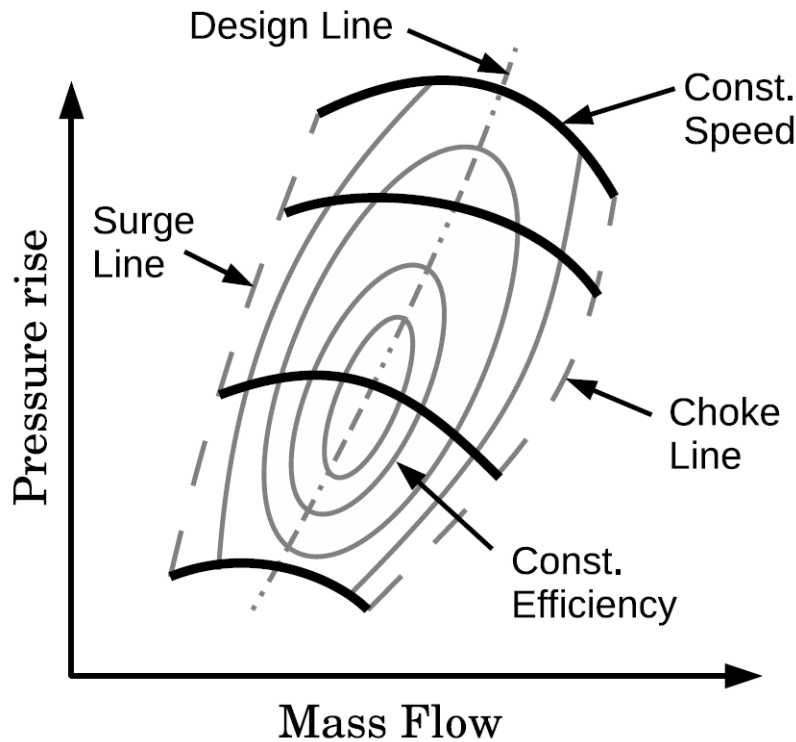


Figure 4.2.4: Centrifugal compressor map with highlight choke and surge line [7].

According to [5], mass flow rate with choking in the rotor is:

$$\dot{m}_c = A_1 \rho_{01} c_{01} \left(\frac{2}{\gamma + 1} \right)^{\frac{1}{n-1} + \frac{1}{2}} \left(1 + \frac{\gamma - 1}{2} \frac{u_1^2}{c_{01}^2} \right)^{\frac{1}{n-1} + \frac{1}{2}}, \quad (4.2.15)$$

where A_1 is the through flow area, n is the polytropic exponent, c_{01} is the velocity of sound. The choking flow rate depends on the rotational speed for both the rotor and stator. Attaining Mach number 1 occurs with backswept blades at diffuser inlet, as conditions are respectively approximately $u \approx \sqrt{\gamma RT}$, the velocity ratio is around $\frac{u_2}{u_1} \approx 2$, but the temperature ratio is less than 4. If the flow at the impeller outlet is highly supersonic, which occurs at large pressure ratios (greater than 6).

4.3 Computational Domain

The computational domain, eg. the FV mesh is the first step done in the simulation framework. The geometry from which the mesh was built on is the rotor impeller and stator housing previously studied by Dewar [8].

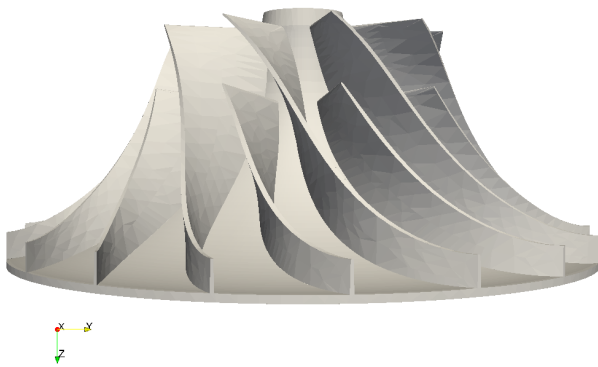
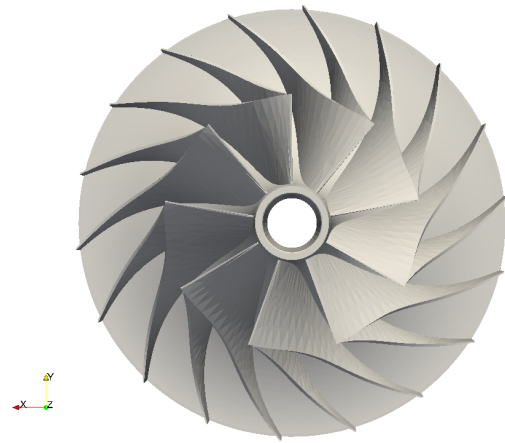
The impeller has nine full and nine splitter backswept blades, with the outer diameter equal to 271 mm. Since the design speed is 27,660 rpm, this compressor is categorised as high-speed centrifugal.

Vanless diffusers are applied in compressors with moderate rotor work. The outlet velocity of the rotor may be supersonic and the vaneless space is intended to mix the jet and wake flows and decrease the Mach number. Design parameters of the compressor which includes design operating performance are listed in Table 4.3.1.

Table 4.3.1: Compressor design parameters.

Mass flow [kg/s]	1.8
Rotational speed [rpm]	27,660
Rotor outlet radius [mm]	135.5
Diffuser outlet radius [mm]	271
Blade backsweep at rotor outlet	40°
Blade height at rotor exit [mm]	12.2
Diffuser height [mm]	10.3
Number of full and splitter blades	9 + 9

The computational model of the rotor on which the mesh was built is represented in the isometric projection, Fig. 4.3.3, while in Fig. 4.3.1 the projection looking from *YZ*-plane is shown. Projection looking from *XY*-plane is shown in Fig. 4.3.2. The axis of rotation is aligned with *z*-coordinate axis. Since the rotor is symmetrical, any blade passage may be modelled with cyclic boundary conditions.

**Figure 4.3.1:** YZ plane.**Figure 4.3.2:** XY plane.

The computational mesh includes one passage between two blades due to limited computer resources and time. Besides the volume inside the rotor blades, the mesh must include a small volume before the rotor inlet to establish a flow profile. Also the diffuser section must be taken into account and included in the mesh. In the case of the inlet and diffuser block, the process of creating the mesh is trivial, since there are no helical surfaces. The diffuser height was assumed the same as the blade height at the rotor exit. The computational domain is shown in Fig. 4.3.3, with a relative position to the entire geometry. Meshing was done using Pointwise software [25]. The mesh is body-fitted bloc-structured to ensure numerical accuracy and stability of the convergence. It consists of 7 196 211 cells, with 3 regions. The rotor region is coloured red, the inlet region is coloured blue and the diffuser region is coloured green in Fig. 4.3.3. Also, the regions are used for later stages of simulation setup in which MRF zones are defined.

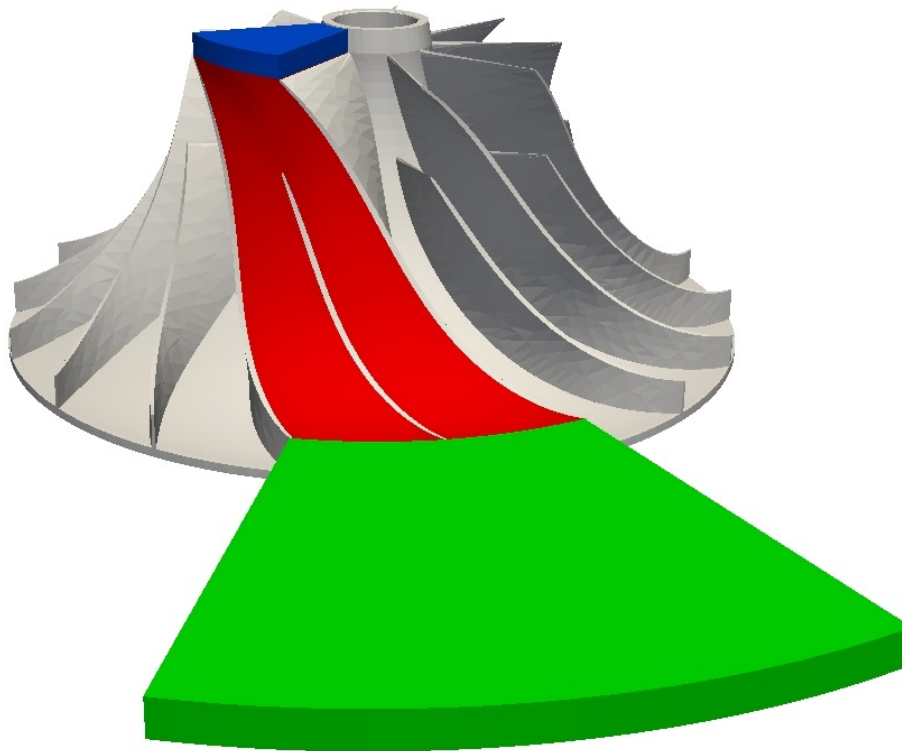


Figure 4.3.3: Regions of the domain.

4.3.1 Boundary Definition

In order to connect the mesh regions described in the previous section, OpenFoam utility `mergeMeshes` was used. The tool enables the connection of two different mesh regions into a single mesh. This approach was used to define GGI patches that serve as an interface. GGI patches were defined on faces which separate the zones of different reference frames. An overview of each mesh region is given next.

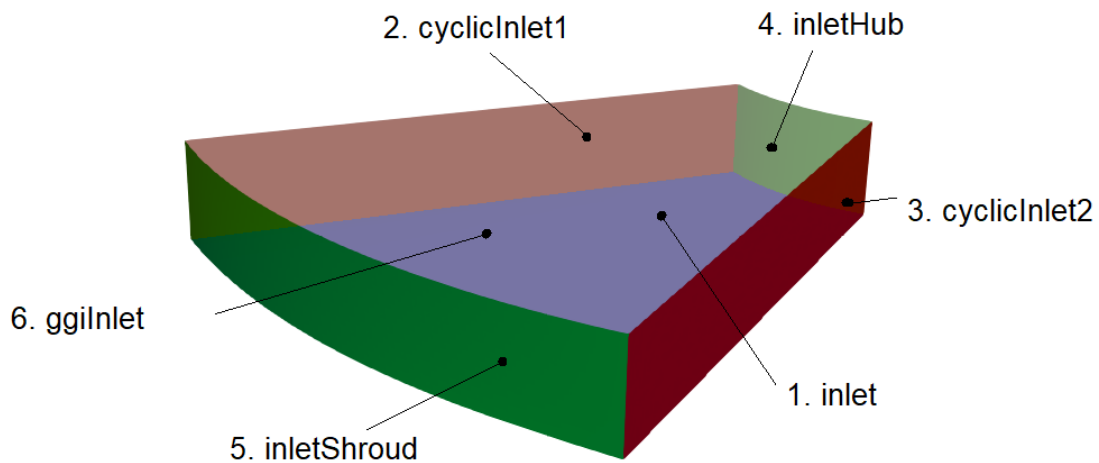
1. Inlet region

The Inlet region is the part of the mesh at the top of the domain, represented with blue in Fig. 4.3.3. It is the smallest region and all relevant information is given in Table 4.3.2.

Table 4.3.2: Inlet mesh region.

Inlet region	
Cell count	254,826
Cell type	hexahedra
Boundary patches	6
MRF	stationary zone

The names of the patches which make the inlet region are presented in Table 4.3.3. GGI master and shadow pairs and zones which are required to implement the GGI are presented in Table 4.3.8. As shown in Fig. 4.3.4, the inlet patch is on the top side coloured grey. A patch that is parallel with the *inlet* patch is *ggiInlet* and it is coloured blue. Vertical to the *inlet* and *ggiInlet* patches are *cyclicInlet1* and *cylinderInlet2* coloured red. On the front and back are patches *inletHub* and *inletShroud* which are modelled as a wall and coloured green.

**Figure 4.3.4:** Inlet region patches.

GGI boundary condition was introduced on the *ggiInlet* patch, in order to model the rothalpy jump could be modelled. This is the main reason for splitting the mesh in the three separate regions and then combining them into one continuous mesh. Code is set up in such a way that master and shadow *GGI* patches have to match each other in space,

eg. the two patches have to lie on the same plane. An example of bad alignment is shown in Fig. 4.3.5. This example is specifically emphasized because it caused a lot of trouble in making the case work. The red line represents the plane in which patch 6 from Table 4.3.3 and patch 1 from Table 4.3.5 intersect, although they have identical outer edges.

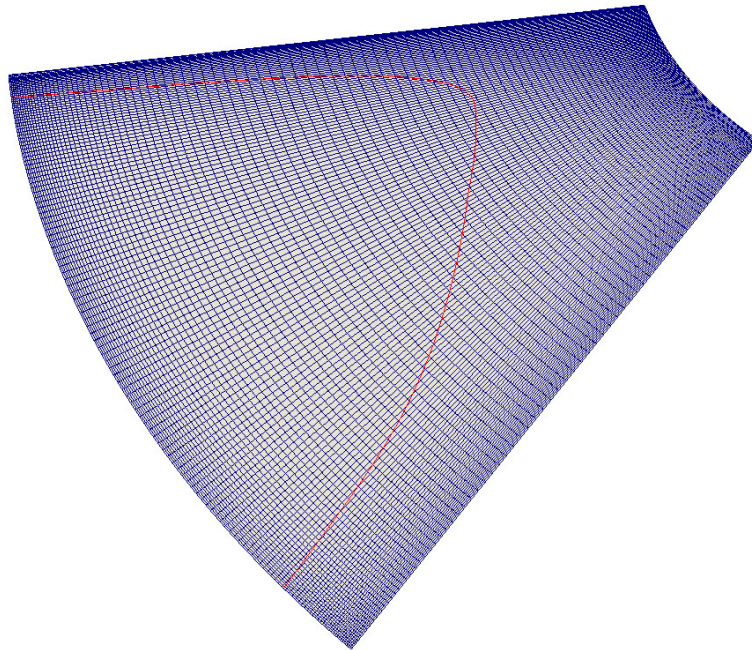


Figure 4.3.5: Inlet misalignment.

Table 4.3.3: Inlet region patches.

Number	Patch name	Patch type
1.	inlet	patch
2.	cyclicInlet1	cyclicGgi
3.	cyclicInlet2	cyclicGgi
4.	inletHub	wall
5.	inletShroud	wall
6.	ggiinlet	ggi

2. Rotor region

The Rotor region of the mesh is part in the centre of the domain and it is represented

with red colour in Fig. 4.3.3. This region was the most challenging to mesh, since is helically curved and demands extra caution go obtain a good geometry representation. The information about the rotor mesh region are given in Table 4.3.4, while

Table 4.3.4: Rotor mesh region.

Rotor region	
Cell count	5,465,196
Cell type	hexahedra
Boundary patches	7
MRF	rotational zone

The names and types of boundary conditions patches are presented in Table 4.3.5, and patches with GGI assigned conditions are explained in Table 4.3.8. A patch that serves as an inlet in this region is *ggiInletRotor*, it is located on the top of the region and it is coloured grey. Two patches which are not visible in Fig. 4.3.7 very small are *cyclicRotor1* and *cyclicRotor2*. The reason for the existence of these two very small patches is the better definition of the MRF zones. These two patches have a height of just one cell and span across the whole upper edge of the blade.

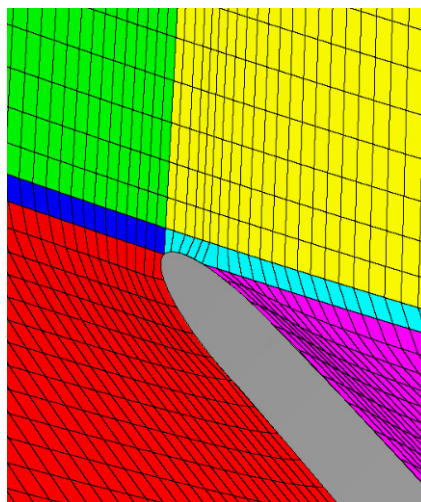


Figure 4.3.6: Rotor region.

Looking at Fig. 4.3.6, MRF zone extends outside the purple region. In the case of a boundary at the purple region, the tip of that blade would be modelled as stationary

which is unacceptable. To overcome this, a block with a height of just one cell is created, coloured cyan and blue. The yellow block belongs to the inlet region. Continuing further in Fig. 4.3.7, *rotorHub* and *rotorShroud* are defined as a wall. They represent the front and backside of the rotor. Patch *rotorBlades* is also defined as the wall because there is no flux through the blades. Finally, there is a *ggiOutletRotor* which represents the outlet part of the rotor region of the mesh and also serves as a boundary in the MRF model.

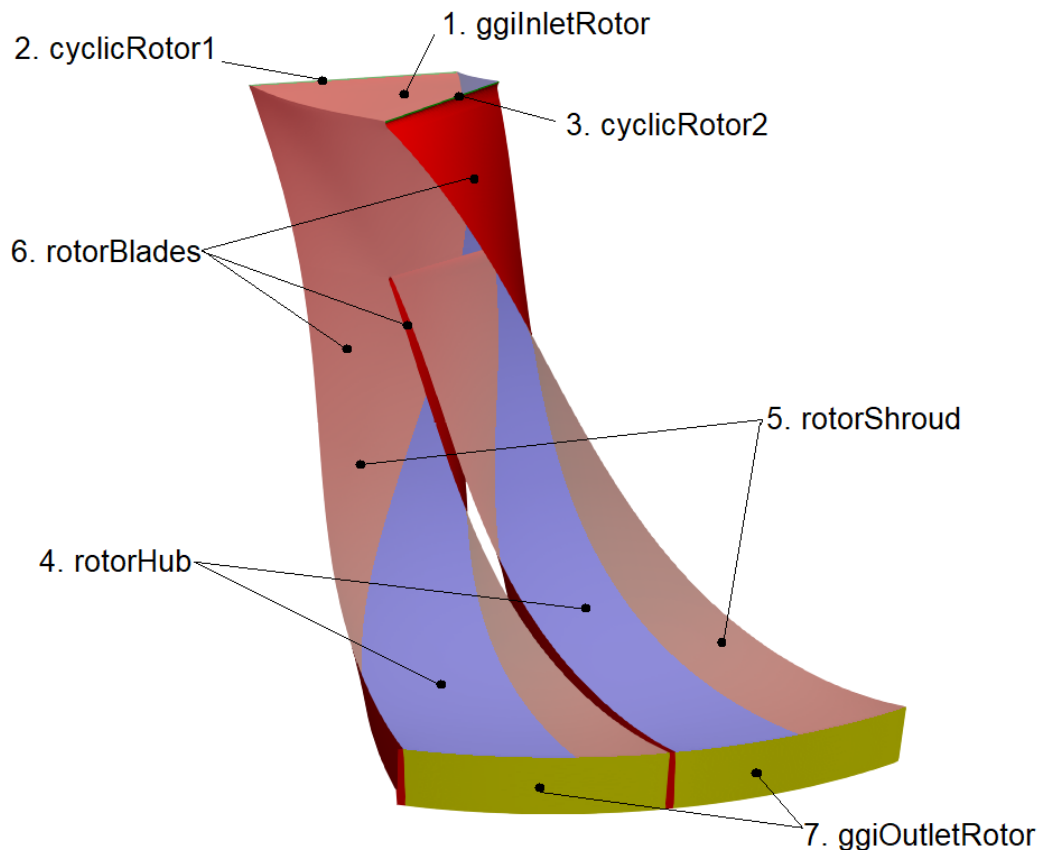


Figure 4.3.7: Rotor region patches.

At first, the simulation did not work and it was established that the same problem as before was present: Patches *ggiOutletRotor* and *ggiInletStator* did not match perfectly in space. Although the solution is known from the previous case, it couldn't have been implemented in this case. As shown in Fig. 4.3.5, the patches need to be in the same plane, however it is not a flat plane, since now patches overlap at the cylinder wall. This was caused by the imperfect representation of a cylindrical segment due to discretisation. The domain would need to have an infinite number of cells to match perfectly. To overcome

the problem, the code was modified to accept GGI patches which don't match perfectly.

Table 4.3.5: Rotor region patches.

Number	Patch name	Type
1.	ggiInletRotor	ggi
2.	cyclicRotor1	cyclicGgi
3.	cyclicRotor2	cyclicGgi
4.	rotorHub	wall
5.	rotorShroud	wall
6.	rotorBlades	wall
7.	ggiOutletRotor	ggi

3. Diffuser region

The diffuser region is the last one in Fig. 4.3.3, coloured green. This region represents the geometry of the vanless diffuser which in this case takes the shape of a disk segment. Table 4.3.6 contains information for the region. The outer edge of the region, defined as the *outlet* patch is located at the diffuser outlet radius according to the corresponding dimension from Table 4.3.1.

Table 4.3.6: Diffuser mesh region.

Diffuser region	
Cell count	1,489,752
Cell type	hexahedra
Boundary patches	6
MRF	stationary

The inlet to the region is on the patch *ggiInletRegion* and it is red. On the right and left side there are patches *cyclicStator1* and *cyclicStator2* which are *cyclicGgi*, with the assigned angle of rotation of 40° and coloured blue. Patch *statorShroud* is on the top, and it is identical to the patch *statorHub* which is at the bottom and green. Both have

wall boundary condition assigned. The last patch is the *outlet*, coloured red in Fig. 4.3.8. All patches and their types are presented in Table 4.3.7.

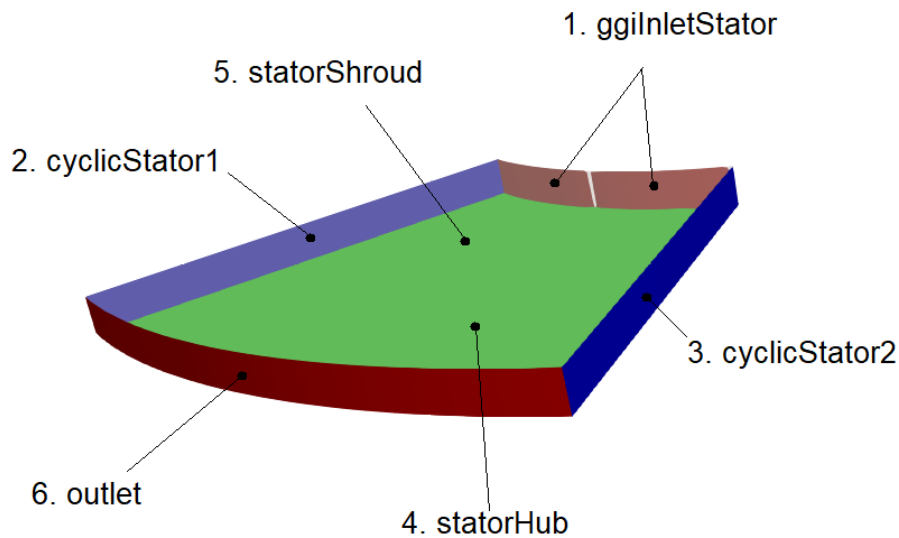


Figure 4.3.8: Diffuser region patches.

Table 4.3.7: Diffuser region patches

Number	Patch name	Type
1.	ggiInletStator	ggi
2.	cyclicStator1	cyclicGgi
3.	cyclicStator2	cyclicGgi
4.	statorHub	wall
5.	statorShroud	wall
6.	outlet	patch

All boundary definitions were described in this section, while in the following section an overview of boundary conditions assigned on these patches with corresponding values, will be given.

Table 4.3.8: GGI pairs and corresponding zones.

Number	Patch name	Interface type	Patch pair	Zone
1.	cyclicInlet1	cyclicGgi	cyclicInlet2	cyclicInlet1Zone
2.	cyclicInlet2	cyclicGgi	cyclicInlet1	cyclicInlet2Zone
3.	ggiInlet	ggi	ggiInletRotor	ggiInletRotorZone
4.	ggiInletRotor	ggi	ggiInlet	ggiInletZone
5.	cyclicRotor1	cyclicGgi	cyclicRotor2	cyclicRotor1Zone
6.	cyclicRotor2	cyclicGgi	cyclicRotor1	cyclicRotor2Zone
7.	ggiOutletRotor	ggi	ggiInletStator	ggiOutletRotorZone
8.	ggiInletStator	ggi	ggiOutletRotor	ggiInletStatorZone
9.	cyclicStator1	cyclicGgi	cyclicStator2	cyclicStator1Zone
10.	cyclicStator2	cyclicGgi	cyclicStator1	cyclicStator2Zone

4.3.2 Boundary Conditions

Boundary conditions must be applied to all patches of the computational domain to define the conditions that make the system of equations solvable. There are three tables with boundary conditions for the three regions of the mesh. Tab. 4.3.9, Tab. 4.3.10 and Tab. 4.3.11 present boundary conditions for the inlet, rotor and diffuser part of the mesh. Descriptions of the boundary conditions used in tables can be found in Appendix A.4.

Table 4.3.9: Boundary conditions for inlet region.

Boundary conditions									
Number	Patch name	alphan [kg/ms]	i [m ² /s ²]	k [m ² /s ²]	mut [kg/ms]	omega [1/s]	p [kg/ms ²]	T [K]	U [m/s]
1.	inlet	zeroGradient;	fixedValue; uniform 302100;	turbulentIntensityKineticEnergyInlet; intensity 0.05; uniform 0.375;	zeroGradient;	compressible::turbulentMixingLenghtFrequencyInlet; mixingLenght 0.01; uniform 7400;	isentropicTotalPressure; gamma 1.4; p0 uniform 96000; uniform 96000;	isentropicTotalTemperature; gamma 1.4; T0 uniform 300; uniform 300;	pressureInletOutletVelocity; uniform (0 0 1);
2.	cyclicInlet1	cyclicGgi; uniform 0;	cyclicGgi; uniform 302100;	cyclicGgi; uniform 0.375;	cyclicGgi; uniform 1e-5;	cyclicGgi; uniform 7400;	cyclicGgi; uniform 96000;	cyclicGgi; uniform 300;	cyclicGgi; uniform (0 0 0);
3.	cyclicInlet2	cyclicGgi; uniform 0;	cyclicGgi; uniform 302100;	cyclicGgi; uniform 0.375;	cyclicGgi; uniform 1e-5;	cyclicGgi; uniform 7400;	cyclicGgi; uniform 96000;	cyclicGgi; uniform 300;	cyclicGgi; uniform (0 0 0);
4.	inletHub	alphanWallFunction;	gradientEnthalpy; uniform 302100;	compressible::kqRWallFunction;	mutWallFunction;	compressible::omegaWallFunction;	zeroGradient;	zeroGradient;	fixedValue; uniform (0 0 0);
5.	inletShroud	alphanWallFunction	gradientEnthalpy; uniform 302100;	compressible::kqRWallFunction;	mutWallFunction;	compressible::omegaWallFunction;	zeroGradient;	zeroGradient;	fixedValue; uniform (0 0 0);
6.	ggiInlet	ggi; uniform 0;	ggiEnthalpyJump; patchType ggi; rotating false; uniform 302100;	ggi; uniform 0.375;	ggi; uniform 1e-5;	ggi; uniform 7400;	ggi; uniform 96000;	ggi; uniform 300;	ggi; uniform (0 0 0);

Table 4.3.10: Boundary conditions for rotor region.

Number	Patch name	Boundary conditions							
		alphanut [kg/ms]	i [m ² /s ²]	k [m ² /s ²]	mut [kg/ms]	omega [1/s]	p [kg/ms ²]	T [K]	U [m/s]
1.	ggiInletRotor	ggi; uniform 0;	ggiEnthalpyJump; patchType ggi; rotating true; uniform 302100;	ggi; uniform 0.375;	ggi; uniform 1e-5;	ggi; uniform 7400;	ggi; uniform 96000;	ggi; uniform 300;	ggi; uniform (0 0 0);
2.	cyclicRotor1	cyclicGgi; uniform 0;	cyclicGgi; uniform 302100;	cyclicGgi; uniform 0.375;	cyclicGgi; uniform 1e-5;	cyclicGgi; uniform 7400;	cyclicGgi; uniform 96000;	cyclicGgi; uniform 300;	cyclicGgi; uniform (0 0 0);
3.	cyclicRotor2	cyclicGgi; uniform 0;	cyclicGgi; uniform 302100;	cyclicGgi; uniform 0.375;	cyclicGgi; uniform 1e-5;	cyclicGgi; uniform 7400;	cyclicGgi; uniform 96000;	cyclicGgi; uniform 300;	cyclicGgi; uniform (0 0 0);
4.	rotorBlades	alphanutWallFunction;	gradientEnthalpy; gradient uniform 0; uniform 302100;	compressible::kqRWallFunction;	mutWallFunction;	compressible::omegaWallFunction;	zeroGradient;	zeroGradient;	fixedValue; uniform (0 0 0);
5.	rotorHub	alphanutWallFunction;	gradientEnthalpy; gradient uniform 0; uniform 302100;	compressible::kqRWallFunction;	mutWallFunction;	compressible::omegaWallFunction;	zeroGradient;	zeroGradient;	fixedValue; uniform (0 0 0);
6.	rotorShroud	alphanutWallFunction;	gradientEnthalpy; gradient uniform 0; uniform 302100;	compressible::kqRWallFunction;	mutWallFunction;	compressible::omegaWallFunction;	zeroGradient;	zeroGradient;	fixedValue; uniform (0 0 0);
7.	ggiOutletRotor	ggi; uniform 0;	ggiEnthalpyJump; patchType ggi; rotating true; uniform 302100;	ggi; uniform 0.375;	ggi; uniform 1e-5;	ggi; uniform 7400;	ggi; uniform 96000;	ggi; uniform 300;	ggi; uniform (0 0 0);

Table 4.3.11: Boundary conditions for diffuser region.

Boundary conditions									
Number	Patch name	alphanat [kg/ms]	i [m ² /s ²]	k [m ² /s ²]	mut [kg/ms]	omega [1/s]	p [kg/ms ²]	T [K]	U [m/s]
1.	ggiInletStator	ggi; uniform 0;	ggiEnthalpyJump; patchType ggi; rotating false; uniform 302100;	ggi; uniform 0.375;	ggi; uniform 1e-5;	ggi; uniform 7400;	ggi; uniform 96000;	ggi; uniform 300;	ggi; uniform (0 0 0);
2.	cyclicStator1	cyclicGgi; uniform 0;	cyclicGgi; uniform 302100;	cyclicGgi; uniform 0.375;	cyclicGgi; uniform 1e-5;	cyclicGgi; uniform 7400;	cyclicGgi; uniform 96000;	cyclicGgi; uniform 300;	cyclicGgi; uniform (0 0 0);
3.	cyclicStator2	cyclicGgi; uniform 0;	cyclicGgi; uniform 302100;	cyclicGgi; uniform 0.375;	cyclicGgi; uniform 1e-5;	cyclicGgi; uniform 7400;	cyclicGgi; uniform 96000;	cyclicGgi; uniform 300;	cyclicGgi; uniform (0 0 0);
4.	statorHub	alphanatWallFunction;	gradientEnthalpy; gradient uniform 0; uniform 302100;	compressible::kqRWallFunction	mutWallFunction;	compressible::omegaWallFunction;	zeroGradient;	zeroGradient;	fixedValue; uniform (0 0 0);
5.	statorShroud	alphanatWallFunction;	gradientEnthalpy; gradient uniform 0; uniform 302100;	compressible::kqRWallFunction;	mutWallFunction,	compressible::omegaWallFunction;	zeroGradient;	zeroGradient;	fixedValue; uniform (0 0 0);
6.	outlet	zeroGradient;	inletOutlet; inletValue uniform 302100; uniform 302100;	inletOutlet; inletValue uniform 0.375; uniform 0.375;	zeroGradient;	inletOutlet; inletValue uniform 7400; uniform 7400;	isentropicTotalPressure; gamma 1.4; p0 uniform 96000; uniform 96000;	isentropicTotalTemperature; gamma 1.4; T0 uniform 300; uniform 300;	pressureInletOutletVelocity; uniform (0 1 0);

4.4 Simulation Setup

Looking at the *inlet* patch in Table 4.3.9 and the *outlet* patch in Table 4.3.11, reveals that velocity \mathbf{U} and temperature \mathbf{T} have the same. These are the values set up at the beginning of the simulation procedure, since the values corresponding to final state would cause divergence. Thus, the values were changed gradually while the simulation was running to "gently" achieve the desired operating point. Also, outlet pressure was changed gradually, which allowed the propagation of fields through the domain. Along with the gradual change of pressure, the rotational speed of the MRF zone should be changed gradually, too. Also, the velocity field was initialised with the solution of the incompressible flow. If MRF rotation is prescribed in the first time step of the simulation, to be equal to nominal rotational speed, which is 27,660 rpm, the simulation would also fail. Due to currently insufficient mass flow. As described in Section 4.2, this type of compressor behaviour is choking. The rotational speed of MRF is set to gradually increase with increasing number of iterations. The details and examples of the gradual setup are given in Appendix A.4.

4.5 Closure

In this section the domain and setup and initial conditions were given, along with the description of the domain and simulation, a short description of centrifugal compressors. The problems encountered in the case set-up were described, for further reference. The results of simulation will be shown in the following chapter. Results will be grouped into two sections, results for operating conditions and off-design conditions. In part with operating conditions, results for three working conditions are presented. Off-design condition result is shown for choke condition.

Chapter 5

Results

5.1 Introduction

Compressor geometry, meshing strategy and the resulting mesh topology were presented in the previous chapter. The challenges which emerged in the simulation process were discussed as well. In this chapter, the results for three nominal compressor operating points will be presented, as well as the results for choke conditions.

5.2 Design operating conditions

In this section the results of the simulations for the design operating points will be presented. Three conditions were simulated, shown in Fig. 5.2.1 coloured with red dots. Table 5.2.1 contains the information about the simulated conditions and the results of the simulation are shown in table 5.2.2. The results are presented in the form of the mass flow rate in order to compared with experimental results data from [8]. Pressure forces on the rotor, their momentum, and the shaft power required by the rotor are presented in Table 5.2.3.

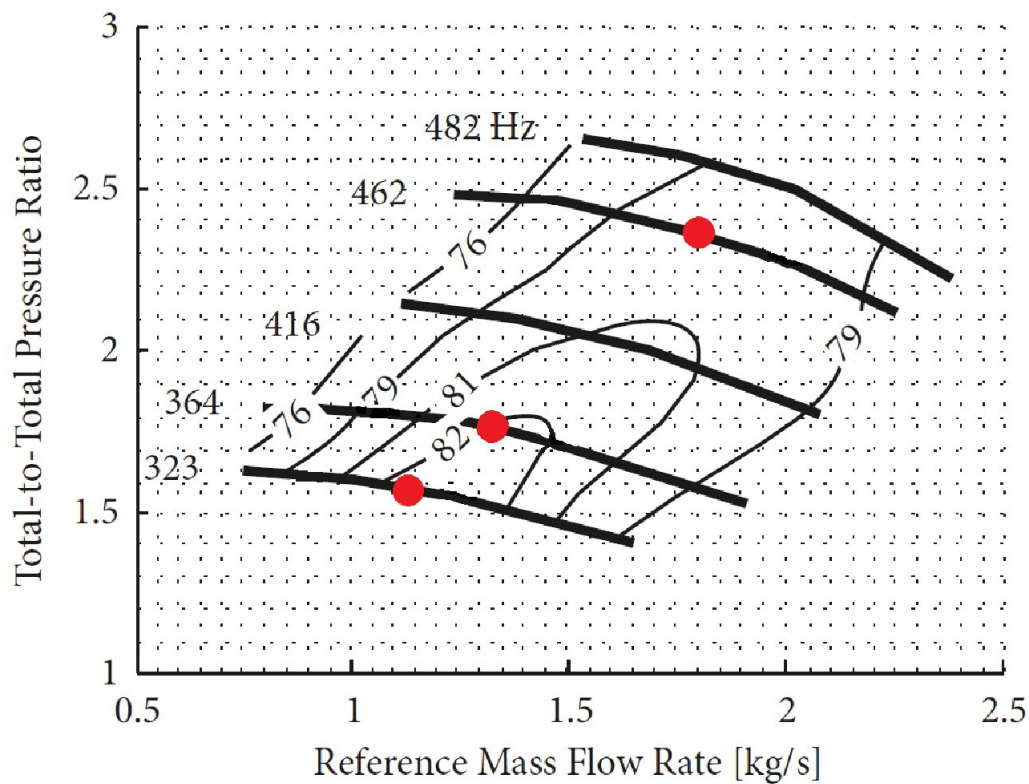


Figure 5.2.1: Simulated conditions.

Table 5.2.1: Operating points specifications.

Point	Rotational speed [1/s]	Mass flow rate [kg/s]	Pressure ratio r
1	462	1.80	2.36
2	364	1.33	1.72
3	323	1.13	1.57

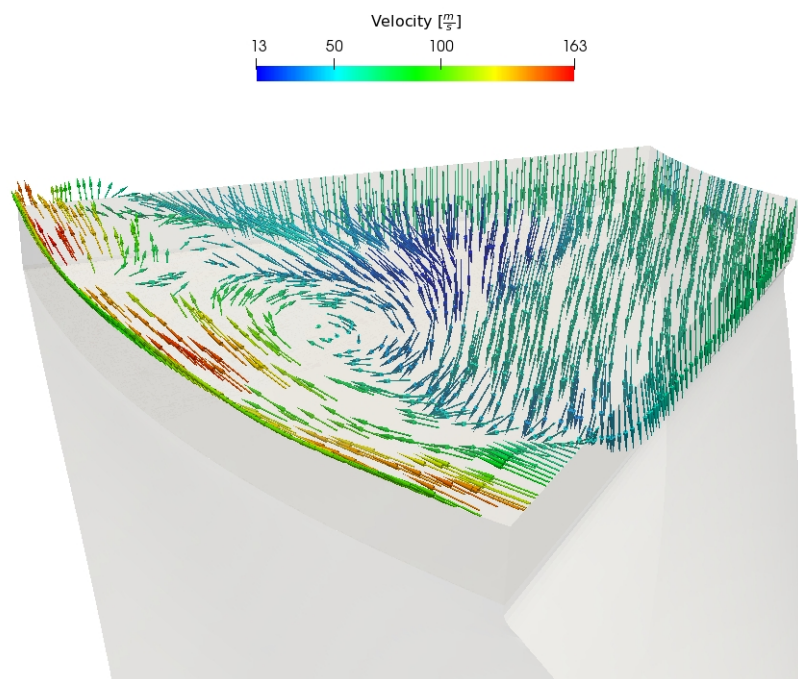
Table 5.2.2: Mass flow rate results.

Point	Desired mass flow rate [kg/s]	Achieved mass flow rate [kg/s]	Relative difference
1	1.80	1.627	-10.09%
2	1.33	1.243	-6.79%
3	1.13	1.092	-3.40%

Table 5.2.3: Rotor forces, moments and power.

Point	Rotor force [N]	Rotor moment [Nm]	Power [kW]
1	955.06	137.87	399.35
2	543.63	77.86	178.08
3	407.25	58.38	118.49

Fig. 5.2.2 represents the direction of absolute velocity vectors at the inlet patch. The swirl pattern of velocity is caused by the very high rotational speed of the rotor, thus creating a suction effect. Figs. 5.2.2-5.2.26 correspond to operating point 3, Table 5.2.2.

**Figure 5.2.2:** Velocity vectors at the inlet.

The direction of velocity in the diffuser part and at the outlet patch of the domain are shown in Fig. 5.2.3. Since the vector direction is not radial, there is a loss of energy used for the creation of vortices. This kind of flow is the main drawback of vaneless diffuser compressors. To harvest additional amount of energy, diffuser blades are usually installed. They change the direction of the flow and slow it down to convert the kinetic energy into pressure increase.

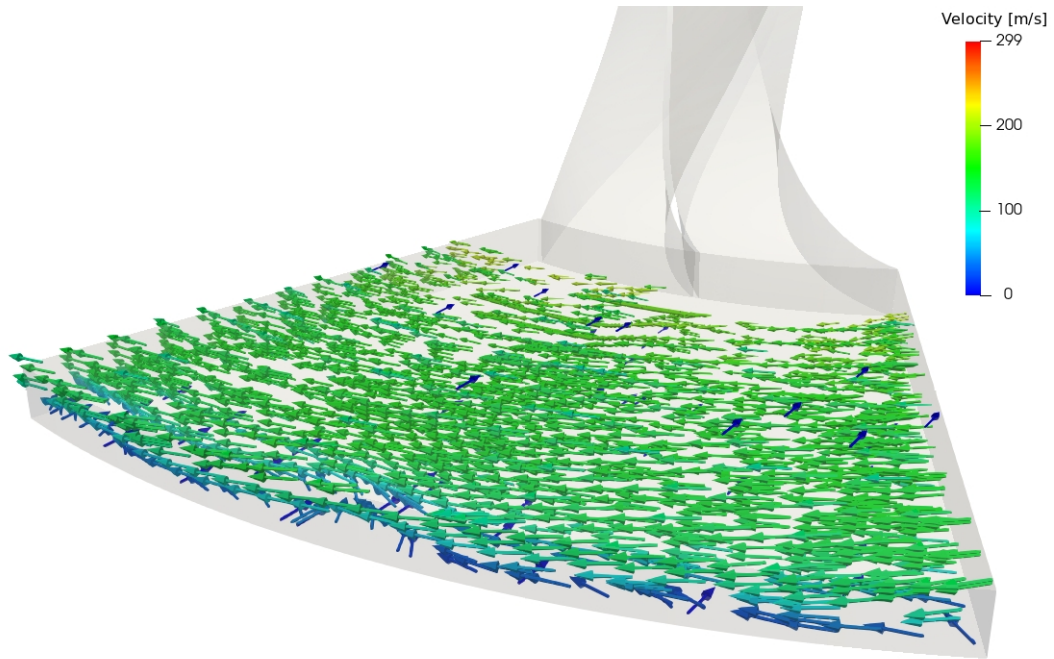


Figure 5.2.3: Velocity vectors in diffuser.

The following figures present the pressure field (Fig. 5.2.4), temperature field (Fig. 5.2.5), turbulent kinetic energy (Fig 5.2.6) and rothalpy field (Fig. 5.2.7).

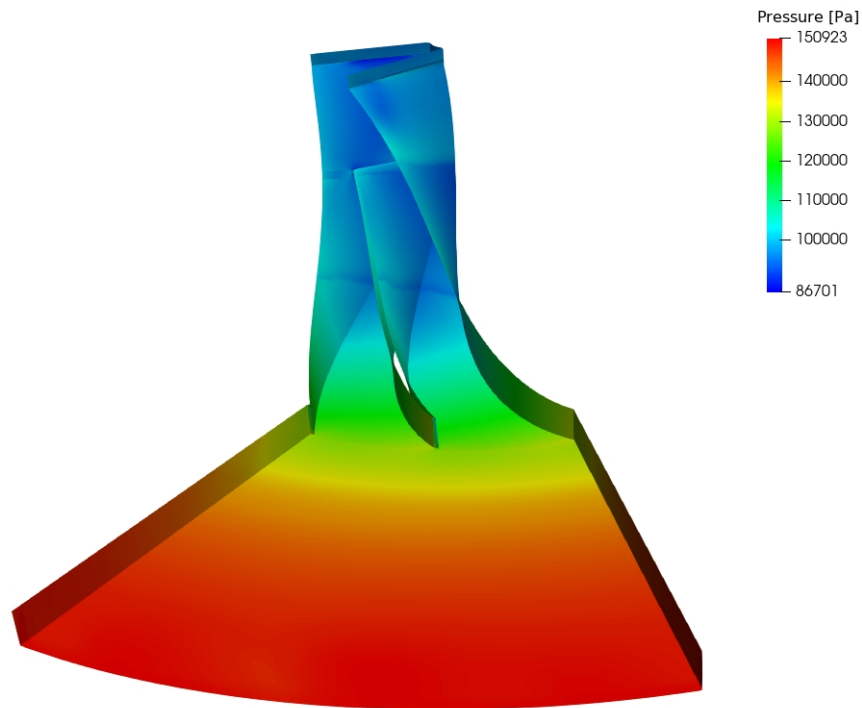


Figure 5.2.4: Pressure field.

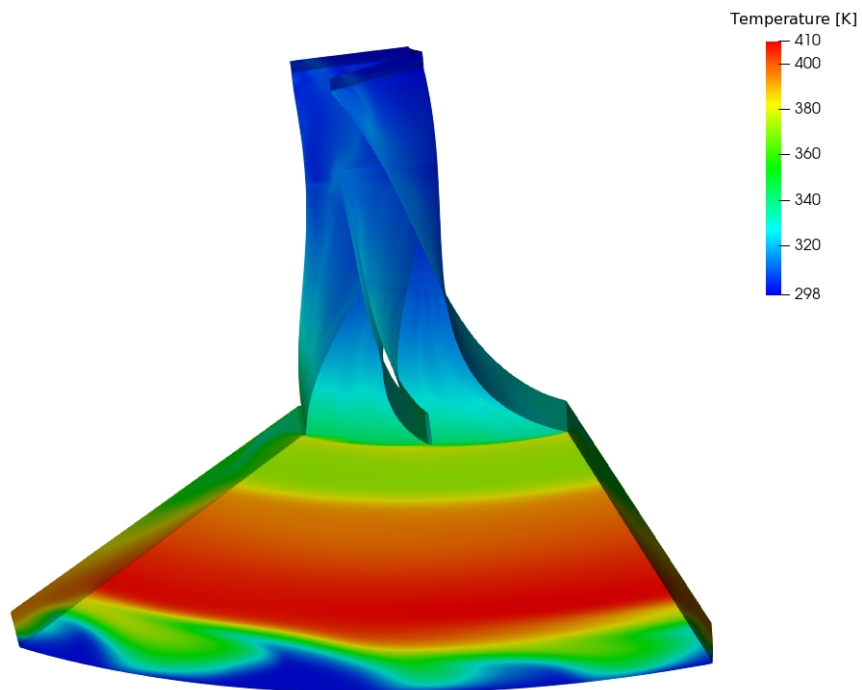


Figure 5.2.5: Temperature field.

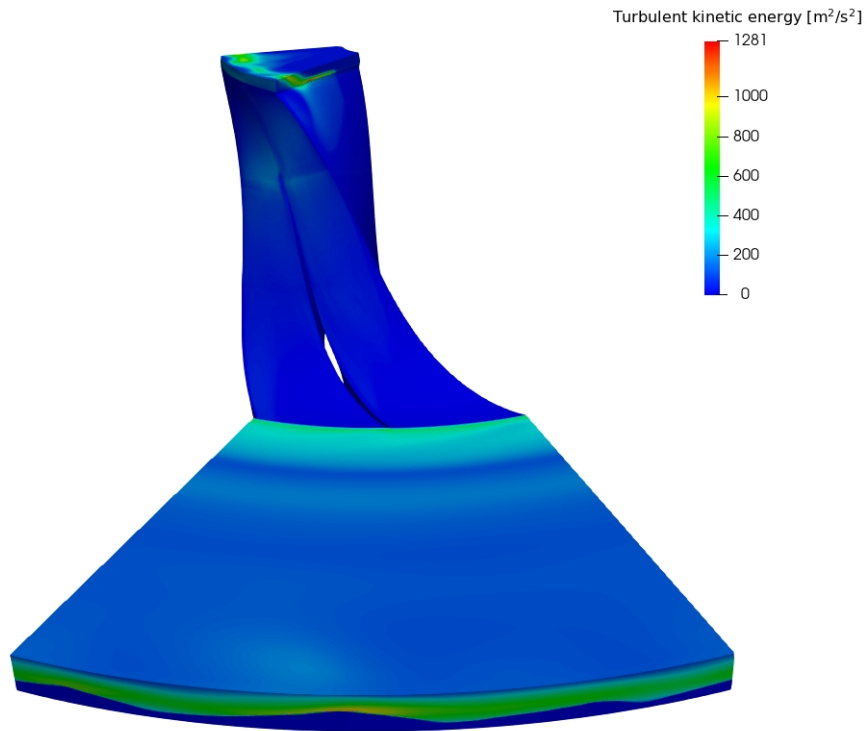


Figure 5.2.6: Turbulent kinetic energy field.

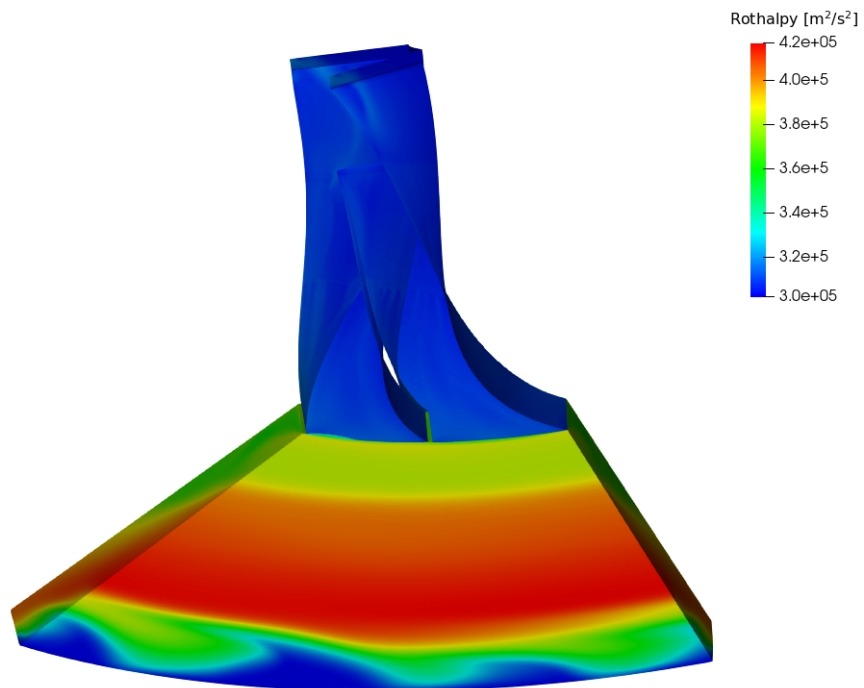


Figure 5.2.7: Rothalpy field.

Eqn. (4.2.8) written in the relative frame is expressed using the rothalpy I :

$$I = h_{0r} - \frac{1}{2} \mathbf{U}_{rot}^2, \quad (5.2.1)$$

where the term rothalpy comes from rotating total enthalpy [5], and it is commonly used in turbomachinery. Because of the second term in Eqn (5.2.1), $\frac{1}{2} \mathbf{U}_{rot}^2$, a sudden jump in value is visible between the rotor and the stator since the rotational speed \mathbf{U}_{rot} term vanishes in the stator.

In the following figures the results will be shown from a different perspective. The diffuser part of the mesh is cut half-height to better represent the flow inside. Fig. 5.2.8 represents the absolute velocity field, Fig. 5.2.9 shows the relative velocity field, Fig. 5.2.10 shows the pressure field, Fig. 5.2.11 shows the temperature field, Fig. 5.2.12 shows the rothalpy field, Fig. 5.2.13 shows the turbulent kinetic energy field and Mach number is shown in Fig. 5.2.14. Comparing Fig 5.2.11 and Fig. 5.2.12, reveals that result for the temperature field is calculated using enthalpy.

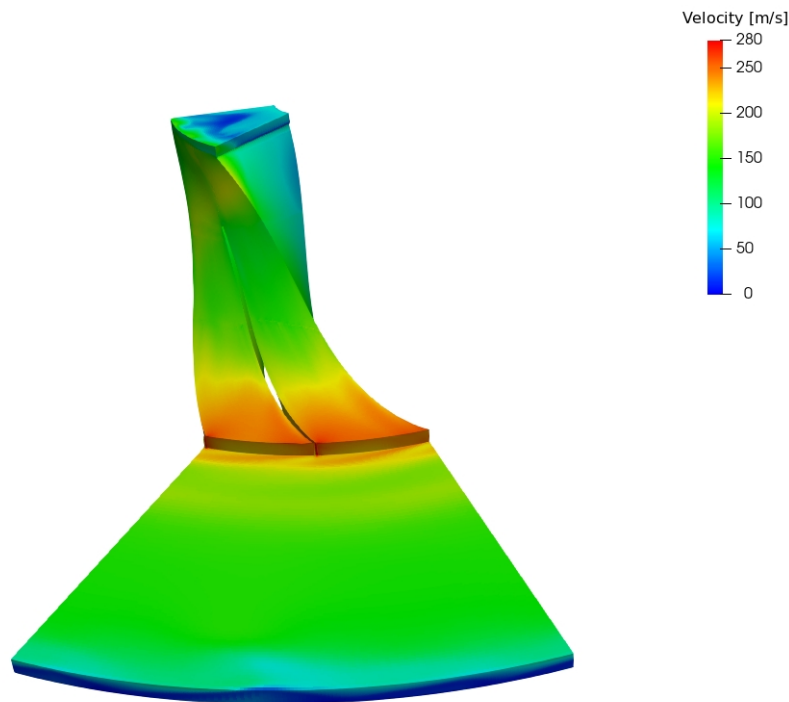


Figure 5.2.8: Velocity field view with a slice of the diffuser part.

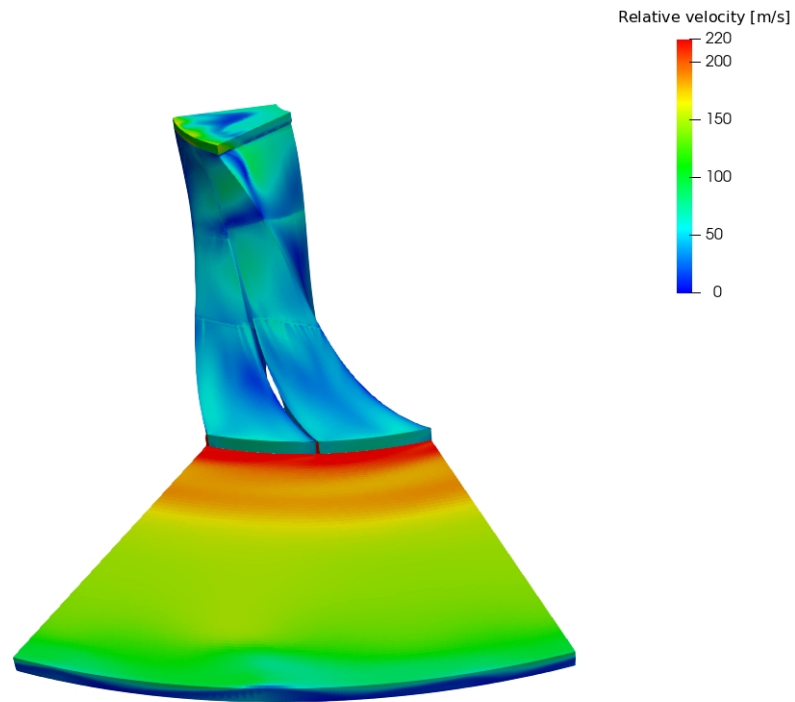


Figure 5.2.9: Relative velocity field view with a slice of the diffuser part.

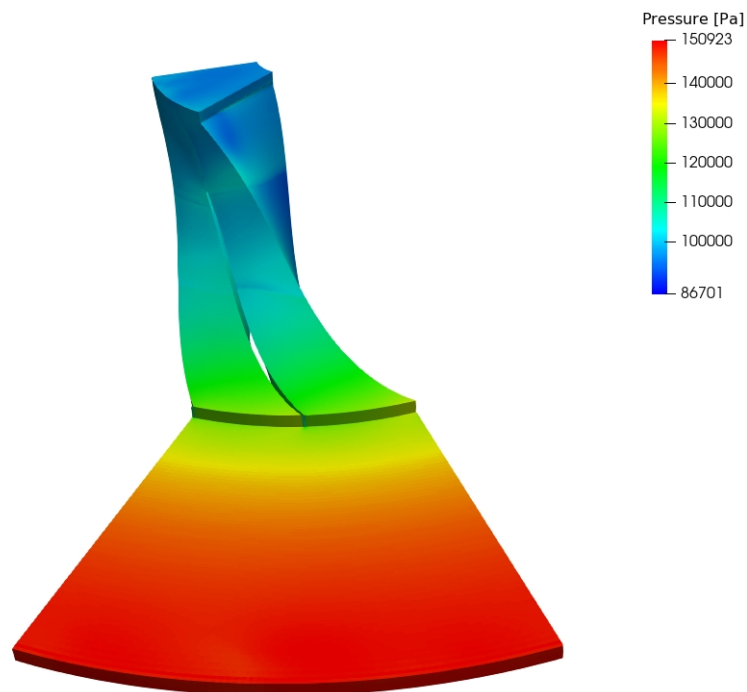


Figure 5.2.10: Pressure field view with a slice of the diffuser part.

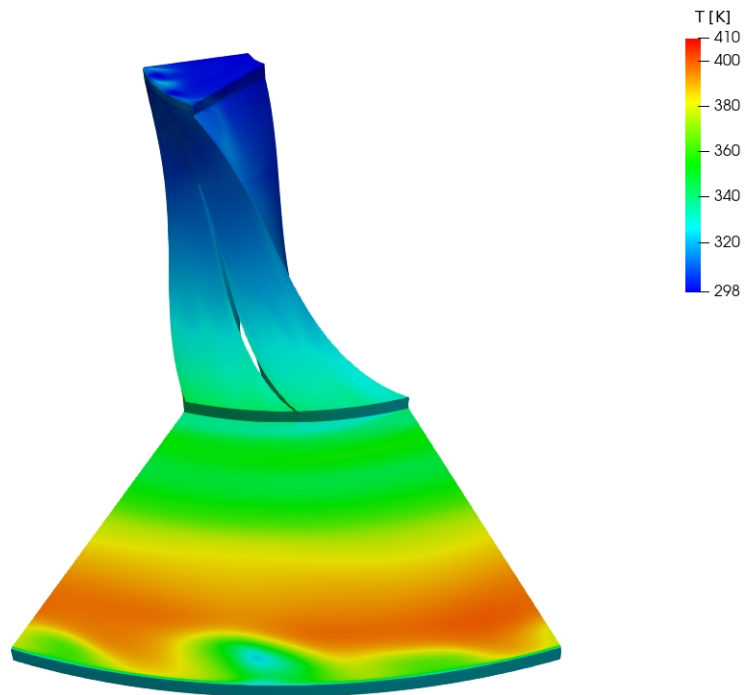


Figure 5.2.11: Temperature field view with a slice of the diffuser part.

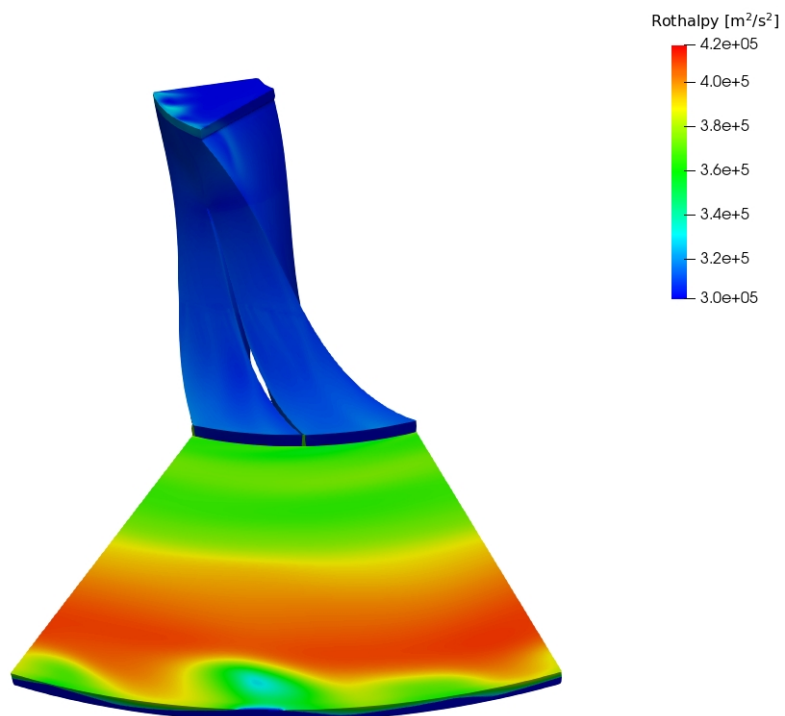


Figure 5.2.12: Rothalpy field view with a slice of the diffuser part.

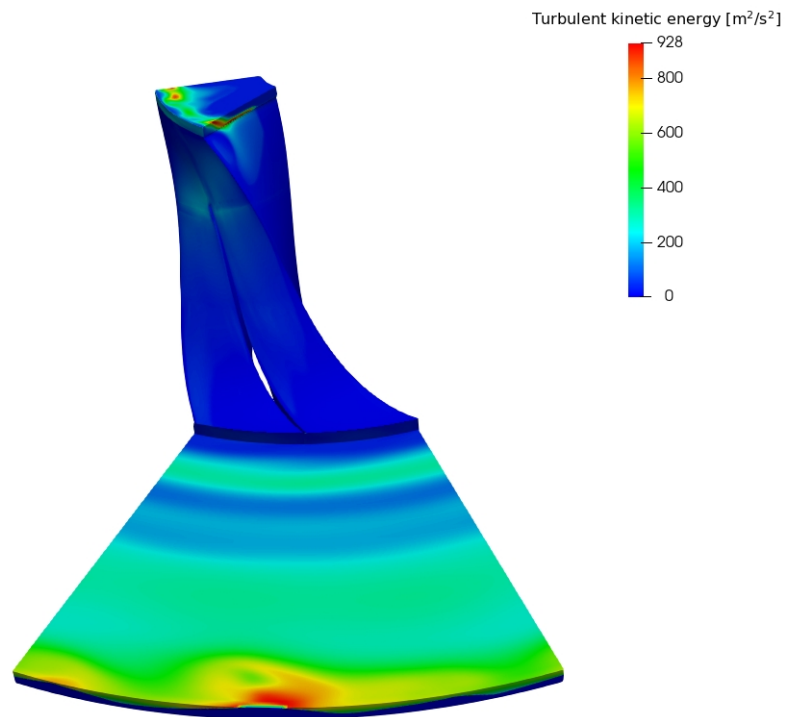


Figure 5.2.13: Turbulent kinetic energy field view with a slice of the diffuser part.

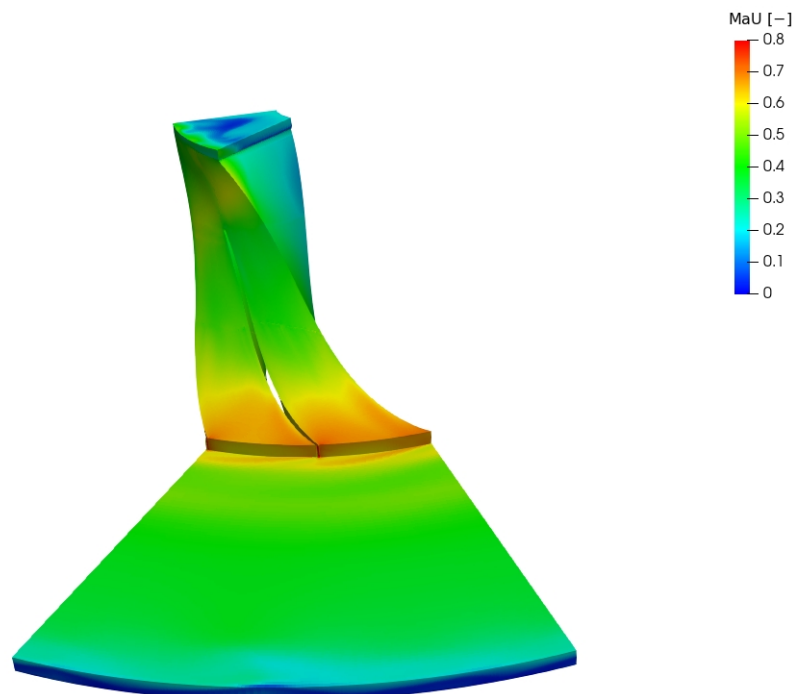


Figure 5.2.14: Mach number field view with a slice of the diffuser part.

In Fig. 5.2.10, the discontinuity in the rotor part of the mesh is visible and they are the so-called *lambda shock*, Fig. 5.2.17. In the operating point map, there should not be shocks with nominal conditions, however this kind of shock does not cover the whole section of the rotor canal. Thus, it allows propagation of information through the canal on the front side which is not affected by the shock. This phenomenon is causing local losses in enthalpy due to the highly irreversible process of the shock wave. The case in which the shock wave covers the whole canal is described in Section 5.3.1.

Flow inside the canal of the impeller is very complex, and 3-dimensional. In the case of a stationary rotor (rotational speed is 0 rpm) flow would resemble the flow in a square channel, the velocities would be lowest near the walls and longest further away from the wall (in the middle of the channel). In the case of rotational elements with extreme rotational velocities, the flow behaves differently. Centrifugal force is now greater than the force caused by the pressure difference which is the main driving force in the stationary case. Due to greater value, centrifugal force is now dominant and it is accelerating the fluid on the pressure side of the rotor blade. On the suction side, there is the opposite effect, the blade is sucking the flow behind the moving blade in. The consequence of this is that the lower flow rates are present in the middle of the section, shown in Fig. 5.2.15. Fig. 5.2.16 shows the direction of relative velocities vectors, and vortices in the direction opposite of the flow can be observed. This behaviour can be described with the previously stated dominant centrifugal force which is forcing the fluid to accelerate near the pressure and suction side of the blade which results in creating the velocity deficit in the center portion of the channel. The differences in velocities can be so large that they cause backflow.

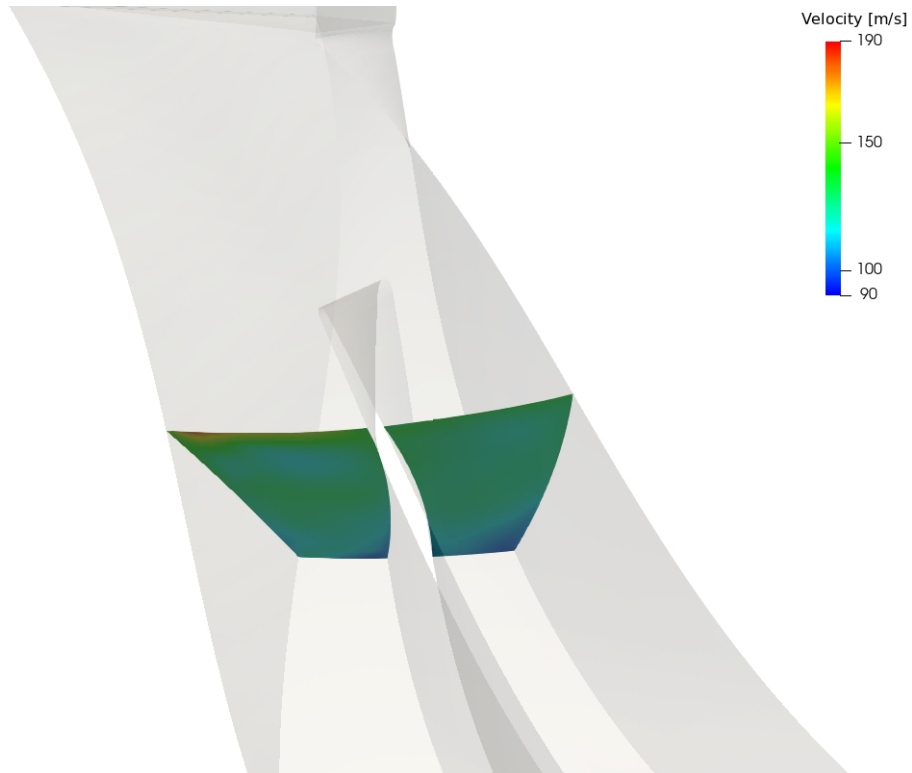


Figure 5.2.15: Rotor slice velocities.

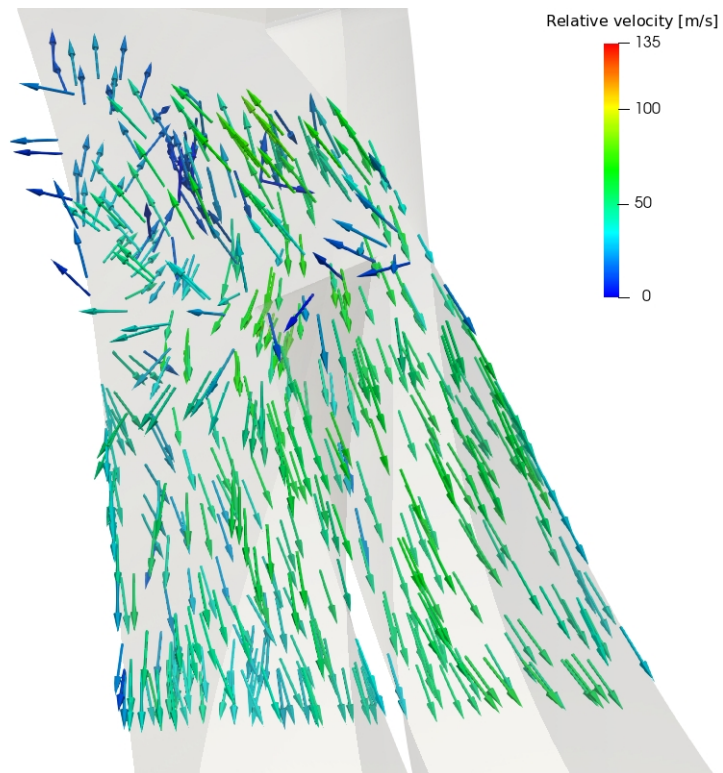


Figure 5.2.16: Rotor velocities vectors.

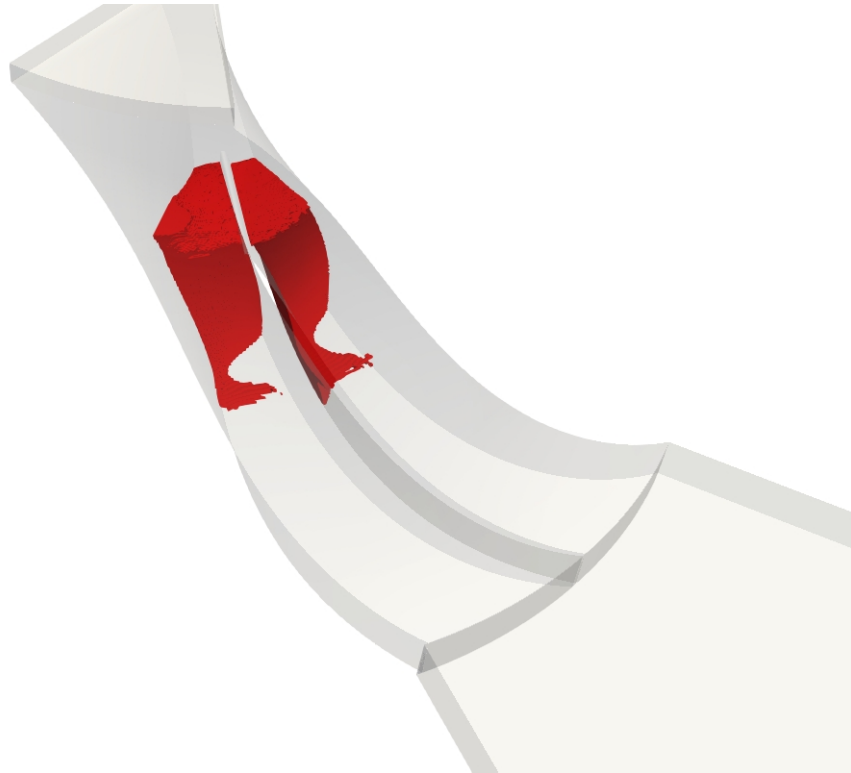


Figure 5.2.17: Lambda shock.

The view is in meridional slices useful to observe the changes through the compressor. Fig. 5.2.18 represents the velocity field at the meridional plane, Fig. 5.2.19 represents the pressure field at the meridional plane, Fig. 5.2.20 represents the temperature field at the meridional plane, Fig. 5.2.21 represents the density distribution on the plane, Fig. 5.2.22 represents the rothaply distribution on the plane and Fig. 5.2.23 shows the turbulent kinetic energy.

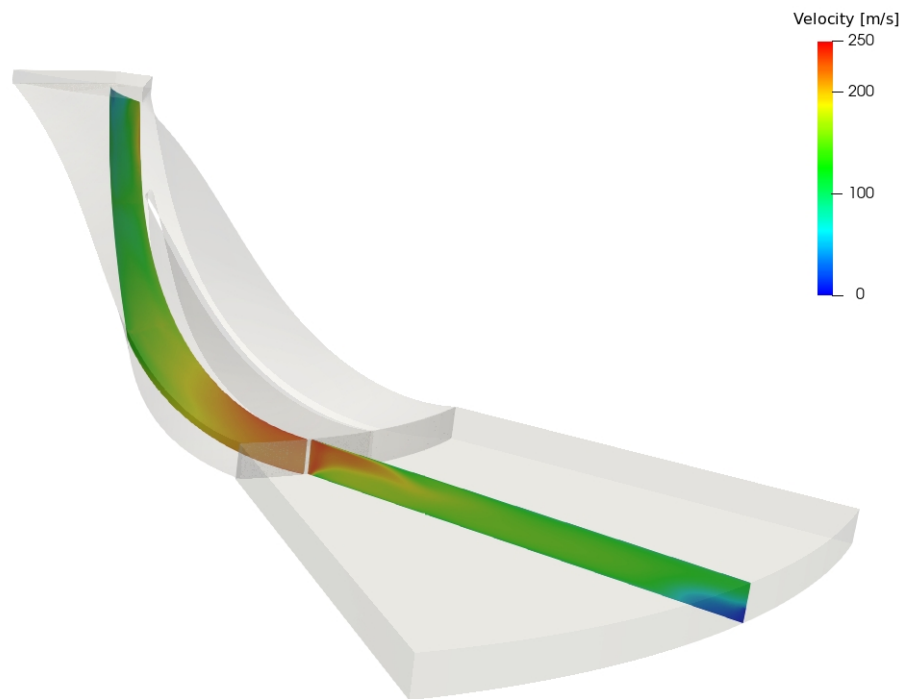


Figure 5.2.18: Velocity field view at meridional plane.

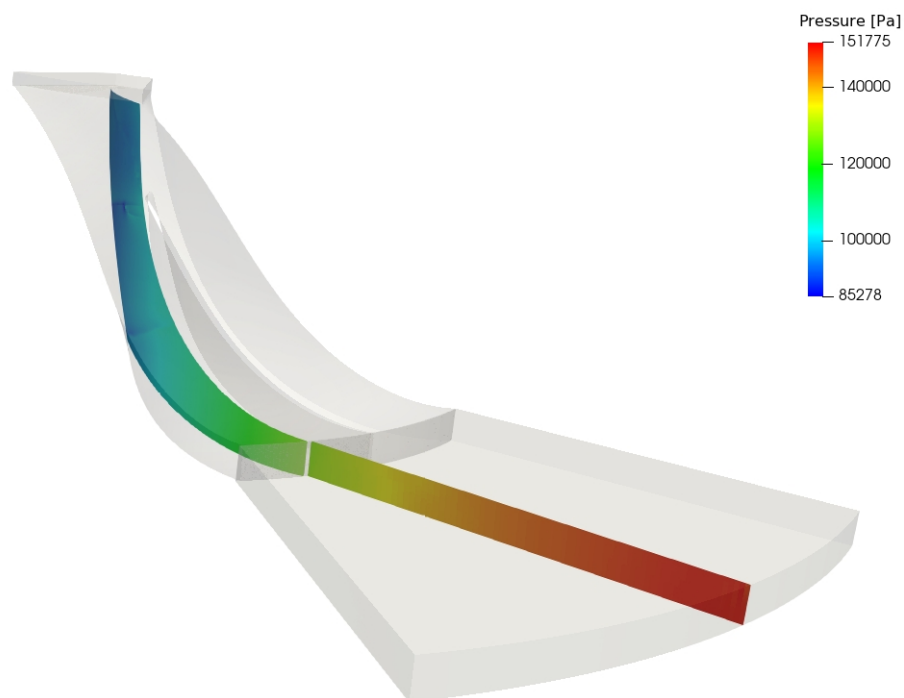


Figure 5.2.19: Pressure field view at meridional plane.

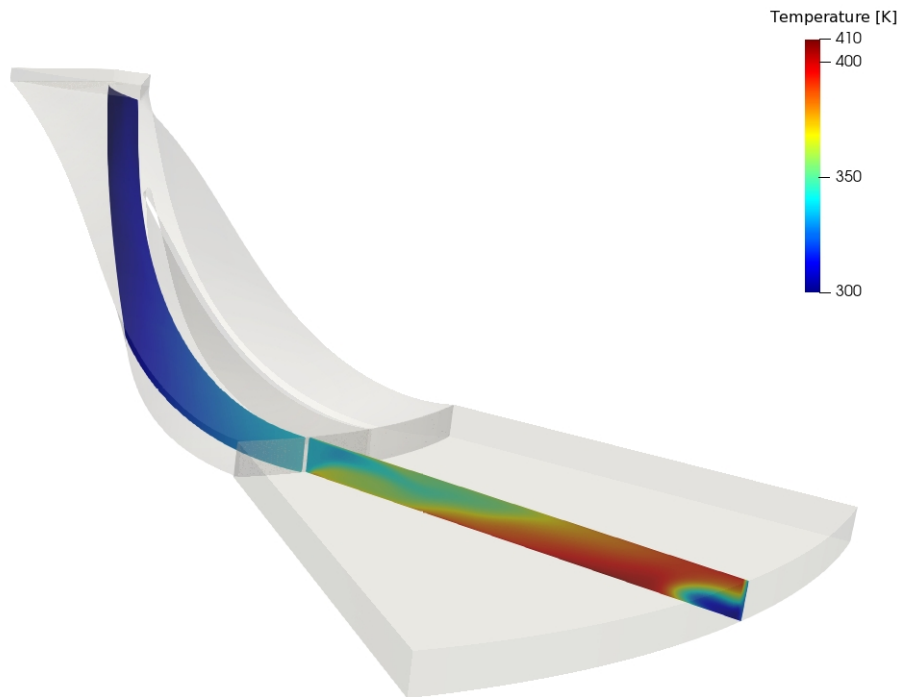


Figure 5.2.20: Temperature field view at meridional plane.

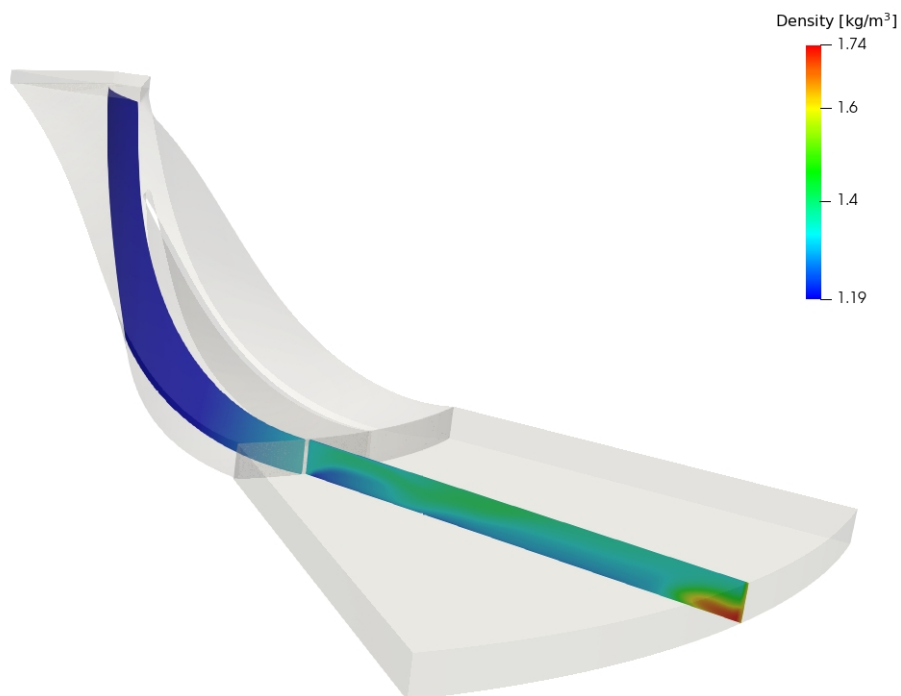


Figure 5.2.21: Density distribution at meridional plane.

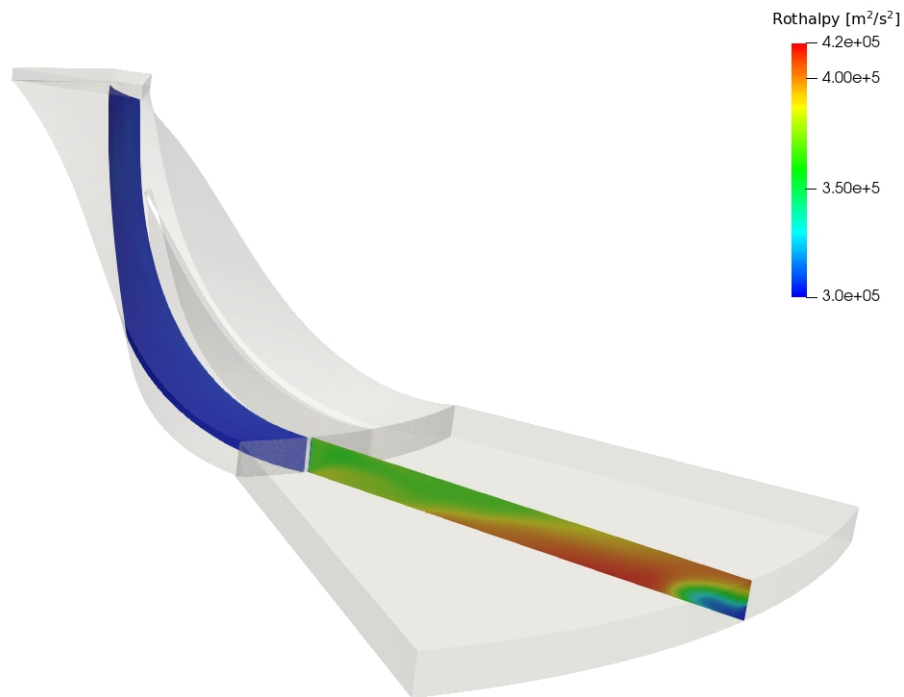


Figure 5.2.22: Rothalpy field at meridional plane.

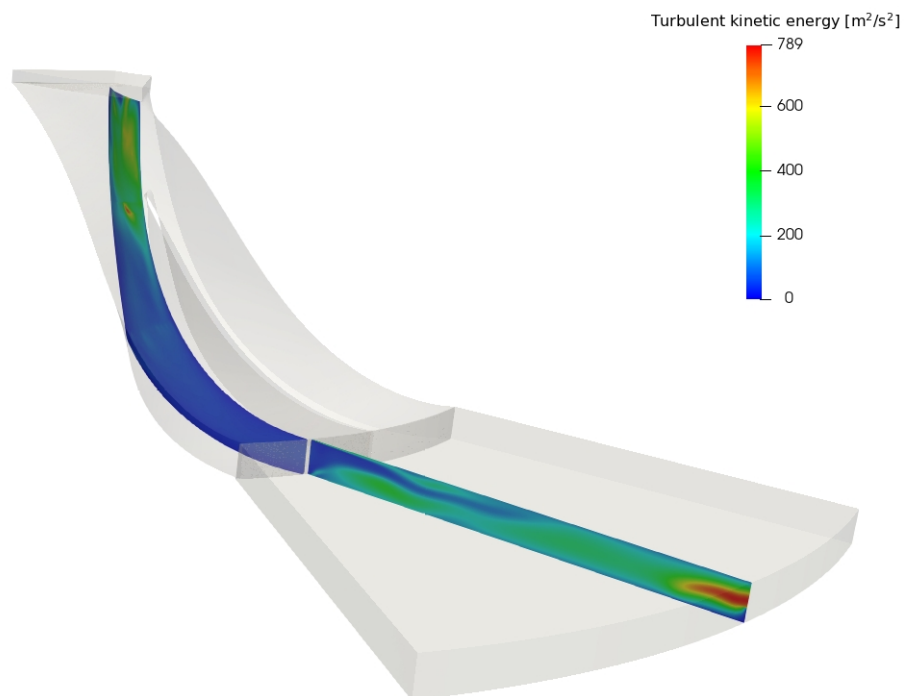


Figure 5.2.23: Turbulent kinetic energy field at meridional plane.

Fig. 5.2.24 represents the pressure field, Fig. 5.2.25 represents the velocity field and Fig. 5.2.26 represents the temperature field on the whole geometry. This kind of results are made by copying single passage results nine times.

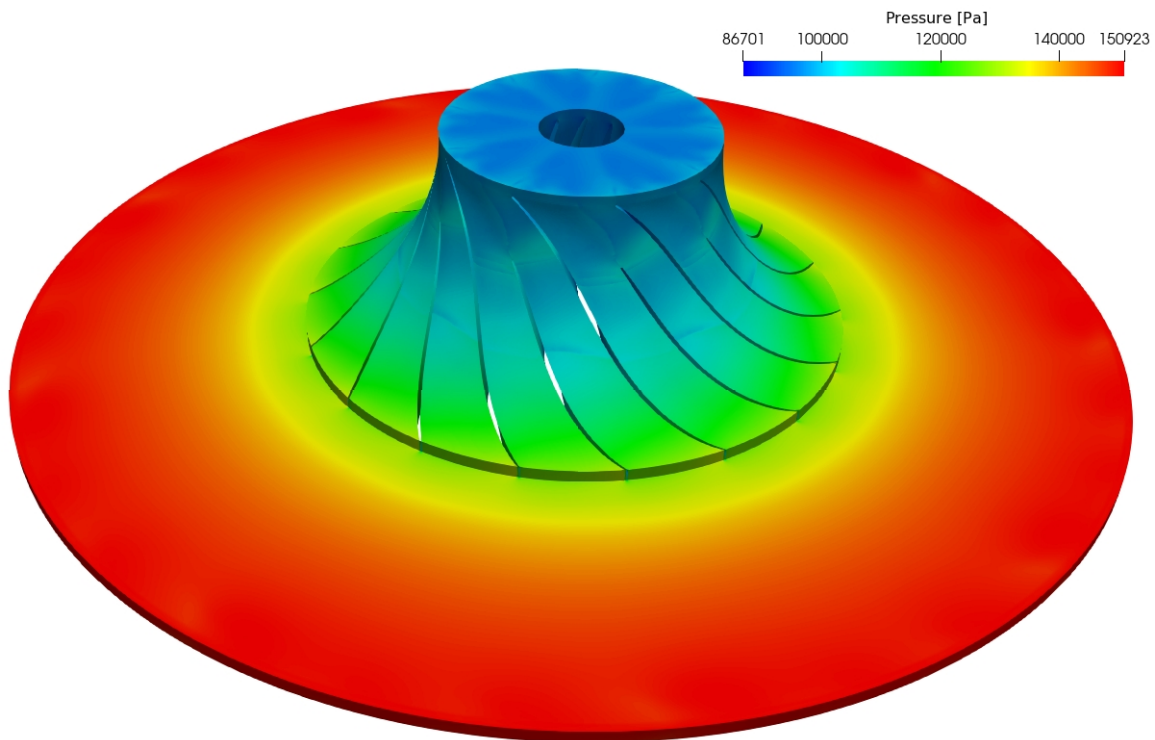


Figure 5.2.24: Pressure field at whole geometry.

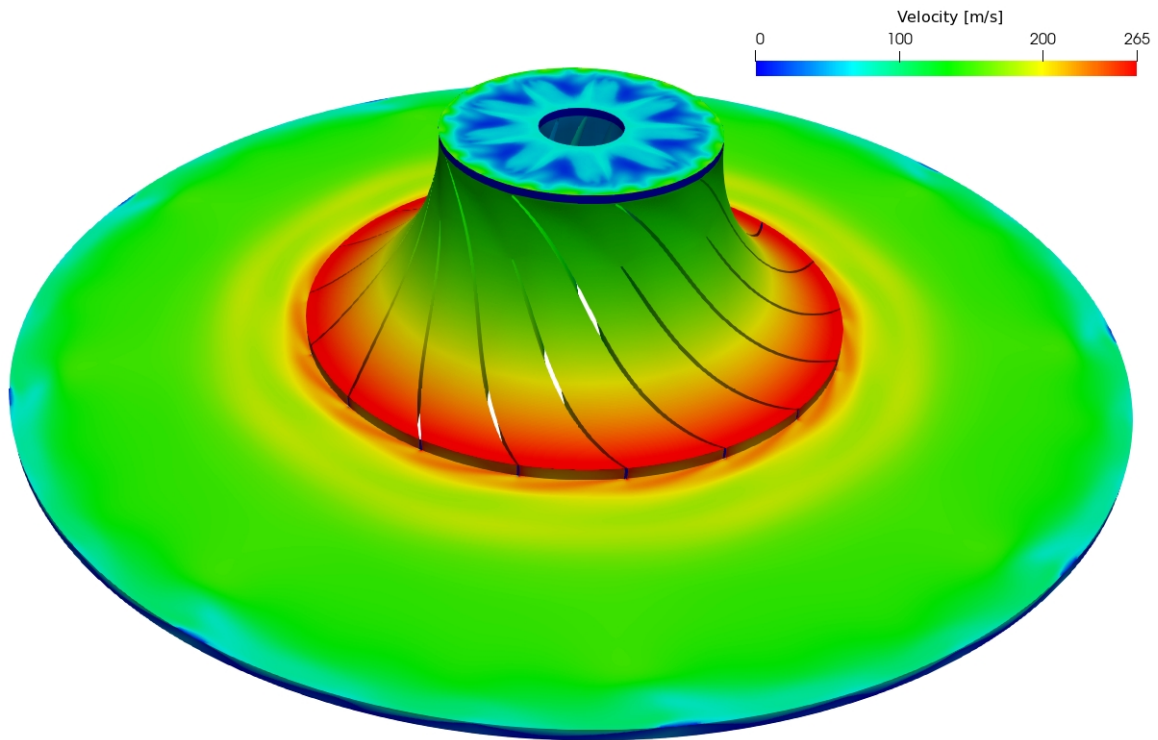


Figure 5.2.25: Velocity field at whole geometry.

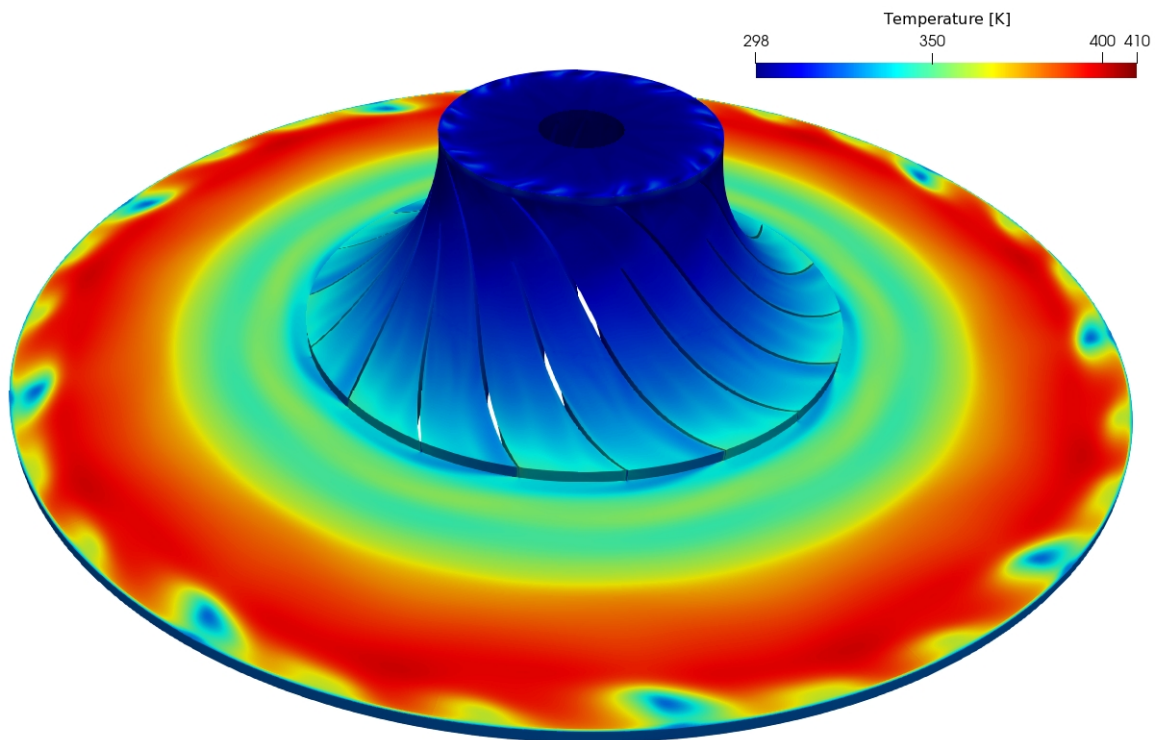


Figure 5.2.26: Temperature field at whole geometry.

5.3 Off-design operating condition

The results of the off-design points simulations will be presented in this section, eg. choke conditions.

5.3.1 Choke condition

For choke condition, the pressure field is shown in Fig. 5.3.2 and density field in Fig. 5.3.3. Other fields are similar to ones shown before and there is no clear shock wave occurring in this condition. To achieve the choke condition, the mass flow rate was increased outside operating range, Fig. 5.2.1.



Figure 5.3.1: Shock wave location.

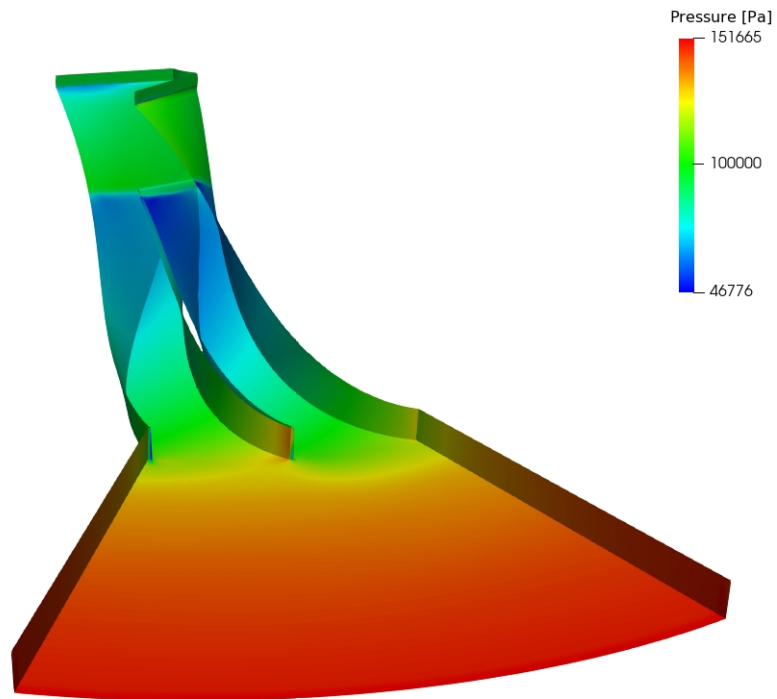


Figure 5.3.2: Pressure field for choke condition.

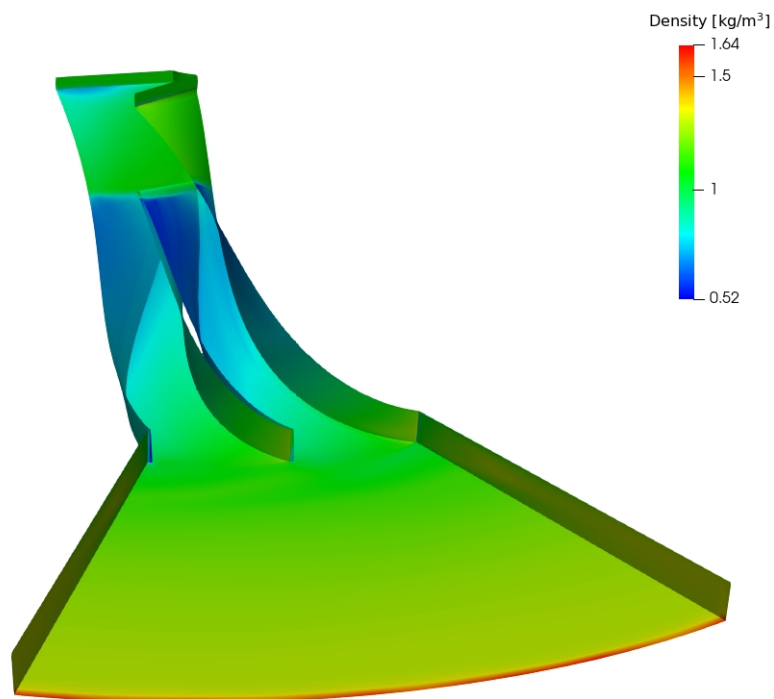


Figure 5.3.3: Density field for choke condition.

As mentioned before, the shock wave can be seen in Fig. 5.3.2 and Fig. 5.3.3, recognised as the sudden change in pressure or density. The consequence of the shock wave inside rotor is that it disables the propagation of information from outlet to inlet. In this case, the change of pressure at the outlet would not be able to "reach" beyond shock wave in order to get out of off-design condition. The only possible way to get away from this state is to decrease the mass flow at the inlet.

5.4 Closure

In this chapter, the results for three nominal compressor operating points will be presented, as well as the results for choke conditions. In the following chapter, the final remarks and conclusion will be given.

Chapter 6

Conclusion

6.1 Conclusion

In the Thesis the possibilities of CFD for simulation of design and off-design conditions in a centrifugal compressor was investigated. An introduction was given with an overview of the types of turbomachinery, including the differences between radial and axial compressors. Equations for flow inside compressors were described in the introduction as well. The Finite Volume Method, discretisation of governing equations, eg. compressible Navier-Stokes equations, was given in the second chapter. In addition, turbulence models were also described. The third chapter gave an overview of the applications of CFD methods in turbomachinery, covering domain and interface handling. In the domain handling section, the frozen rotor and moving mesh methods were described. The interface handling section gave an overview of the GGI and mixing plane interfaces. In the fourth chapter the geometry of centrifugal compressor from which the computational domain was created was shown with the addition of equations used in describing the flow in centrifugal compressors. Details and challenges of the making of mesh and geometry preprocessing were shown as well. At the end of the chapter, simulation setup was outlined. The results were given for three operating points and one off-design point in the last chapter. Results were outlined in form of the mass flow rate, rotor force, rotor moment and power. Mass flow rate results were compared with experimental results. In the end, results for the off-design point was given. The most noticeable flow features observed in the simulations were: velocity vectors directions inside the compressor, lambda shock and choke

operating condition.

6.2 Future Work

Future work as a continuation of the Thesis, would include running simulations for the stall operating conditions. Beside off-design conditions, simulations for more nominal operating points with different conditions would be good extension to this Thesis, and to complete the full compressor operating map. Transient simulations could also provide insight into more details of the features in off-design conditions.

Appendix A

Appendix

A.1 MRFZone

Example of the code used to define the Multiple Reference Frame which has assigned rotation.

The file MRFZones is located in case_dir/constant.

```
rotorCells
{
    //patches (rotor);
    // Fixed patches (by default they 'move' with the MRF zone)
    nonRotatingPatches
    (
        inlet
        outlet
        inletShroud
        inletHub
        statorHub
        statorShroud
        ggiInlet
        ggiInletRotor
        ggiOutletRotor
        ggiInletStator
    );
    origin    origin [0 1 0 0 0 0 0] (0 0 0);
    axis      axis   [0 0 0 0 0 0 0] (0 0 1);
    omega     omega  [0 0 -1 0 0 0 0] 2896.548427; // 27660 rpm
}
```

```
rampTime 1400;
}
```

- nonRotatingPatches - Patches which are stationary in regard to the rotational part.
- origin - Origin of the axis.
- axis - Axis of revolution.
- omega - Angular velocity in rad/sec.
- rampTime - Time instance in which the full angular velocity is reached.

A.2 GGI

Dictionary used to define GGI patch.

The file is located in `case_dir/constant/polyMesh/boundary`.

```
ggiInletRotor
{
    type            ggi;
    nFaces          14157;
    startFace       21392095;
    shadowPatch     ggiInlet;
    zone            ggiInletRotorZone;
    bridgeOverlap   false;
}
```

- type - Defines the type of ggi.
- nFaces - Defined by the mesh, user should not change this.
- startFace - Defined by the mesh, user should not change this.
- shadowPatch - Pair of the GGI patch.
- zone - Name of the faceZone of the patch being defined.
- bridgeOverlap - If it is false, uncovered faces are disallowed. If it is true in the non-overlapping cases, slip boundary condition will be defined.

A.3 cyclicGgi

Example of the code which is used to define the cyclicGgi patch.

The file is located in `case_dir/constant/polyMesh/boundary`.

```
cyclicRotor1
{
    type            cyclicGgi ;
    nFaces          99;
    startFace       21391897;
    shadowPatch     cyclicRotor2 ;
    zone            cyclicRotor1Zone ;
    bridgeOverlap   false ;
    rotationAxis    (0 0 1);
    rotationAngle   -40;
    separationOffset (0 0 0);
}
```

- `type` - Defines type of ggi.
- `nFaces` - Defined by the mesh, user should not change this.
- `startFace` - Defined by the mesh, user should not change this.
- `shadowPatch` - Pair of GGI patch.
- `zone` - Name of the faceZone of the patch being defined.
- `bridgeOverlap` - If it is `false`, uncovered faces are disallowed. If it is `true` in the non-overlapping cases, slip boundary condition will be defined.
- `rotationAxis` - Axis of revolution.
- `rotationAngle` - Rotation angle needed with respect to `rotationAxis` to match `shadowPatch` pair.
- `separationOffset` - Used for patches with transitions.

A.4 OpenFoam Boundary Conditions Description

A detailed overview of boundary conditions shown in Tables 4.3.9, 4.3.10 and 4.3.11 are given here.

A.4.1 von Neumann Boundary Condition

zeroGradient

```
inlet
{
    type            zeroGradient;
}
```

gradientEntalphy

```
inletHub
{
    type            gradientEntalphy;
    gradient        uniform 0;
    value           uniform 302100;
}
```

A.4.2 Dirichlet Boundary Condition

fixedValue

```
inlet
{
    type            fixedValue;
    value           uniform 96000;
}
```

A.4.3 Mixed Boundary Conditions

inletOutlet

```
    outlet
    {
        type            inletOutlet;
        inletValue      uniform 7400;
        value            uniform 7400;
    }
```

pressureInletOutletVelocity

```
    outlet
    {
        type            pressureInletOutletVelocity;
        value            uniform (0 0 0);
    }
```

A.4.4 GGI Boundary Conditions

ggi

```
ggiInlet
{
    type            ggi;
    value            uniform (0 0 0);
}
```

cyclicGgi

```
cyclicInlet1
{
    type            cyclicGgi;
    value            uniform (0 0 0);
}
```

ggiEntalphyJump

```
ggiInlet
{
    type          ggiEntalphyJump ;
    patchType     ggi ;
    rotating      false ;
    value         uniform 302100;
}
```

A.4.5 Wall Boundary Conditions

alphatWallFunction

```
inletHub
{
    type          alphatWallFunction ;
    Prt          0.85;
    value         uniform 0;
}
```

kqRWallFunction

```
inletHub
{
    type          compressible :: kqRWallFunction ;
    value         uniform 0.375;
}
```

mutWallFunction

```
inletHub
{
    type          mutkWallFunction;
    Cmu           0.09;
    kappa        0.41;
    E             9.8;
    value        uniform 1e-5;
}
```

omegaWallFunction

```
inletHub
{
    type          compressible :: omegaWallFunction;
    refValue     uniform 0;
    Cmu          0.09;
    kappa        0.41;
    E            9.8;
    beta1        0.075;
    value        uniform 7400;
}
```


Bibliography

- [1] R. K. Turton, *Principles of turbomachinery*. Springer Science & Business Media, 1995.
- [2] L. Balatinec, “An overview of rotor-stator interfaces for computational fluid dynamics simulations in turbomachinery,” Master’s thesis, Master’s thesis, University of Zagreb, 2019.
- [3] H. Jasak, “Course materials for Numerical Methods in Continuum Mechanics Method,” 2019.
- [4] G. Cvijetić, *Steady state methods for turbomachinery*. Faculty of Mechanical Engineering and Naval Architecture, University of Zagreb, Aug. 2014.
- [5] E. Dick, *Fundamentals of turbomachines*, vol. 109. Springer, 2015.
- [6] S. L. Dixon and C. Hall, *Fluid mechanics and thermodynamics of turbomachinery*. Butterworth-Heinemann, 2013.
- [7] E. Sundström, *Centrifugal compressor flow instabilities at low mass flow rate*. PhD thesis, KTH Royal Institute of Technology, 2016.
- [8] B. Dewar, J. Tiainen, A. Jaatinen-Värri, M. Creamer, M. Dotcheva, J. Radulovic, and J. M. Buick, “CFD modelling of a centrifugal compressor with experimental validation through radial diffuser static pressure measurement,” *International Journal of Rotating Machinery*, vol. 2019, 2019.
- [9] A. T. Sayers, *Hydraulic and compressible flow turbomachines*. No. BOOK, McGraw-Hill, 1990.

- [10] M. R. Galvas, *Fortran program for predicting off-design performance of centrifugal compressors*, vol. 7487. National Aeronautics and Space Administration Washington, DC, USA, 1973.
- [11] J. R. Serrano, A. Tiseira, L. M. García-Cuevas, L. B. Inhestern, and H. Tartoussi, “Radial turbine performance measurement under extreme off-design conditions,” *Energy*, vol. 125, pp. 72–84, 2017.
- [12] J. Zhao, Z. Wang, Y. Zhao, and G. Xi, “Investigation of transient flow characteristics inside a centrifugal compressor for design and off-design conditions,” *Proceedings of the Institution of Mechanical Engineers, Part A: Journal of Power and Energy*, vol. 232, no. 4, pp. 364–385, 2018.
- [13] H. Wan, S. S. Patnaik, and A. Heltzel, “Study of centrifugal compressor off-design performance based on cfd simulations,” in *2018 AIAA Aerospace Sciences Meeting*, p. 0246, 2018.
- [14] H. Jasak, *Error analysis and estimation for the finite volume method with applications to fluid flows*. PhD thesis, 1996.
- [15] T. Uroić, *Implicitly coupled finite volume algorithms*. PhD thesis, University of Zagreb. Faculty of Mechanical Engineering and Naval Architecture., 2019.
- [16] D. C. Wilcox *et al.*, *Turbulence modeling for CFD*, vol. 2. DCW industries La Canada, CA, 1998.
- [17] F. Menter, “Zonal two equation kw turbulence models for aerodynamic flows,” in *23rd fluid dynamics, plasmadynamics, and lasers conference*, p. 2906, 1993.
- [18] F. Menter, “Two-equation eddy-viscosity turbulence models for engineering applications,” *AIAA journal*, vol. 32, no. 8, pp. 1598–1605, 1994.
- [19] F. Menter and T. Esch, “Elements of industrial heat transfer predictions,” in *16th Brazilian Congress of Mechanical Engineering (COBEM)*, vol. 109, p. 650, 2001.
- [20] F. Menter, M. Kuntz, and R. Langtry, “Ten years of industrial experience with the SST turbulence model,” *Turbulence, heat and mass transfer*, vol. 4, no. 1, pp. 625–632, 2003.

-
- [21] A. Hellsten, "Some improvements in Menter's k-omega SST turbulence model," in *29th AIAA, Fluid Dynamics Conference*, p. 2554, 1998.
- [22] "The MRF Development."
http://openfoamwiki.net/index.php/See_the_MRF_development. Accessed: 03-17-2021.
- [23] H. Jasak, "Dynamic mesh handling in openfoam," in *47th AIAA aerospace sciences meeting including the new horizons forum and aerospace exposition*, p. 341, 2009.
- [24] M. Beaudoin and H. Jasak, "Development of a generalized grid interface for turbomachinery simulations with OpenFOAM," in *Open source CFD International conference*, vol. 2, Berlin, 2008.
- [25] "Pointwise."
<http://www.pointwise.com/about/index.html>. Accessed: 03-22-2021.